# Thermoluminescent Microparticles used as Harsh Environment Temperature Sensors Characterized using MEMS Devices

**A THESIS**
**SUBMITTED TO THE FACULTY OF THE GRADUATE SCHOOL**
**OF THE UNIVERSITY OF MINNESOTA**
**BY**

**Philip Robert Armstrong**

**IN PARTIAL FULFILLMENT OF THE REQUIREMENTS**
**FOR THE DEGREE OF**
**Ph.D. in Electrical Engineering**

**Joseph J. Talghader**

**July, 2017**

# Acknowledgements

To my advisor Dr. Joseph J. Talghader for keeping me on track and giving me good ideas and advice.

To my colleague Merlin Mah, who I worked with on the same project, helped me refine many of my own ideas and built many of the measurement systems I used that allowed for more complex and prolific measurements.

To everyone in my research group who even though they were busy with their own projects took the time to help me find solutions to problems in my own project.

To all of the staff in the Minnesota Nano Center that gave me advice on my fabrication processes and maintained the equipment I so frequently found a way to break.

To the Defense Threat Reduction Agency(DTRA) that funded the research presented in this thesis.

# Dedication

To my Mother and Parvis for always believing in me.

## Abstract

The measurement of glow curves from thermoluminescent materials has had important applications in geological/archeological dating and radiation dosimetry. A method for using thermoluminescent materials in a temperature sensing application will be described in this thesis. Thermoluminescence is a process by which an ionizing radiation source excites carriers that eventually settle into trap states. Thermal energy due to a temperature profile is then used to empty the carriers from these trap states allowing them to radiatively recombine. Measuring the thermoluminescent intensity versus temperature is called a glow curve and contains information about the traps in wide bandgap ($> 5.5$eV) insulating materials. One such material, yttrium oxide with a terbium impurity, was deposited as a thin film on a silicon substrate in order to characterize the use of lanthanides in a insulating host material for thermoluminescent applications. Lanthanides can act as both a trap and recombination center. Eventually microparticles of lanthanide doped magnesium borate and calcium sulfate where determined to be the best samples for testing. When the microparticles of magnesium borate or calcium sulfate are exposed to a temperature profile like those that occur during explosives testing the filled trap density will decrease different amounts depending on the physical properties of a given trap. The temperature profile can be calculated by comparing the altered glow curve of a sample that experienced the explosive event to the glow curve of a sample that was not in the explosive event, this technique has been shown to be effective in measuring temperatures up to just above 500°C. The limitation in maximum temperature is in large part due to the maximum temperature possible during a glow curve measurement before thermal emission from the heat source overwhelms the thermoluminescence of the sample. To combat this parasitic thermal emission, and extend the usable temperature range of this sensing technique, two methods are demonstrated to reduce thermal emission. The first method uses a microheater with the metal heating element placed around the perimeter and an aperture placed over the center where a thermoluminescent microparticle is placed blocking thermal emission from the heating element but allowing the light from the microparticle to escape. The second method

deposits a distributed Bragg reflector on the top and bottom of a microheater which reduces its emissivity at wavelengths that match the microparticle emission spectrum.

# Contents

# List of Tables

# List of Figures

# Chapter 1

# Introduction

## 1.1 A Brief Overview

Chapter 1 is a brief overview of this dissertation. Each section in this chapter is a summary of what will be described in the following chapters. Therefore a lot of details will be left out but the basic concepts will be discussed.

## 1.2 Applications for Thermoluminescence

Materials which show thermoluminescence are first irradiated by an ionizing radiation source and then upon heating emit visible light. This is not to be confused with blackbody radiation which is a completely different mechanism for light emission. The intensity and emission spectra of the emitted light in thermoluminescence can depend on the properties of the material as well as the type of ionizing radiation to which it was exposed. Equation (1.1) is the first-order kinetics method for describing the intensity of thermoluminescence for a crystalline sample that is heated at a linear rate. The variables of $s$ and $E_t$, and $n$ stand for the frequency factor, trap depth, and filled trap density respectively. The rate of linear heating is the value $\beta$. The light intensity measurement of thermoluminescence is also known as a "glow curve".

$$I(T) = sn_0 exp(E_t/kT) exp\left[\frac{-s}{\beta}\int_{T_0}^{T} exp(-E_t/k\theta)d\theta\right] \tag{1.1}$$

More details on this process will be described in later chapters, for now a brief background on current applications of thermoluminescence will be described.

There are two very common applications for thermoluminescence. The first being geological and archaeological dating [1–5]. The materials used in dating are exposed to cosmic radiation or radioactive isotopes that exist naturally. Over time these small amounts of ionizing radiation will be absorbed by the thermoluminescent material. The intensity of the light emission from the material during heating can then be measured and the age of the material estimated. The intensity of the thermoluminescence will increase as more radiation is absorbed. The intensity of the signal will then allow for the estimation of the age of the material. This is a common practice in geological dating where it can supplement or replace radiometric dating. Archeological dating of materials or in this case objects such as pottery works in a similar fashion. Pottery is typically fired in a kiln as part of the process in making it. During this step any possible thermoluminescent materials that have already absorbed some ionizing radiation will empty during the heating from the kiln. Then after it has cooled it will begin to absorb radiation again. The age of ancient pottery can be estimated by measuring the intensity of the thermoluminescent signal.

The second common applicaton for thermoluminescence is thermoluminescent dosimetry(TLD) [6–9]. This is a method for measuring the amount of radiation that a person may have been exposed to in environments that use equipment which emit ionizing radiation such as x-ray diffraction machines or nuclear reactors. These are crystalline materials that are grown and designed to have unique responses to different kinds of ionizing radiation. Typically a person will wear a TLD ring or badge while being around possible sources of radiation. After a certain amount of time the TLD material will be measured to determine if there was any exposure to harmful radiation. As with the geological applications the intensity of the thermoluminescent signal will indicate how much radiation exposure there may have been. The most common of TLD materials used in these applications is TLD-100(LiF:Mg,Ti) [6], which is useful because it absorbs certain kinds of ionizing radiation such as x-rays at the same rate as human tissue. It is also not effected by photobleaching due to ambient visible light.

Another possible application for thermoluminescence will be described in this thesis. The previous applications for thermoluminescence were most concerned with measuring

the intensity of the signal to estimate the radiation exposure. But these methods do not consider the information that can be determined when looking more closely at the light emitted from the thermoluminescent material during heating. The intensity of the emitted light can fluctuate during heating, which is caused by defects and impurities in the crystalline material. If a thermoluminescent sample material is irradiated with a known dosage and then exposed to a temperature profile which only partially nullifies the thermoluminescence of the material it is possible to determine that temperature profile by comparing it to a sample that was exposed to the same dosage of radiation but did not experience that temperature profile. By looking at the difference between the thermoluminescent responses of the two samples the temperature profile can be determined. In this way thermoluminescent materials can act as a temperature sensors.

## 1.3 Rare Earth Doped Thin Film TL Materials

Rare earths have interesting properties like efficient photon up-conversion and a narrow wavelength emission of light. Thermoluminescence has been used to probe the physical parameters of rare earth traps in wide band gap ($> 5.5$eV) materials. Because rare earths are not as strongly affected by their host material their behavior is more predictable. When used in thermoluminescence as a recombination center they have characteristic wavelength emissions that remain relatively unchanged between similar host materials. For example the emission spectra for $Y_2O_3$:$Tb^{3+}$ and $ZrO_2$:$Tb^{3+}$ are almost identical. This is because the trivalent state leaves the $5p^6$ and $5s^2$ shells filled. This shields the 4f shell of the rare earth from being effect by the host material. And due to the unique 4f-4f transitions that are allowed in rare earths they can maintain their distinct wavelength emissions.

Finding methods to fabricate TL thin films that are compatible with standard VLSI techniques would be useful for mass production. A simple and cheap method for growing TL thin films of $Y_2O_3$:$Tb^{3+}$ using electron beam evaporation is possible. It starts with mixing the host material $Y_2O_3$ powder form with the powder form of $Tb_4O_7$. Then placing the mixture in a graphite crucible and using electron beam evaporation to grow the film on standard p-doped silicon (100) 4 inch wafer. The wafer is then annealed to promote crystal formation. In the case of $Y_2O_3$:$Tb^{3+}$ thin films one of the most

important features of the host material is that it helps to be crystalline or at least poly crystalline. There is a direct correlation between the crystallinity of a material and the intensity of the measured glow curve [10]. For the example of $Y_2O_3$:$Tb^{3+}$ the strength of the crystal peaks measured are showed to have a correlation to the intensity and shape of the measured glow curves. The emission spectra of the $Y_2O_3$:$Tb^{3+}$ was measured and showed two strong peaks at 490nm and 540nm. These indicate the characteristic 4f-4f transitions of the $Tb^{3+}$ ion. The 490nm and 540nm peaks correspond to the $^5D_4$ to $^7F_5$ and $^7F_6$ transitions respectively. An example of the glow curve for $Y_2O_3$:$Tb^{3+}$ is shown in figure 1.1. The shape of the curve suggests that it is the result of the depopulation of several traps in the band gap of $Y_2O_3$.

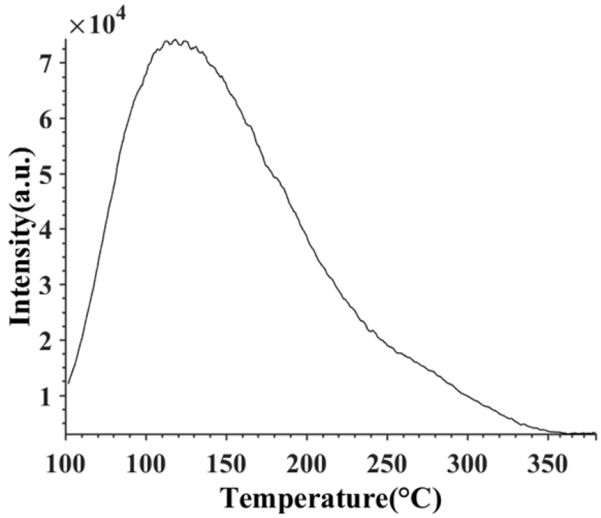


Figure 1.1: Glow curve for UV irradiated $Y_2O_3$:$Tb^{3+}$

## 1.4 Thermoluminescent Materials used as Temperature Sensors

The maximum value of the first-order kinetics equation when plotted with respect to time is dependent on the filled trap density $n$. The filled trap density is decreased when a thermoluminescent sample is exposed to a temperature profile with a maximum temperature that is high enough to empty some of the filled traps in the band gap. If

only some of these traps empty the leftover filled traps can be thought of as containing information about the temperature profile. If the shape of the profile is known such as the rapid thermal increase and exponential decrease in temperature of an explosive event it could be possible to determine the maximum temperature and decay constant of the exponential cooling. This rapid thermal increase and subsequent cooling can be modeled by Equation (1.2). For the case of a single trap TL material this method

$$T(t) = T_{max} exp(-t/\tau) \tag{1.2}$$

will only work if the initial value $n_0$ of the filled traps is known. In practice this would mean that the exact same sample would have to be used and irradiated with the exact same amount of ionizing radiation. This is impractical so the alternative is to use a thermoluminescent material that has several traps that contribute peaks to the glow curve. And most importantly it should have a high temperature peak that has negligible depopulation during the explosive event. This is important because the intensity of the lower temperature peaks can be compared to the higher temperature peaks and the ratio of the peaks can be calculated. Then the ratio of the peaks can be compared to a control sample that was irradiated along with the sample that went through explosive testing. By comparing the ratios from the control sample to the sample in the explosive testing the values of $\mathrm{T_{max}}$ and $\tau$ can be calculated. This calculation is carried out by reconstructing the glow curve of the control sample by finding the values of $s$ and $E_t$ and using a composite of first order peaks to fit the shape of the glow curve. Then taking a range of values for $\mathrm{T_{max}}$ and $\tau$ and substituting them into equation (1.2). A simulation of the glow curve after being exposed to a rapid thermal increase as described in equation (1.2) is compared to samples that were in the explosion. Comparison between the simulated and measured results will allow for the reconstruction of the temperature profile.

## 1.5 Reduced Thermal Emission Microheaters

One fundamental problem with taking the glow curve of a thermoluminescent material is that at high temperature the device being used to heat the sample will give off

some amount of blackbody radiation or more generally speaking some kind of thermal emission. An example of how thermal emission alters a glow curve measurement is shown in Figure 1.2. This limits

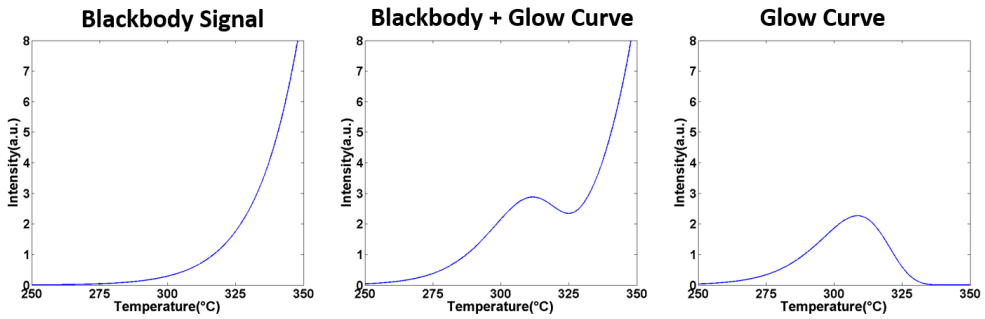


Figure 1.2: How the blackbody signal will change the shape and intensity of a Glow curve.

the amount of information that can be retrieved by using thermoluminescence to probe the trap configuration of a material. Because of this a standard method for blocking out parasitic thermal emissions is to use an optical filter. At standard glow curve measurement temperatures the thermal emission wavelengths are relatively weak below about 500nm. An optical filter is used to block out all the thermal radiation at wavelengths higher than 500nm. While this works well for materials that emit at wavelengths below 500nm it will block any signal being emitted by the thermoluminescent material above 500nm along with the thermal emission. It would be useful if there was a way to reduce the thermal emission at all wavelengths or tailor a device that has a reduced emissivity at wavelengths of interest. There is two possible solutions to this problem. The first is a heating element around the periphery of a device with a aperture over the center. The heating element made out of metal will be highly emissive at temperatures of interest for glow curve measurements but the structural material supporting it and the sample can be a less emissive ceramic. By placing an aperture over the center of the microheater most of the thermal emission from the heating element can be blocked while still letting the thermoluminescent emission from the sample that is in the center get through. The second solution is to alter the emissivity as a function of wavelength for the device that is heating the sample. This is achievable by using the multilayer structure around the heating element which is designed to have a certain absorption

coefficient at wavelengths of interest. According to Kirchoff's Law of Radiation the absorptivity of a body is equal to its emissivity. So thermal emission wavelengths can be tailored to not overlap with the emission spectrum of the thermoluminescent material to allow for higher temperature measurements.

# Chapter 2

# Theory of Thermoluminescence

## 2.1 Introduction to First-Order Kinetics of Thermoluminescence

Thermoluminescence is a luminescent process similar to photoluminescence and electroluminescence. In each of these types of luminescence, some form of energy is introduced to a material to generate an excited state. When this excited state decays to a ground state it will emit a photon. A material can be considered luminescent when it emits a photon in response to an absorption of energy. There are many kinds of luminescence with the main difference between them being how the excited state is initialized. In the case of photoluminescence, a photon is responsible for the excitation; for electroluminescence it is a electrical current or potential. When the excited state is generated it can take varying amounts of time for it to decay to a ground state. The process is called fluorescence when the excited stated is allowed to go directly to the ground state. The lifetime of the excited state in this case is usually in the nanoseconds to milliseconds range. It can take longer with the presence of a metastable state. Instead of going directly from an excited state to a ground state the process can be delayed by the presence of a metastable state. This third state for the system is a temporary state before the system goes back to the ground state. Phosphorescence occurs when a metastable state "slows" the decay of an excited state. In this case the excited state can take seconds or much longer to reach the ground state. With thermoluminescence

the time between excitation to photon emission can take years. This is because thermoluminescence consists of two excitations. The first is some form of ionizing radiation or ion bombardment which induces the excited state. The carrier in the excited state can then get trapped in a metastable state. The carrier can remain in the metastable state for much longer periods of time until enough thermal energy is used to stimulate the carrier in the metastable state so that it reaches the excited state again and falls to the ground state which releases a photon. This is assuming that the excited state does not go back to the metastable state. So the term thermoluminescence is deceiving because it implies that that excited state is initialized by thermal energy. But it is actually a two step process using two different forms of energy to complete the process instead of just a photon or electrical field. A more accurate term for thermoluminescence would be thermally stimulated luminescence. This is because the final step is always stimulated by thermal energy. But thermoluminescence has become the accepted term for this process.

Thermoluminescence has been shown to occur in crystalline, polycrystalline, and amorphous materials [11–28]. It can even occur in biological material such as spinach or bones [29–32].The majority of the studies have been focused on inorganic insulating materials which show some kind of crystalline or polycrystalline structure. This is because the physical models used to explain thermoluminescence assume a crystalline structure. When "crystalline" is used it may bring to mind the 14 possible Bravais lattices. In all 14 of these lattices each point is arranged in a 3D space in specific positions and is all arranged according to the lattice for an infinite distance. These lattices can be related to natural or artificially occurring materials by replacing each of the lattice points with an atom or atoms. In practice the crystal will be finite in side, have impurities or defects, and have dangling bonds at the surface. The impurities and defects in the imperfect crystal are what make thermoluminescence possible.

The band gap model for insulating materials states that there is a forbidden region of energy between the conduction and valence bands where electrons and holes cannot exist in a perfect crystal. But imperfections in the crystalline material can alter the regular potential energy structure; this can lead to allowed states for electrons and holes in the bad gap of the material, also known as traps. Depending on their relative position from the conduction or valence band, the trapped electron or holes will require more or

less energy in order to leave the trap. Now take for instance a photon or ion incident on a crystalline material with enough energy to raise an electrons into the conduction band and holes into the valence band where they are free to fall into a corresponding electron or hole trap. If an electron trap is close enough to the conduction band there may be enough thermal energy due to the temperature of a material to generate phonons that can transfer enough energy to the trapped electron to raise it into the conduction band. While in the conduction band the electron is in a more unstable state and able to recombine with a hole trap. The hole trap would have be deep enough so that it could not be emptied by the same amount of thermal energy. The more thermally stable hole trap acts as a luminescent or recombination center for the electron, which is the cause of the photon emission. The situation can be reversed for a hole trap close to the valence band and an electron trap far from the conduction band. But these are the most simplified explanations for the process. It is possible that there are multiple electron traps and recombination centers [33–35]. When there are multiple recombination centers and a single electron trap the electron may recombine at anyone of these centers. The photon emitted from this recombination will have an energy that will depend on which center it had recombined. The case of multiple traps will be covered in more detail later in the chapter.

For the remainder of this section and following sections the explanation of thermoluminescence will follow that of Chen and Mckeever [36]. The measurement of thermoluminescence is typically carried out by heating a sample at a linear rate and measuring the intensity of light being emitted. The first-order Randal-Wilkins model is used for the simplest case of a trapped electron being released and recombining at a hole trap/recombination center. Figure 2.1 uses the band gap model to illustrate the process. The band gap has a trap density $n$ and a recombination center density of m. The depth of the trap $n$ is $E_t$ and size of the band gap is $E_g$. A photon with energy $E > E_g$ is able to transfer enough energy to raise a electrons from the valence band to the conduction band. While an electron is in the conduction band it is free to move around and possibly fall into the trap $n$. Assuming this happens multiple times the number of filled traps after the initial excitation is assumed to be $n$ now. The Boltzmann's distribution function can be used to give the probability that the state of a system will change given the energy in the system. From the Boltzmann's distribution function the

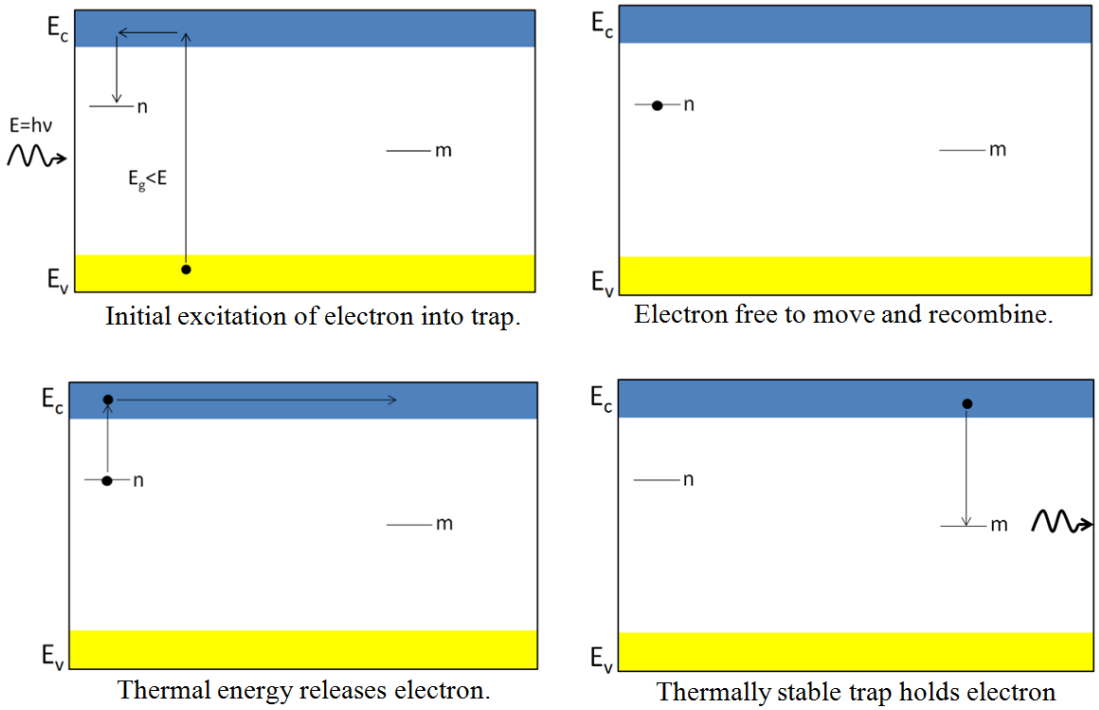


Figure 2.1: A simple illustration of thermoluminescence for a material with a band gap of $E_g$. A photon with energy E great enough raises an electron to from the valence band to the conduction band. While in the conduction band it is free to move around and possibly fall into the trap $n$. With enough thermal energy the electron can leave the trap and enter the conduction band. When in the conduction band it is free to move and recombine at the luminescent center.

probability that an electron will be able to leave the trap and enter the conduction band is shown in Equation (2.1).

$$p = \exp(-E_t/kT) \tag{2.1}$$

Here $E_t$ is the trap depth, k is Boltzmann's constant and T is the temperature. The probability that a trap will empty if kT $<<$ $E_t$ is extremely low. If the probability of a trap emptying is sufficiently low it is considered to be thermally stable. In regards to thermoluminescent (TL) materials this normally refers to the state of the trap at room temperature. This thermally stable state is what allows for the long period of time (years) between initial excitation and emission of a photon. According to the first-order

Randal-Wilkins model the number of photons given off per unit volume per unit time from the TL material is equal to the rate at which electrons empty from the $n$ traps. Equation (2.2) represents the connection between emitted photons and

$$I(T) = \frac{dn}{dt} = sn \exp(-E_t/kT) \tag{2.2}$$

the rate of trap emptying. The new constant $s$ in Equation (2.2) is commonly referred to as the frequency factor or pre-exponential factor. A better way to name it to help explain what it means is the "attempt-to-escape frequency. It can in essence be considered as an electron in a potential well where $s$ depends on the interactions with the lattice per unit time, the probability it will transition out of its current state and the entropy associated with the transition out of the state[24]. From here on, the frequency factor will be considered as a physical constant of the trap such as $E_t$. The Randal-Wilkins model assumes that each electron that leaves a trap is free to move around in the conduction band and then recombine at a luminescent center m, and that the probability an electron will fall back into the trap it was just released from is negligible (when an electron falls back into the trap it was just released from it is known as retrapping). Since I(t) is the number of photons per unit volume per unit time it can be multiplied by the appropriate constants to get the intensity or total energy being emitted. In practice the most important thing to know is the thermoluminescent intensity of a material as a function of the applied temperature. To demonstrate this the first order homogeneous differential equation of Equation (2.2) must be solved for $n$. The solution is shown in Equation (2.3).

$$n(t) = n_0 \exp\left[ - s \int_{t_0}^{t} \exp(-E_t/kT) dt \right] \tag{2.3}$$

As mentioned before the thermoluminescence as a function of temperature is of interest. The temperature is increased at a linear rate while the thermoluminescence is measured. Equation (2.4) is the linear heating rate with $\beta$ being the constant heating rate in units of temperature per time. The first derivative of Equation 4 with respect to time is taken and is shown in Equation (2.5).

$$T = T_0 + \beta t \tag{2.4}$$

$$\frac{dT}{dt} = \beta \tag{2.5}$$

In order to get the temperature desired dependence Equation (2.5) is used to replace dt and Equation (2.4) is used to define the new limits of integration in Equation (2.3). The temperature dependent function for the filled trap density is then given by Equation (2.6).

$$n(T) = n_0 \exp\left[\frac{-s}{\beta}\int_{T_0}^{T} \exp(-E_t/k\theta)d\theta\right] \tag{2.6}$$

The variable for temperature T in Equation (2.3) is replaced with a dummy variable $\theta$ in order to avoid confusion with the new limits of integration. Equation (2.6) is substituted for $n$ in the right hand side of Equation (2.2) to yield the final equation for the First order Randall-Wilkins model for thermoluminescence Equation (2.7).

$$I(T) = sn_0 \exp(-E_t/kT) \exp\left[\frac{-s}{\beta}\int_{T_0}^{T} \exp(-E_t/k\theta)d\theta\right] \tag{2.7}$$

It should be noted again that this does not take into account retrapping and assumes that each electron that leaves a trap will recombine at a luminescent center m to generate a photon. The rate in Equation (2.2) does not consider that the electron will exist in the conduction band for a finite period of time. But even with these simplifications the first order equation adequately describes the general idea of what happens in the thermoluminescence process. Figure 2.2 is an example graph of Equation (2.7), which is commonly known as a "glow curve". This is the general shape of a glow curve for a TL material with a single trap. The rising edge is defined by exponential term $exp(-E_t/kT)$ on the left side of the Equation (2.7) which starts at a small value and quickly approaches unity as kT approaches $E_t$. The exponential term on the right that includes the integration of an exponential function causes the falling edge to approach

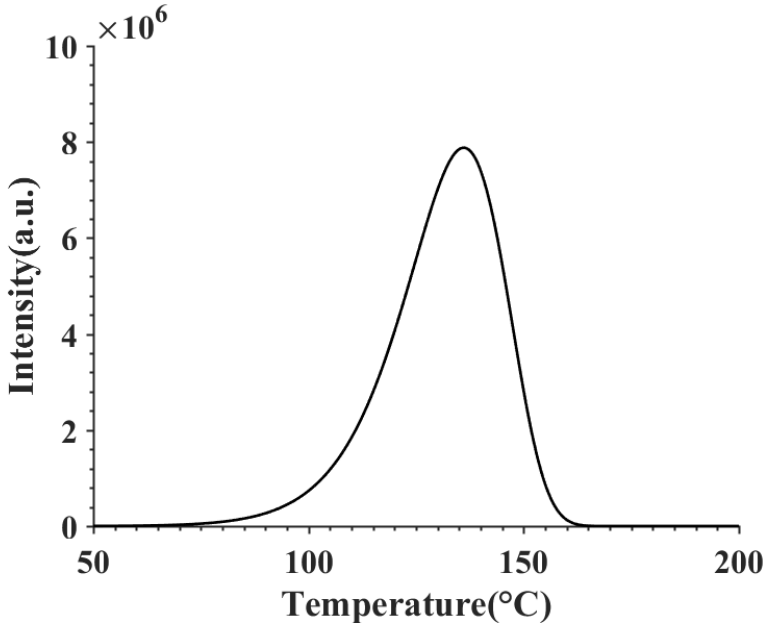


Figure 2.2: Example graph of Equation (2.7) which is thermoluminescence as a function of temperature according to the first-order Randall-Wilkins model. This is commonly referred to as a glow curve.

zero as the temperature rises. The shape of the rising edge is the same for all higher order models. So the first order model is will have a glow curve that is identical to that of higher order models up until the peak of the glow curve.

## 2.2 Effect of Physical Trap Parameters on Glow Curve

The physical parameters, $E_t$, $s$, and n, along with the heating rate $\beta$, will affect the width and peak position of the curves. Figure 2.3 is an example of how the peak position varies with three different values of $E_t$ which correspond to different electron trap depths but with the same $n$, $s$, and $\beta$. The values of $E_t$ are 1.1, 1.3, and 1.5 electron volts for $E_1$, $E_2$, and $E_3$ respectively. As the traps get deeper or farther away from the conduction band the glow curves begin to shift to higher temperatures. And this makes sense when going back to Equation (2.1). As the trap gets deeper it will require more thermal energy in order to start depopulating the trap. Typical values for trap depth range from 1-2eV. Below 1eV the traps start to become so shallow that

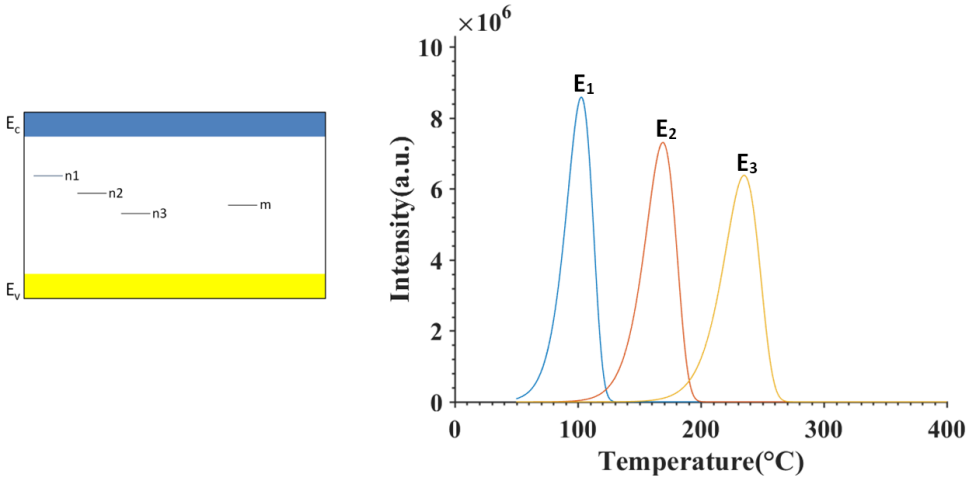


Figure 2.3: Example of how different trap depths effect the shape and position of a single order glow curve.

at room temperature they tend to start depopulating. When left at room temperature for hours to days most materials will not show any thermoluminescence below $100^oC$ on their glow curves. This can be attributed to thermal fading which will be discussed in more detail later. And traps with depths above 2eV are usually at such a high temperature that the thermal emission from the heating source used to measure them partially overwhelms the thermoluminescence from the sample. This can be overcome by various methods like optical filters or choosing a different heating rate. The trap depths are also limited by the size of the band gap. To a lesser extent, the change in trap depth also leads to a decrease in the intensity of the glow curve and an increase in the width. The amount of energy emitted in the form of photons in each of the cases is the same because the area under each curve is equal. When the trap depth is changed it is obvious that the glow curve peak will shift but what is less obvious is that it can change the rate at which the trap will empty. This is apparent when looking at the slopes of the glow curves at different trap depths.

The frequency factor $s$ will also shift the peak intensity of a glow curve and change its width. Figure 2.4 is an example of three possible values used for the frequency factor and how they can alter the glow curve. As before, all the other parameters are kept the same while only $s$ is changed. The values $s_1$, $s_2$,and $s_3$ are $10^{12}$ , $10^{14}$, and $10^{16}$

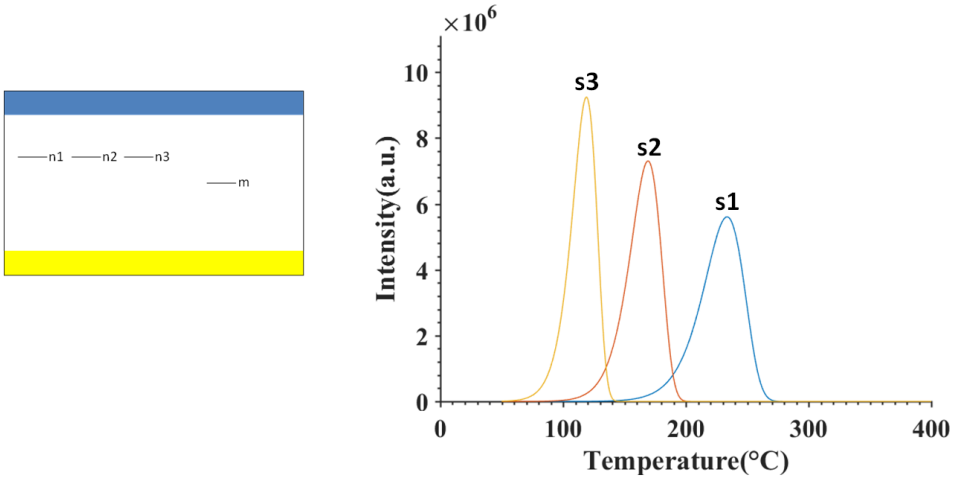


Figure 2.4: Example of how different frequency factors affect the shape and position of a single order glow curve.

inverse seconds respectively. With increasing values of the frequency factor, the glow curve peaks will begin to shift to lower temperatures and the widths will become more narrow. This can be explained by understanding what was mentioned before about the frequency factor. The carrier in the trap will be "attempting to escape" more frequently with a higher frequency factor. The higher the $s$ value is the more susceptible the trap is to empty at a given temperature. When the frequency factor increases the slope of the glow curve becomes steeper; hence this means for the same heating rate the traps empty more quickly. The frequency factor also changes the intensity and width of the glow curve similar to $E_t$. The main difference from $E_t$ is that the intensity will change more as the peak shifts to different temperatures. It has more influence as a scaling factor on the width and intensity than $E_t$. As before the area under the glow curve is unchanged so the total photon energy emitted is the same regardless of the frequency factor. Possible values of $s$ can range from $10^8$/s to $10^{18}$/s [37].

The filled trap density $n$ is a scaling factor for the intensity of the glow curves. Figure 2.5 gives three examples of how changing the trap density will affect the glow curve. The variation in trap density will only change the width and intensity of the glow curve. This is due to there being more carriers to recombine leading to an increase in total photon emission. A greater number of traps will lead to a greater amount of

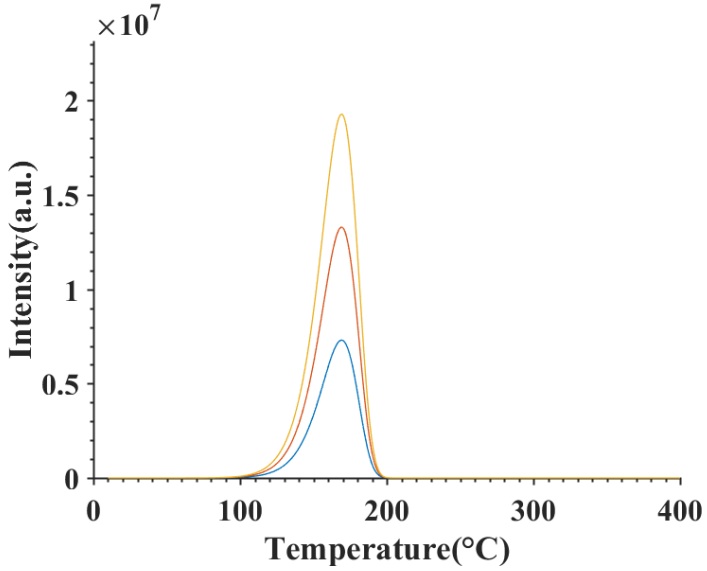


Figure 2.5: Example of how different trap densities effect the shape and position of a single order glow curve.

photons, but there is a limit. The material parameters of $E_t$ and $s$ are set by the nature of the trap in the material. The filled trap density of a material can be controlled by varying the amount of traps introduced into the material. And assuming that there is no interaction between these traps and they all have available recombination sites. In the case of a crystalline or polycrystalline solid, the amount would be limited by some fraction of the density of states of the material. The density of states will determine the maximum amount of possible traps. Often during the initial filling of traps caused by ionizing radiation not all of the traps will become occupied. Some traps will remain unoccupied, so the amount of ionizing radiation can also determine the amount of filled traps. This means that the filled trap density $n$ can depend on the amount of available traps and the amount of traps that are filled during the exposure to ionizing radiation. In practice exposing the sample to the appropriate ionizing radiation for 15 minutes is enough to fill all available traps. The trap density is so sensitive to the material it is placed in and the amount of traps filled by the initial irradiation that it is difficult to give a range of common values for it. The measured glow curve only indicates how many traps were filled and does not account for the unfilled traps. If it were possible to detect all the photons being emitted from a sample then the concentration of filled traps could

be measured but in practice this is impractical. There is also no guarantee that the linear heating during a measurement will empty all the filled traps. Oftentimes there will be residual thermoluminescence in subsequent measurements. Because of this, the sample can be kept at a high temperature after a measurement if additional measurements are going to be necessary to ensure that all the filled traps have been emptied. Varying the trap density in a material will increase the area under the glow curve so more photons are being emitted. This is different from the changing the parameters of $E_t$ and $s$ where the area under the glow curve remains constant.

So far, only material properties have been shown to have an effect on the glow curve. But the heating rate also plays an important role on the glow curve shape and position. Figure 2.6 shows examples of different heating rates when all the material parameters are

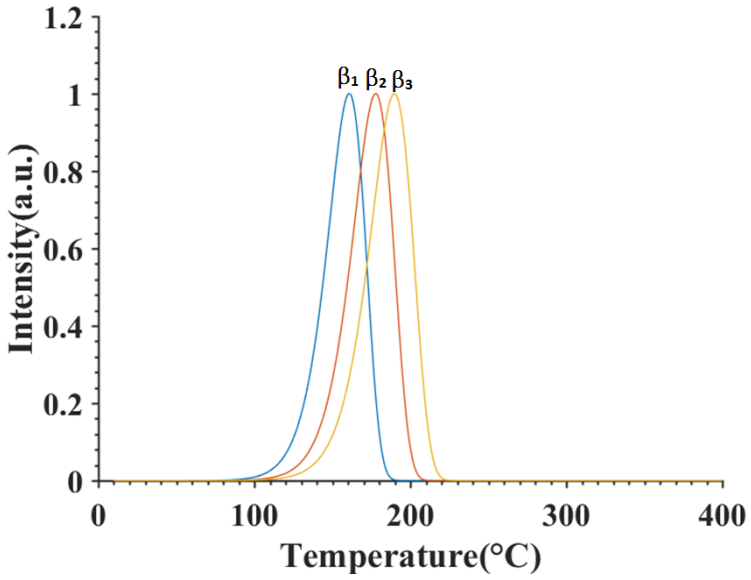


Figure 2.6: Example of how different heating rates effect the shape and position of a single order glow curve.

kept constant and assuming the same number of filled traps are emptying. The values for $\beta_1$, $\beta_2$, and $\beta_3$ are 1, 4, 10$^o$C/s respectively. The obvious difference between heating rates is that the glow curve peak shifts; the widths of the glow curves do not change. At first it may not be physically obvious why the glow curve peak would shift, but it depicts

how the heating rate will change the rate at which filled traps empty. Take for example a slower heating rate. If the heating rate is slower more time is spent in a certain range of temperatures. The effect on the measurement when considering this would be that the traps have more time to empty. So more traps empty at lower temperatures or earlier in the measurement. Similarly, if the thermoluminescent material is held at a constant temperature it will empty traps at a certain rate(decreasing). The longer it is held at this temperature the more traps will empty. Inversely, at faster heating rates the measurement spends less time at certain temperature ranges so the carriers have less time to empty. Because of this, the peak is shifted to higher temperatures because it requires more time to reach the peak emptying period indicated by the peak of the glow curve.

The only variable in Equation (2.7) that can be easily controlled is the heating rate $\beta$. It can easily be varied to shift the peak of the glow curve. A useful result in the ability to shift a glow curve is that the physical parameters can be calculated when glow curves from two or more heating rates are measured and compared. Two glow curves means two first-order equations and two unknowns $E_t$ and $s$. The filled trap density n0 will drop out during the process mentioned here. The first step in this process is calculating the derivative to Equation (2.7) as seen in Equation (2.8).

$$\frac{dI}{dT} = \frac{sn_0E_t}{kT^2}\exp(-E_t/kT)\alpha + sn_0\exp(-E_t/kT)\left(-\frac{s}{\beta}\right)\exp(-E_t/kT)\alpha \tag{2.8}$$

$$\alpha = \left[\frac{-s}{\beta}\int_{T_0}^{T}\exp(-E_t/k\theta)d\theta\right]$$

The second step is to identify the temperature at which the peak of the glow curve occurs by setting the first derivative equal to zero as seen in equation (2.9).

$$\frac{E_t}{kT_p^2} + \exp(-E_t/kT_p)\left(-\frac{s}{\beta}\right) = 0 \tag{2.9}$$

$$\frac{\beta E_t}{kT_p^2} = \exp(-E_t/kT_p) \tag{2.10}$$

And then equation (2.9) can be slightly rearranged to more easily identify the important components. The final result is shown in Equation (2.10) where $T_p$ is the temperature that corresponds to the peak of the glow curve. If two separate measurements are taken on the sample but at different heating rates then the values for $\beta$ and $T_p$ will differ but since $s$ and $E_t$ are physical constants for a given trap they will remain the same. Now there is a system of two equations with the two unknowns $s$ and $E_t$. The heating rates $\beta_1$ and $\beta_2$ are known because they were set during the glow curve measurement and the temperature location of the peaks $T_{p1}$ and $T_{p2}$ can be measured from the glow curve. The resulting system of equations is shown in Equations (2.11a) and (2.11b). At this point it would be useful to have the physical constants

$$\frac{\beta_1 E_t}{skT_{p1}^2} = \exp(-E_t/kT_{p1}) \tag{2.11a}$$

$$\frac{\beta_2 E_t}{skT_{p2}^2} = \exp(-E_t/kT_{p2}) \tag{2.11b}$$

$s$ and $E_t$ put in terms of the known quantities $\beta_1$, $\beta_2$, $T_{p1}$ and $T_{p2}$. A first step in doing this is to rearrange Equation (2.11b) as shown in (2.12). The next

$$s = \frac{\beta_2 E_t}{kT_{p2}^2} \exp(E_t/kT_{p2}) \tag{2.12}$$

$$E_t = \frac{kT_{p1}T_{p2}}{T_{p1} - Tp2} ln\left(\frac{\beta_1 T_{p2}^2}{\beta_2 T_{p1}^2}\right) \tag{2.13}$$

$$s = \beta_2 \frac{T_{p1}}{T_{p2}(T_{p1} - T_{p2})} ln\left(\frac{\beta_1 T_{p2}^2}{\beta_2 T_{p1}^2}\right)\left(\frac{\beta_1 T_{p2}^2}{\beta_2 T_{p1}^2}\right)^{\left(\frac{T_{p1}}{T_{p1}-T_{p2}}\right)} \tag{2.14}$$

step is to substitute $s$ in Equation (2.12) into Equation (2.11a) and then solve for $E_t$ to get an equation that equates $E_t$ to the known variables. The result of this is Equation (2.13). And finally Equation (2.13) can be substituted into Equation (2.12) to also get $s$ in terms of the known values. This result of the substitution is Equation (2.14). This equation is not a unique solution. Depending on what order the substitutions are done

in equation 11 will lead to a different result for Equation (2.14) but the result value for $s$ will be identical. Examination of Equations (2.13) and (2.14) can give a qualitative indication as to how a shift in the glow hint at the values of $E_t$ and $s$. Both equations contain a dependence on the inverse of the difference between the peak of the glow curves. Each also have the same logarithmic component which contains the ratio of the heating rates and squares of the glow curve peak temperature. The frequency factor also contains another term that is to the power of the inverse difference of the two glow curve peaks. This indicates that large changes in the range of orders of magnitude need to occur in the frequency factor for there to be a significant shift in glow curve peak temperature which was mentioned earlier.

## 2.3 Thermal Fading

Thermal fading in regards to the first-order kinetics model for thermoluminescence can give an explanation to why trap depths typically are greater than 1eV and why when held at room temperature most thermoluminescent samples show little thermoluminescence below 100$^{o}$C in practice. This can be understood by examining Equation (2.1). Even at room temperature(300K) there is still a significant non-zero probability that traps can empty. Although this probability will be very low even for traps shallower than 1eV, over time a significant number of traps will empty. This will lead to a decrease in the total number of filled traps thus causing a decrease in the intensity of the measured thermoluminescence. By starting with Equation (2.2) the same approached explained in [36] is used to describe how thermal fading will decrease the intensity of a thermoluminescent signal. The intensity of the emitted light is directly related to the decrease in filled traps. The first-order kinetics equation was found by using Equation (2.2) and assuming a linear heating rate and following the before mentioned steps. But a different viewpoint is going to be used here. In a practical scenario, any sample that is to be measured must obviously be stored somewhere. And in the case of thermoluminescence it may not be possible to do an immediate measurement after the initial exposure to ionizing radiation to fill the traps. Depending on the circumstances of the irradiation and measurement system, samples may need to be stored for hours, days or perhaps years at a time. Assuming these samples are kept at around 300K over these

extended periods of time it is valuable to know how this will change the intensity of the glow curve peaks. If the value of T in Equation (2.2) is kept at a constant room temperature it is possible to calculate the number of traps that will empty over a period of time. By taking the same approach as before and solving the differential equation but assuming a constant T this time the result is Equation (2.15). Assuming a constant T leads

$$n = n_0 \exp[-t \exp(-E_t/kT)] \tag{2.15}$$

to a simpler equation because there is no need to integrate the exponential. This leaves a value for the time t in the equation which is taken as the amount of time the sample is sitting at the constant temperature. Over this amount of time the initial value of filled traps $n_0$ is reduced at an exponential rate. The exponential lifetime of this decay is equation 16. In this model the rate of decay is dependent on the physical parameters of the trap, namely the frequency factor and trap depth. The decay is inversely proportional to the frequency factor and exponential proportional to the trap depth. A qualitative understanding of this dependence can be understood by going back to Figures 2.3 and 2.4. In these graphs the peak of the glow curve shifts to lower temperatures as the trap depth gets smaller and the frequency factor gets bigger. This is similar to what is happening in Equation (2.16). The lifetime of a carrier

$$\tau = \frac{1}{s} \exp(E_t/kT) \tag{2.16}$$

at a constant temperature will go up or down the same way as the glow curve peak shifts to higher or lower temperatures. This is all due to the willingness of a carrier to leave a trap depending on the frequency factor and trap depth. The intensity of the light emission from the thermoluminescent sample will drop when held in storage at a certain temperature and this can be estimated using (2.15) substituted back into Equation (2.2). Since the initial value for the filled traps is linearly related to intensity, the result is Equation (2.17).

$$I = I_0 \exp[-ts \exp(-E_t/kT)] \tag{2.17}$$

There is little difference between Equations (2.15) and (2.17) except the exchange of intensity for filled traps, but since the two are linearly related, this is to be expected. They both have exponential decays with the same lifetime. For a better understanding of how thermal fading changes the intensity of glow curves with different traps, take for example a thermoluminescent material that has three traps that all have the same filled trap density and frequency factor but have different trap depths, similar to the example illustrated in the band diagram of Figure 2.3, but in this example all three traps exist in the material but do not interact so that the measured glow curve is a linear combination of the single-order peaks from each of the traps as seen in Figure 2.7. The plots of Figure 2.7 are generated by using Equation (2.15) to calculate the new filled

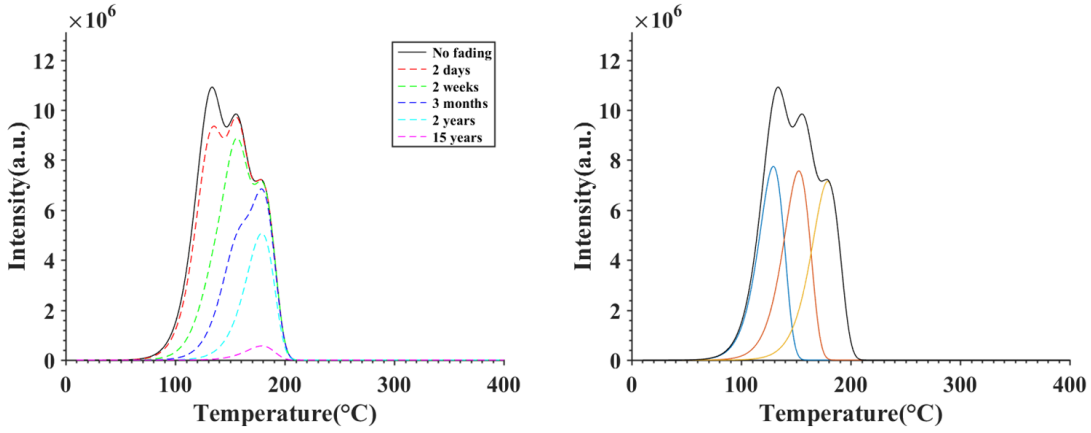


Figure 2.7: The plot on the left is the individual first-order peaks and the linear combination of the peaks. On the right are plots of the glow curve after different lengths of time, showing the effects of thermal fading.

trap density after a given time and then substituting into Equation (2.7). The amount of lapsed time t in Equation (2.15) used to generate the thermal fading plots are in seconds and correspond to lengths of time of 2 days, 2 weeks, 3 months, 2 years, and 15 years. These lengths of time were chosen to illustrate different stages that each first-order peak goes through. At the first time step of 2 days there is a significant decrease in the intensity of the lowest temperature peak. It is still distinguishable from the next higher temperature peak. The two higher temperature peaks remain relatively unchanged. This can be seen by how these two peaks still follow the none faded glow

curve. After about 2 weeks the lowest temperature peak has almost completely faded. The peak has not completely faded which is why the next higher temperature peak has a higher intensity than its individual first-order peak seen on the left side of Figure 2.7. Even though the peak is not longer visible it still is contributing to the glow curve but is overwhelmed in intensity by its neighbors. When 3 months have passed the second highest temperature peak has greatly decreased in intensity but is still has a visible effect on the shape of the highest temperature peak. The values for t corresponding to different thermal fading times can be substituted into Equation (2.15) to calculate the ratio of the intensities before and after thermal fading occurs. After 3 months the lowest temperature peak has decreased in intensity by 12 orders of magnitude making it a negligible part of the glow curve. The second peak drops to about 50% of its original intensity. The highest temperature peak has only dropped by about 4%, so it remains mostly unchanged by thermal fading at this point. After 2 years the second peak has dropped to about 1% its original intensity and the highest temperature peak has dropped to roughly 75% its original intensity. At 15 years the first two peaks have completely faded and only the highest temperature peak remains. This example shows that even over a small range of peak temperatures of $130 - 190^{o}$C the amount time it takes for thermal fading to take effect can range from a few days to several years. If there was a lower peak temperature, peak it might only take seconds to hours to completely thermally fade or if the peak was higher, it could take decades or centuries for these peaks to thermally fade. The practical significance of this result is that the amount of time between the initial irradiation of a sample and when the glow curve is measured may lead to a different measured result. When doing successive measurements of samples it is good to keep the time between irradiation and measurement constant. Also, it is possible to at least get qualitative information about the peak distribution of a sample by looking at the way thermal fading changes its glow curve. Unfortunately thermal fading does not offer specifics about the physical properties of the traps due to the fact that both the trap depth and frequency factor both shift and change the width of the glow curves but it can offer a starting point. Thermal fading can also be used to help verify results from Equations (2.13) and (2.14) which were used to calculate the trap depth and frequency factor when measuring a sample at different heating rates.

Another form of fading that will be only briefly mentioned here is anomalous fading.

Two examples of this are recombination by tunneling [38] and defect diffusion [39]. Recombination by tunneling can occur when a electron trap is in close proximity to a recombination center in a material. This frequently happens due to the random distribution of impurities and defects in a material. The electron can tunnel through the potential barrier blocking it from a recombination center and then recombine when it reaches the center. This can also lead to photon emission. Defect diffusion is caused by defects diffusing through a material which can cause filled traps to empty or otherwise nullify a trap or recombination center. Each of the forms of anomalous fading can alter the intensity of a single glow curve peak at a time because each glow curve peak is dependent on a single trap location.

## 2.4 Thermoluminescence of Multiple Trap States

So far, first-order kinetics with a single trap and recombination center have been used to describe the thermoluminescence process. But in reality the thermoluminescence process can be more complex when dealing with amorphous or polycrystalline materials. In the strictest sense any material that has defects is not perfectly crystalline. The case where a crystalline material happens to have defect concentrations to not change the crystalline structure but high enough to still introduce trap levels in the band gap would be a viable candidate for a single trap and recombination center model. In a polycrystalline material, the grain boundaries may introduce a continuum of trap states. This continuum of trap states could all lie within a certain energy range in the band gap making them "good" thermoluminescent traps. A "good" trap depth is one with an effective energy depth relative to the conduction band that makes it thermally stable at around room temperature but not so deep that too much heat is required to excite them out of the trap. Assuming that there is still only one recombination center and the electrons are unable to transfer from trap to trap means that each trap in the range of traps caused by the grain boundary can each be considered two have its own first-order glow curve. Another assumption that is made in this model is that each glow curve will have $n_0$ and $s$ but a range of values for $E_t$. The measured glow curve for a continuum of traps may appear to have a single peak but is in fact the linear combination of many peaks as seen in Figure 2.8. The model for multiple traps is the

summation of first-order peaks as seen in equation (2.18). The range of trap depths is $E_a < E_t < E_b$ with a spacing of $\Delta$E between

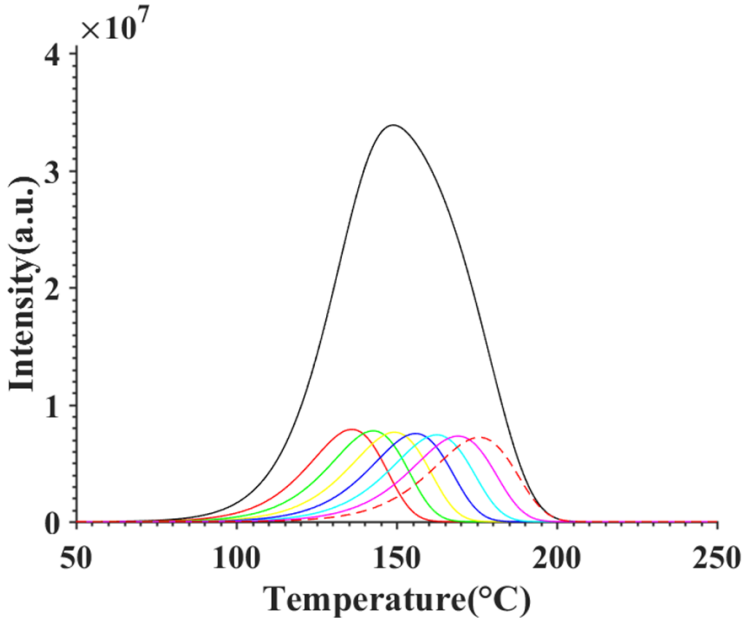


Figure 2.8: Example of a multiple trap glow curve with 7 traps that range in trap depth of 1.2 to 1.32eV with a spacing of 0.2eV. Each trap has the same frequency factor and trap density. These traps are assumed to not interact and have the same recombination center.

$$I(T) = \sum_{i=0}^{N-1} sn_0 \exp(-(E_a + i\Delta E)/kT) \exp\left[\frac{-s}{\beta}\int_{T_0}^{T} \exp(-(E_a + i\Delta E)/kT)dT\right] \tag{2.18}$$

each trap for N number of traps $E_b$-$E_a$=$N\delta$. This example of a finite number traps that are linearly spaced is the simplest model for multiple traps. More complicated models can include exponential and Gaussian spacing of the trap depths [36]. It is also possible to have a continuous or non-discrete range of traps with in an allowed range in the band gap. In that case the summation from Equation (2.18) now becomes an integral as seen in Equation (2.19).

$$I(T) = \int_{E_a}^{E_b} sn_0 \exp(E/kT) \exp\left[\frac{-s}{\beta}\int_{T_0}^{T} \exp(-E/kT)dT\right] \tag{2.19}$$

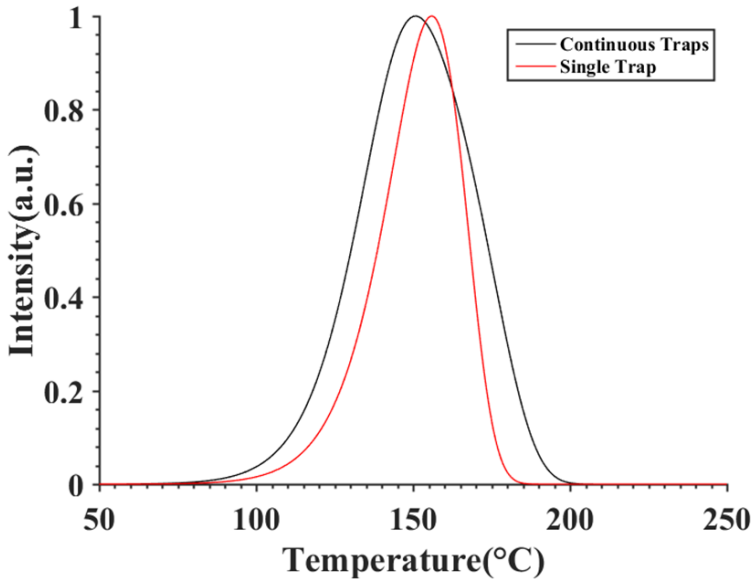


Figure 2.9: Glow curve for the linear combination of continuous traps between energies $E_a$ and $E_b$. The glow curve from the single trap case is also plotted for comparison.

A plot of Equation (2.19) is shown in Figure 2.9. Along with the plot of the continuous case is a single trap glow curve with a depth at the center of the trap range for the continuous plot. This is done to better show how the shape of the graph will change when using a continuous distribution of traps. The two graphs in this case are normalized because when every trap is emptied during heating each is allowed to recombine at the same center. Because of this the intensity of the glow curve will linearly increase with the density of trap states. The graphs in Figure 2.9 are normalized to allow for a better comparison of the graphs.

# Chapter 3

# Thermoluminescence of Lanthanide Doped Thin Films

## 3.1 Introduction to Lanthanide Doped Solids for Thermoluminescence

The luminescent properties of rare-earth doped yttria are well known [40–44]. These materials show luminescence due to the trivalent lanthanide in the yttria host. In particular, studies have been done on the cathodoluminescence [45], photoluminescence [46], and thermoluminescence [10, 47] of $Y_2O_3$:Tb. The studies conclude that the luminescence comes from the interaction of the trivalent terbium ion with the yttria crystal which introduces a luminescent center in the band gap of yttria. The emission spectra of terbium or other lanthanide dopants in a crystalline or polycrystalline host remains fairly constant. There are a couple reasons for this unique behavior. First is the electron shell arrangement of the lanthanide atoms. Before being placed in a host material and becoming ionized the filled shell arrangement for terbium is shown in the left side of Figure 3.1. Upon being placed in a crystalline host material the potential from the crystal is strong enough to remove the two 6s electrons and one 4f electron. The electrons that remain are shown on the right side of Figure 1. The outermost shells are now the 5s and 5p shells. The 4f shell can now be considered as an inner core shell. Due to the arrangement of the shells 5s and 5p they effectively screen the 4f shell from

$$[Kr]4d^{10}5s^25p^64f^96s^2 \qquad [Kr]4d^{10}5s^25p^64f^8$$

Figure 3.1: (Left) The filled shell arrangement for terbium before it is introduced into a host material. (Right) The shell arrangement for terbium after it has been introduced into a host material for example yttrium oxide. The [Kr] stands for the electron shell arrangement for krypton.

the electric field from the crystal [48]. This screening effect leaves the 4f shell mostly unperturbed by the surrounding crystal field. This means that the 4f shell will act the same regardless of the surrounding fields due to the host material. The screening of the 4f shell allows for the second unique feature of lanthanides which is the intraband transitions. Normally intraband electric dipole transitions are forbidden. However, in the case of most lanthanides, the 4f-4f transition is the cause of the strong and narrow spectral lines. But since this transition occurs within the 4f energy band, it should be forbidden according to quantum mechanical selection rules. Specifically, the Laporte selection rules state that there must be a 1 change in orbital and total orbital angular momentum, spin must be conserved and there must be a change in parity. In this case the parity rule is broken because it remains the same during the transition. The magnetic dipole interaction does not require a change in parity but because it is so weak it cannot account for the intensity of the spectral lines seen from lanthanides. The Judd-Ofelt theory[13] states that if a higher order band such as the 5d(even parity) band is "mixed" into the 4f(odd parity) band than the parity selection rule is satisfied, allowing for an electric dipole transition to occur. The two states that are "mixed" are the $4f^N$ and $4f^{N-1}5d$ states where the N stands for the number of electrons in the trivalent lanthanide f shell which for example would be 8 as mention previously. The $4f^{N-1}5d$ state is where an electron moved from the f shell to the d shell. This state has an even parity and is "mixed" with the odd parity 4f state. The resulting $4f^N$ states with the $4f^{N-1}5d$ states "mixed" into them allow for the 4f-4f transitions. The reasoning for why these states are allowed to be mixed are beyond the scope of this discussion on lanthanide doped materials. What is most important to take from this is the before mentioned narrow spectral lines that remain at a fairly constant wavelength when the lanthanide is placed is various types of solids.

Thermoluminescence has been used to characterize the energy levels introduced by

lanthanides into various host materials [49–52]. In most thermoluminescent measurements wide band gap(greater than 5.5eV) materials are chosen as a host material for dopants and possible defects. As mentioned in chapter 2 thermoluminescence is highly dependent on the defects that exist in the case of a (poly)crystalline host material. Usually these defects are random so they are difficult to reproduce. This makes it difficult to consistently fabricate TL materials that have the same glow curve from batch to batch. Lanthanides give the possibly of being able to introduce traps in the band gap that have a predictable behavior due to the fact that the 4f shell which determines the luminescent behavior of the lanthanide is shielded from the host material. The lanthanide traps in the band gap can act both as an electron trap and/or recombination center. Figure 3.2 is an example of the host material $YPO_4$ [48] in a powder form where many thermoluminescent measurements were taken each with a different lanthanide dopant. What the authors of the work

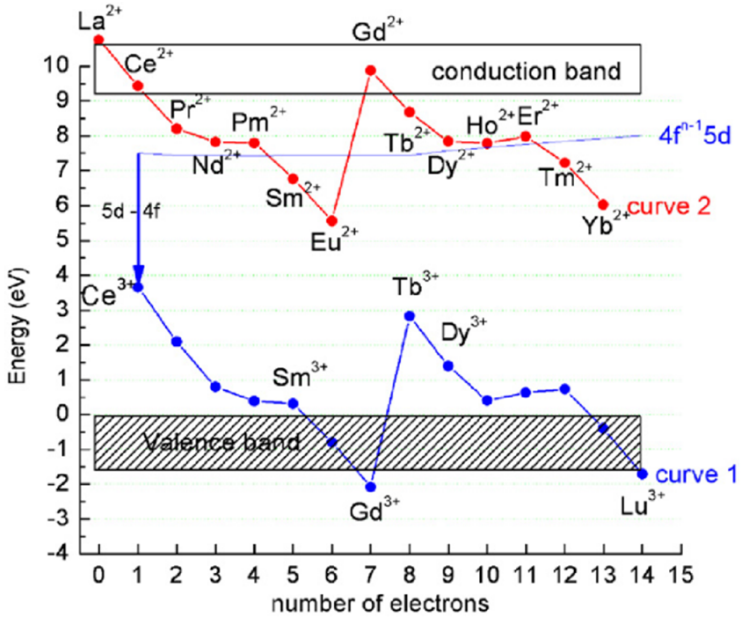


Figure 3.2: Example of energy levels for various lanthanides in $YPO_4$ [12](direct replica from source). In this example the authors found that $Ce^{3+}$ acted as a hole trap and $Nd^{3+}$, $Sm^{3+}$, $Dy^{3+}$, $Ho^{3+}$, $Er^{3+}$ and $Tm^{3+}$ can act as electron traps.

found was that the trivalent cerium dopant acted like a hole trap and many of the other lanthanides such as neodymium and samarium would act as electron traps. For the

measurements they would add cerium along with one of the other lanthanides that could act as an electron trap. Upon irradiation with an ionizing source cerium would gain a hole and the other lanthanide would gain an electron. This fits nicely with the single trap and single recombination center model mentioned in chapter 2. When the glow curve was measured the thermal energy would release a trapped electron into the conduction band where it could then be free to recombine at the cerium site. The confirmation of the recombination site actually being cerium was confirmed by characteristic emission peaks for cerium of 338 and 352nm. Figure 3 shows the resulting glow curves from the co-doping of cerium with

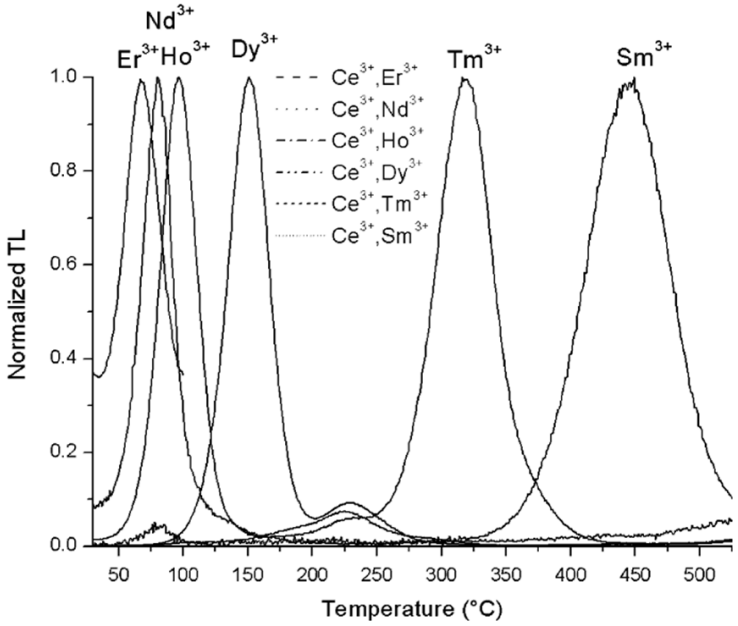


Figure 3.3: Separate Glow curves of $YPO_4$ co-doped with cerium and several other lanthanides[12] (direct replica from source). There is an obvious correlation between the peak glow curve in each case and the trap depths shown in Figure 3.2. Electron traps farther from the conduction band correspond to glow curves with peaks at higher temperatures.

several of the other lanthanides mentioned Figure 3.2. It is obvious when comparing Figures 3.2 and 3.3 that there is a correlation between the depth of the electron traps and the position of the peak temperature for different glow curves. As the electron traps get deeper, the corresponding glow curve shows a peak at a higher temperature. This

matches with what is expected from the first-order kinetics equation for thermoluminescence. The only discrepancy here is that the dysprosium has a higher temperature peak than the neodymium. This can be explained by recalling that the frequency factor in the first-order kinetics equation can also shift the glow curve peak. If these measurements where done on a different host material with the same dopants a similar pattern in the arrangement of trap levels in the band gap would appear. For instance the $Eu^{2+}$ energy level would always be below $Dy^{2+}$, and $Sm^{2+}$ would always be below $Tb^{3+}$. What would change with a different host material are the relative positions of curves 1 and 2 with respect to the conduction and valence band. The predictability of the lanthanides regardless of the host material they are in make them useful as traps or recombination centers for thermoluminescent testing and applications.

## 3.2 Deposition and Measurement Processes of a TL Thin Film

Most thermoluminescent(TL) thin films are grown using techniques , such as spray pyrolysis [53] and sol-gel [54] methods, that are not part of standard silicon integrated circuit processes. Conversely, the overwhelming majority of thermoluminescent materials will not display thermoluminescence when deposited in the same manner as a microelectronic film. Yttrium oxide is well known as a material that is deposited as a polycrystalline film [55]. And since this film can be deposited using e-beam evaporation [45] it can be used in standard microfabrication processes. When using a powder as the source material for electron-beam evaporation, it is simple to include dopants into the host powder by mixing the two powders together before evaporation. The combination of strong polycrystalline and luminescent characteristics of $Y_2O_3$:Tb make it a good candidate for an integrated circuit thermoluminescent thin film. In the example shown here electron-beam evaporation is used to deposit a thin film of $Y_2O_3$:Tb, which can be deposited in a simple evaporation process and luminesces brightly after exposure to radiation and subsequent heating. Rare earth [40–47] and transition metal[11] impurities can be added to yttria to improve the luminescence. The dopant can be added during deposition by including small amounts of it in the host material of the electron-beam source. As the electron beam strikes the source it will evaporate both the host material

and impurity. With a subsequent annealing the polycrystalline grains can be grown and the impurities in the film activated. Unlike the previously mentioned spray pyrolysis and sol-gel methods this technique does not require the careful mixing of chemicals. The powders for the host material and impurity are blended and then compressed into pellets. The pellets are then ready for evaporation. $Y_2O_3$:Tb films were deposited on (100) silicon substrates. $Y_2O_3$(99.99%) and $Tb_4O_7$ (99.9%) powders were used as evaporation sources. The terbium oxide powder was mixed with the yttrium powder with a molar concentration of terbium in the mixture of 0.1%. The resulting powder was a homogenous blend of the $Y_2O_3$ and $Tb_4O_7$ powders and was then compressed into pellets. The pellets were 1cm in diameter and approximately 0.5cm thick. The pellets were then placed in a graphite crucible liner for e-beam evaporation. In order to prevent possible contamination of carbon particles from the crucible liner, the inside of it was wiped with a polycellulose wipe several times until very little carbon appeared on the wipe. Approximately 15 grams of pellets were used in each deposition run. It was important to have the source material stacked over the top of the crucible liner rim so that the electron-beam could easily reach it. If the source material is too low in the crucible, deposition rates will drop due the e-beam not hitting the source with enough power to evaporate it properly. The source material in the graphite crucible could only be used 2 to 3 times before it would no longer be useful for evaporation. After each thin film deposition the remaining yttria would appear black and glassy. It is possible that the black color was due to oxygen vacancies in the yttria which caused the light to be absorbed [56]. After the 2 to 3 runs the source material would be too far below the edge of the crucible to be useful. When this happened a new mixture would have to be mixed and compressed into pellets. The electron beam system used for evaporation was a Varian model number 3118. The voltage and current during evaporation were 4.19kV and 0.2A respectively. A slow deposition rate of 2-3/s was used to promote crystal growth. Since the source material was not solid, but rather consisted of pellets, the deposition rate fluctuated considerably. The fluctuation can be attributed to the uneven density of the pellets in the crucible. The beam position would need to be regularly changed in order to sustain a constant deposition rate.

A quartz crystal monitor was used to keep track of the thickness of the film, which had a final thickness of 350nm. This particular quartz monitor did not have settings

to measure the deposition rate of yttria. Several test runs were done at the before mentioned power settings for specific amounts of time. The sample used for thickness measurements was a glass slide with a piece Kapton tape wrapped around it in several places along the length of the glass slide. After the film deposition onto the glass slide the Kapton tape would be carefully peeled off leaving a section of the glass side which did not have the yttria deposited on it. A P-16 profilometer was then used to measure the step height between the spots on the slide where there was a boundary between the yttria film and where there was none due to the Kapton tape blocking that area during deposition. After the film was deposited, it was cleaved into four smaller samples and was annealed using a Modular Pro RTP-600S. Each sample was annealed at different temperatures for different amounts of time. These temperatures and times are listed in Table 3.1. The reason for the different temperatures was to

| Temperature(°C) | Time(s) |
|---|---|
| 300 | 300 |
| 600 | 300 |
| 900 | 120 |
| 1100 | 30 |

Table 3.1: Annealing temperatures and times for the $Y_2O_3$:Tb thin films deposited by e-beam evaporation onto (100) p-doped silicon wafers. The choice of anneal times are based on the maximum amount of time allowed at the corresponding temperature. Any longer and it may damage the RTA.

find the minimum temperature required in order to achieve a thermoluminescent signal during measurement. Each sample film was annealed under argon gas with a flow rate of 4sccm preceded by a two minute argon purge. The samples were also annealed in an oxygen gas. When the oxygen gas was used later thermoluminescent measurements did not show any signal. Possible reasons for this will be discussed in the next section. The silicon wafers with the $Y_2O_3$:Tb thin films were then cleaved into 2cm x 2cm squares for measurement.

Three ionizing radiation sources (ultraviolet, x-ray, and gamma) were used to fill the traps of the $Y_2O_3$:Tb. The UV source was a deuterium lamp with no filter; the x-ray source was an XRAD-320 with a 2mm Al filter; the gamma radiation source was a $^{137}$Cs radioisotope. Measurements of thermoluminescent intensity versus temperature

were taken using a photomultiplier tube (PMT) Sens-Tech P25PC as a detector. The quantum efficiency began to sharply drop off after about a 600nm photon wavelength and eventually reached zero at 650nm. Because of this any emission above 600nm will be strongly attenuated and anything above 650nm will not be detectable by the PMT. The internal default heating rate for our hotplate (with a 115Vrms) is 2.7$^o$C/s, so this ramp rate was used to measure our TL glow curves. When applicable for some of the measurements, a 550nm cut-on short pass optical filter was used. The filter was placed directly in front of the PMT. The filter greatly attenuated the black body signal allowing for the measurement of high temperature peaks above 350$^o$C. The emission spectra of the thin film was measured using a Spectral Products CM-110 monochromator. The monochromator was placed in front of the PMT and

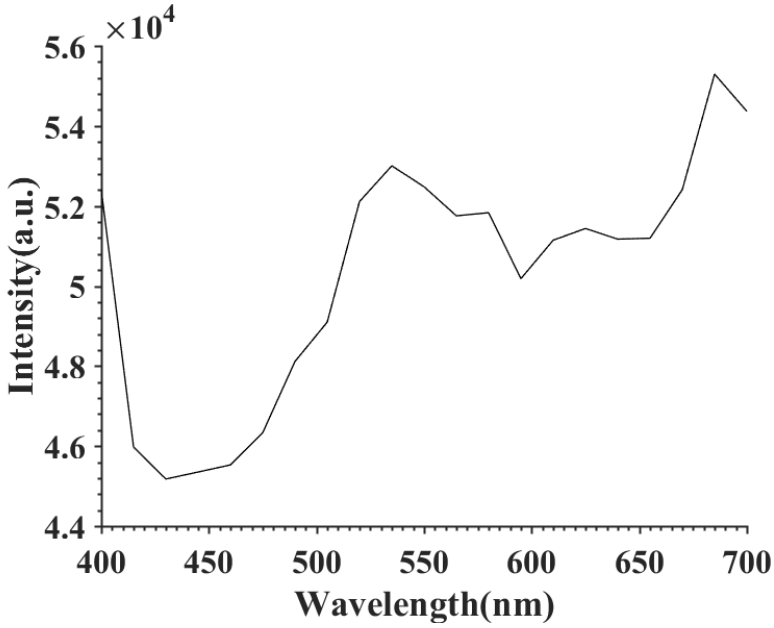


Figure 3.4: Results of bleach testing of the $Y_2O_3$:Tb sample. Bleaching of a sample is when exposed to light before a measurement it reduces the intensity of the thermoluminescent signal. The sample is most sensitive to wavelengths between 415 to 550nm.

set to a series of wavelengths. Each wavelength was incremented 3nm for 100 subsequent TL measurements until the full range from 400 to 700nm was covered. Additional scans were taken of the peak at 490nm in 1nm steps to increase resolution of the peak.

Bleaching affects were also measured. Bleaching occurs when the intensity of the thermoluminescence (usually corresponding to emission at lower temperatures) decreases due to exposure to light after irradiation. The bleaching measurement was carried out by placing a monochromator in front of a tungsten-halogen lamp. And in a similar manner to the emission spectra measurement the set wavelength of the monochromator was incremented in 15nm steps. The bleach testing was also done between 400 to 700nm. Figure 3.4 shows the results of the bleach testing.

## 3.3 Thermoluminescence and Characterization of TL thin Film

| Material | Crystallinity | TL response | Peak location(s) | UV sensitive |
|---|---|---|---|---|
| $Y_2O_3$:(Tb); (Tb, Er); (Tb, Yb);(Tb, Eu) | polycrystalline | strong | 130°C, 250°C | yes |
| $Y_2O_3$:Tb, Ce | polycrystalline | weak | 130°C | yes |
| $Y_2O_3$:(Ce);(Ce, Yb);(Ce, Er) ; (Pr) ; (Nd);(Dy);(Er);($DyI_3$) ; ($DyF_3$) | polycrystalline | none | n/a | n/a |
| $ZrO_2$ | polycrystalline | none | n/a | n/a |
| $ZrO_2$:Tb | polycrystalline | weak | 110°C | yes |
| $CeO_2$:();(Er);(Tb) | polycrystalline | none | n/a | n/a |
| MgO:(Ce);(Tb) | amorphous/ polycrystalline | none | n/a | n/a |
| $CaF_2$:Dy (TLD-200) | amorphous/ polycrystalline | none | n/a | n/a |
| LiF:Mg,Ti (TLD-100) | amorphous | none | n/a | n/a |
| CaO | amorphous | none | n/a | n/a |
| YAG:Ce | amorphous | none | n/a | n/a |

Table 3.2: Attempted TL thin films using the process described in section 3.2. The table lists crystallinity, relative strength of TL response and sensitivity to UV light from the deuterium lamp. Of all the above tested thin films only $Y_2O_3$:Tb showed a strong TL signal.

The process used to deposit the $Y_2O_3$ was also used to deposit many other lanthanide doped thin films. The results of the other attempted materials are listed in table 3.2. The only thin film that showed strong thermoluminescence was $Y_2O_3$:Tb. The graph of the glow curve from the UV radiation source is shown in Figure 3.5. This is after 15 minutes of irradiation.

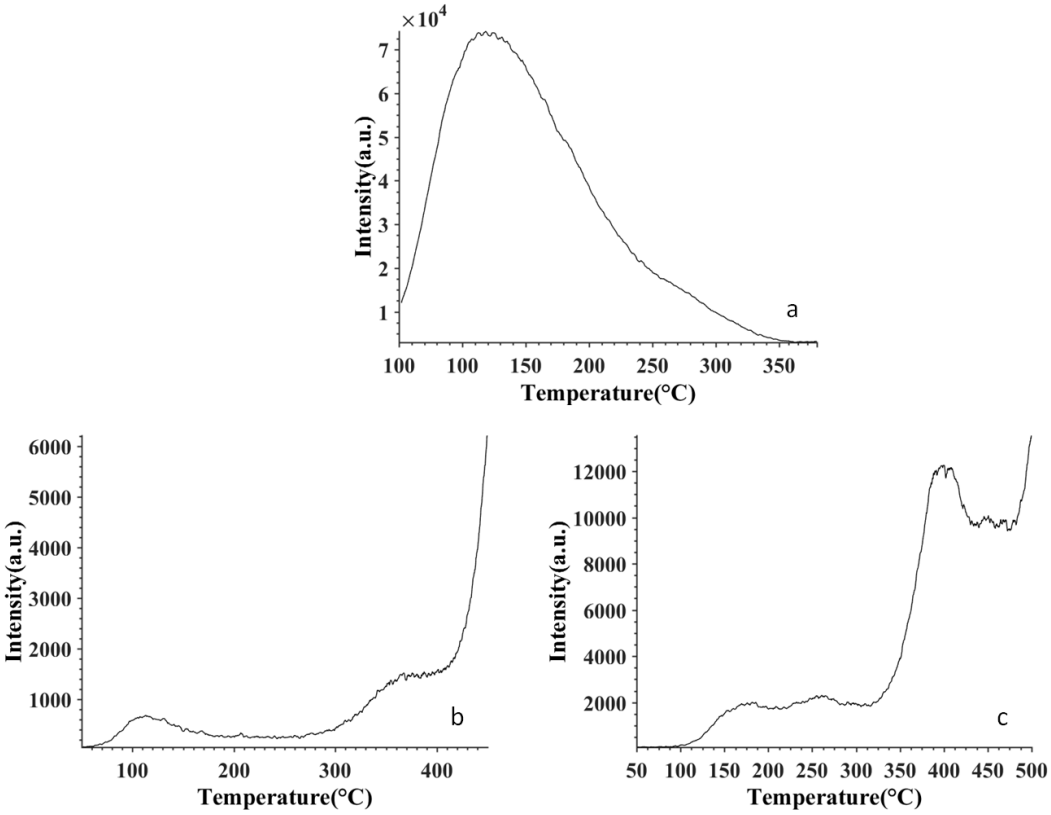


Figure 3.5: Glow curve for $Y_2O_3$:Tb (a) 10 seconds after UV irradiation. There are two peaks at 140$^o$C and 230$^o$C. (b) 30 minutes after x-ray irradiation with peaks at 120$^o$C and 360$^o$C. (c) 1 hour after gamma irradiation with peaks at 170$^o$C, 260$^o$C, and 410$^o$C. The exact reason for the difference in these glow curves is unknown but maybe due to the generation of more free carriers allowing for more traps to fill or possibly deeper level traps are created from the higher energy photons.

Longer irradiation times had no effect on the intensity of the glow curve. The thermoluminescence glow curve of the UV irradiated sample was measured 10 seconds after irradiation. There are glow curve peaks at 140$^o$C and 230$^o$C. These peaks indicate that

there are at least two traps in the band gap of yttria that are deep enough to be thermally stable at room temperature. These trapping centers could be due to defects in the film, terbium ion, or surface states. The terbium ion may act as both an electron and hole trap similar to $Dy^{3+}$ in $YPO_4$ [48]. From the spectral emission peaks mentioned later, the terbium ion always acts as the recombination center because the spectral peaks match the intraband transitions in the terbium ion [46]. $Y_2O_3$:Tb also had a glow curve after being irradiated by the before mentioned gamma and x-ray sources as seen in Figure 3.5. And under these higher energy radiation sources a peak at 410$^o$C was measured using the 550nm short pass

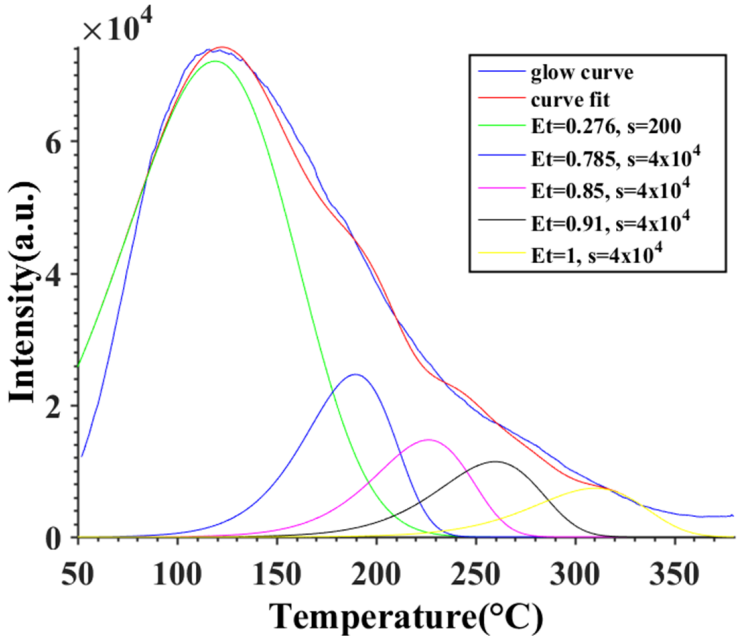


Figure 3.6: An attempt at determining the number of traps and their physical paramters $E_t$ and s was made. The peaks are not based off on physical measurements but are rather curve fits.

filter. The glow curves for gamma and x-ray sources do show a peak at 170$^o$C and 120$^o$C respectively indicating a sensitivity to these forms of ionizing radiation; however, the UV source in our laboratory is much more accessible to our group; therefore, the glow curves used in the rest of the paper will be the result of UV irradiation. The UV source was used because it allowed for more rapid measurements. The x-ray and gamma

sources require the sample to be moved after irradiation where as the UV irradiation

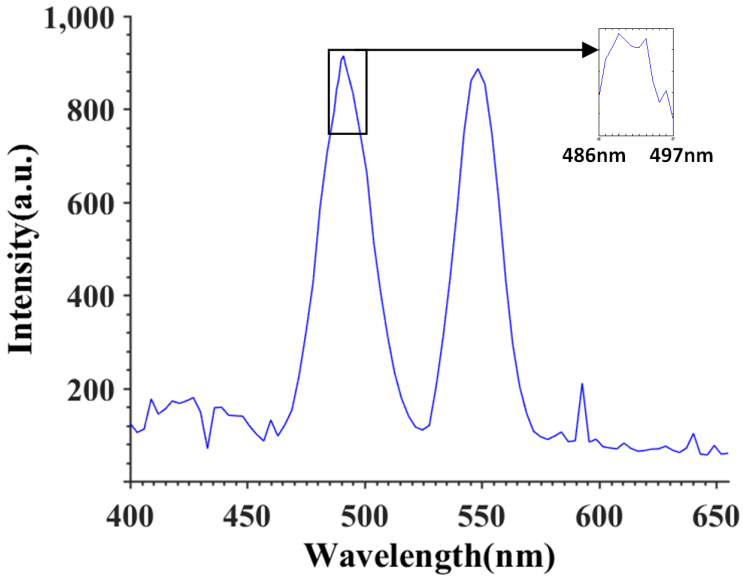


Figure 3.7: Emission spectrum of $Y_2O_3$:$Tb^{3+}$. The two main peaks at 490nm and 540nm correspond to the $^5D_4$ to the $^7F_5$ and $^7F_6$ levels respectively.

can be done while the sample is on the hot plate. An attempt at determining the number of traps and their physical paramters Et and s was made. The results are shown in figure 3.6. $Y_2O_3$:Tb grown by other methods [45] [46]. The two main peaks at 490nm and 540nm involve 4f-4f transitions of the $Tb^{3+}$ ion [46]. The 490nm and 540nm peaks correspond to the $^5D_4$ to the $^7F_5$ and $^7F_6$ levels respectively. There are characteristic peaks at 585nm and 618nm that do not appear or are difficult to attribute in Figure Figure 3.7. This is most likely because the signals are relatively too weak for the PMT to detect, given the intensity of the other peaks and the extremely small volume of material in the film. In Figure 3.6 the peak at 585nm is uncharacteristically sharp for this emission peak relative to others reported in the literature, and in Figure 3.7 it exists for only a very small temperature range around 200$^o$C, which is also unusual. While this could certainly be a contribution from the 585nm TL emission, it is so weak relative to our noise level that we will ignore it for the remainder of this work. Figure 3.8 is a 3D rendering of the relationship between temperature and emission wavelength. One can separate the 490nm and 540nm emission peaks into two plots of thermoluminescence

versus temperature. When the two plots are compared, they appear almost identical. This indicates that the emission spectrum is not significantly temperature dependent and the recombination center is largely independent of the trap energies.

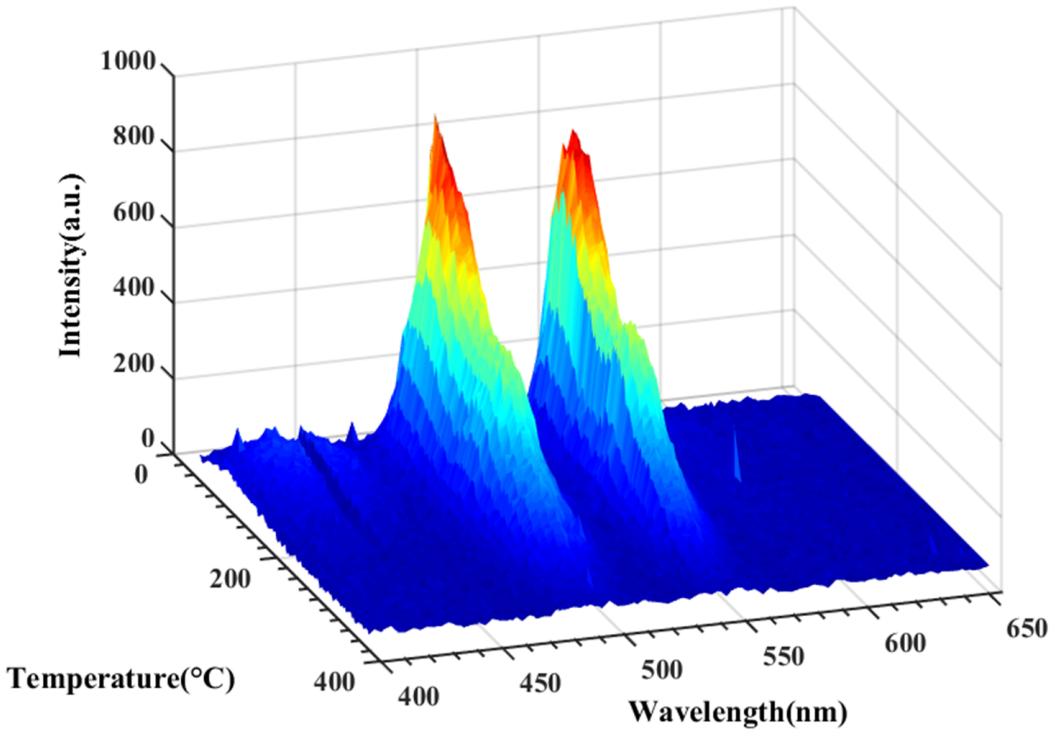


Figure 3.8: 3D rendering of the wavelength and temperature dependence of the emission spectra of $Y_2O_3$:Tb. The two emission peaks have largely the same relative intensity at all temperatures.

There is a minimum annealing temperature required in order for the $Y_2O_3$:Tb to become thermoluminescent. This requirement is closely related to the onset of crystallinity in the film as depicted in Figure 3.9. The characteristic crystal planes indicate that this is (poly)crystalline yttria. The reflection planes[14] indicative of $Y_2O_3$:Tb are also labeled in Figure 3.9. X-ray diffraction was used to measure the crystallinity of the film after several different annealing temperatures. It can be seen from the XRD peak intensity that the film becomes more (poly)crystalline with increased annealing temperature. The thin film does not become thermoluminescently active until a $900^oC$ anneal for 2 minutes. Beyond this, the intensity of the thermoluminescence increases with annealing

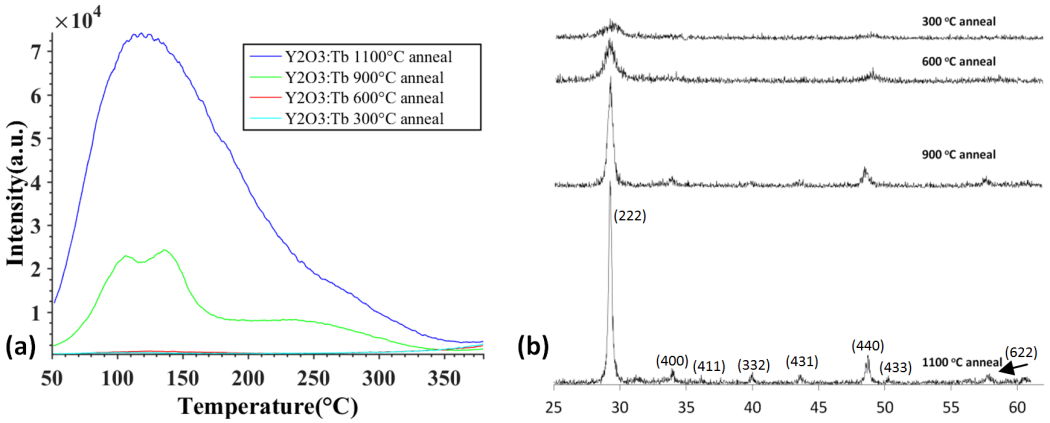


Figure 3.9: (a) Glow curves for different annealing temperatures. The two glow curves for the 600$^o$C and 300$^o$C are plotted but are essentially invisible against the x-axis because they are so weak. (b) XRD measurements for different annealing temperatures. There is an obvious correlation between the intensity of the XRD peaks and intensity of the glow curves. The XRD peaks increase in intensity with increasing annealing temperature.

temperature. This is probably due to an increase in crystal grain size and activation of the $Tb^{3+}$ ion. The XRD data of Figure 3.9 indicates that with higher annealing temperatures, the peaks increase in intensity, implying an increase in the(poly)crystallinity and grain size of the material. As the crystal grain size increases, more of the $Tb^{3+}$ ions are incorporated into the cubic bixbyite [55] crystal structure. Rutherford backscattering spectrometry(RBS) was used to measure the impurity concentration of terbium in the yttria thin film. A graph of the RBS measurement is shown in Figure 3.10. The concentration of the terbium was determined by calculating the area under the yttrium and terbium peaks. The scattering cross sections of the terbium and yttrium peaks are then used as a weighting factor on the area under the peaks. The ratio of the weighted areas will be the relative concentrations of atoms in the material. Since the XRD measurement indicates that the $Y_2O_3$ is at least partially crystalline, we have assumed a stoichiometric material and calculated the oxygen concentration accordingly from the yttrium concentration. The ratio of yttrium to terbium indicates a 1% concentration of terbium. This is 10 times more than the concentration in the source material, and is probably due to the higher vapor pressure of terbium oxide relative to yttrium oxide during the evaporation process. The higher concentration maybe due to the slightly

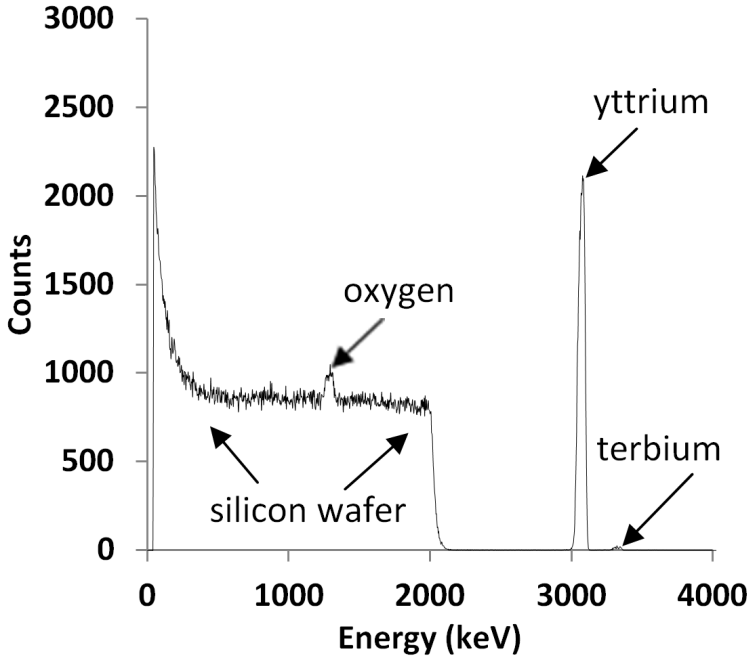


Figure 3.10: RBS measurement of $Y_2O_3$:Tb. The RBS data shows the peaks for oxygen, yttrium and terbium, each of which are labeled. The large flat portion represents the 550um thick silicon wafer.

higher melting point of yttria being 2425$^o$C and terbium oxide 2340$^o$C. Thermal fading has a significant effect on the $Y_2O_3$:Tb. Figure 3.10 shows an example of the thermal fading. The thermoluminescent intensity peak fades by 75% after 10 minutes and 50% after 1 hr. For visible light with wavelengths shorter than 500nm, light will begin emptying traps that were filled during irradiation. This effect is weakly seen across the 500nm to 700nm range of visible light but is more apparent at shorter wavelengths. Thermo Scientific. The thin film was 2x2cm and 350nm thick and the TLD-100 chip was 6.4x6.4x0.89mm. The mass of the $Y_2O_3$:Tb and TLD-100 were 7.01x10$^{-4}$g and $9.64x10^{-2}$g respectively. The max intensity of the UV irradiated $Y_2O_3$:Tb glow curve and x-ray irradiated TLD-100 is 7.42x10$^4$ and 5.84x10$^6$ respectively. The calculated luminescent intensity per unit mass for the $Y_2O_3$:Tb and TLD-100 is 1.06x10$^8$ and $60.6x10^6$ respectively. The $Y_2O_3$:Tb has about 2 times the luminescent intensity per unit mass of the TLD-100 when UV irraddiated. The comparison can be seen in Figure

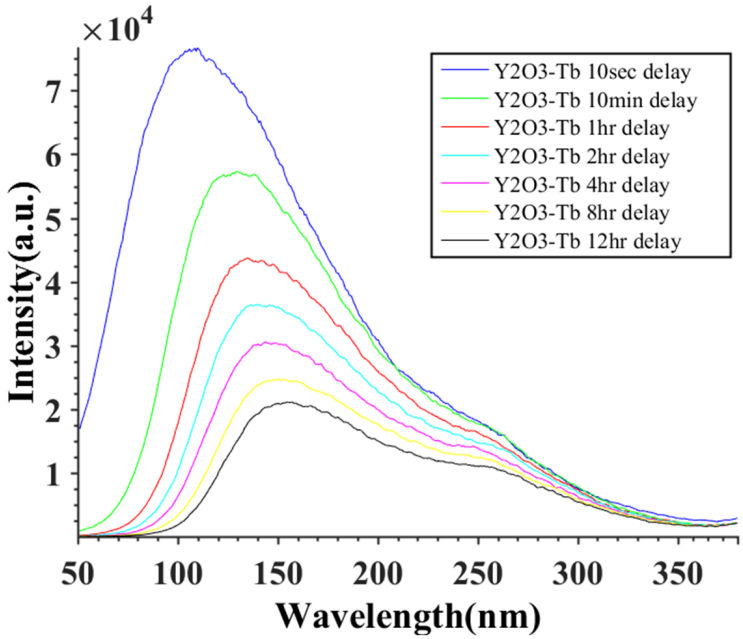


Figure 3.11: Thermal fading of a Tb-doped $Y_2O_3$:Tb thin film. This film was evaporated as described in the text, then annealed at 1100$^o$C. After UV irradiation, the glow curve was taken sequentially at different delay times as shown in the legend. As is commonly seen in many TL materials, there is significant thermal fading of the lower temperature regions of the glow curve while the higher temperature regions show much less.

3.12 between $Y_2O_3$:Tb and TLD-100 irradiated with 25Gy x-ray. The luminescent intensity per unit mass of the TLD-100 thin film was 37 times as intense as the $Y_2O_3$:Tb for x-ray irradiation.

An important feature to note about the $Y_2O_3$:Tb fabrication process described in this chapter is that it can lead to slightly different thermoluminescent characteristics. Some differences that can occur from batch to batch are the shape and position of the glow curve and the intensity of the signal. The difference in peak position is only a few degrees and intensity change of no more than about 10%.

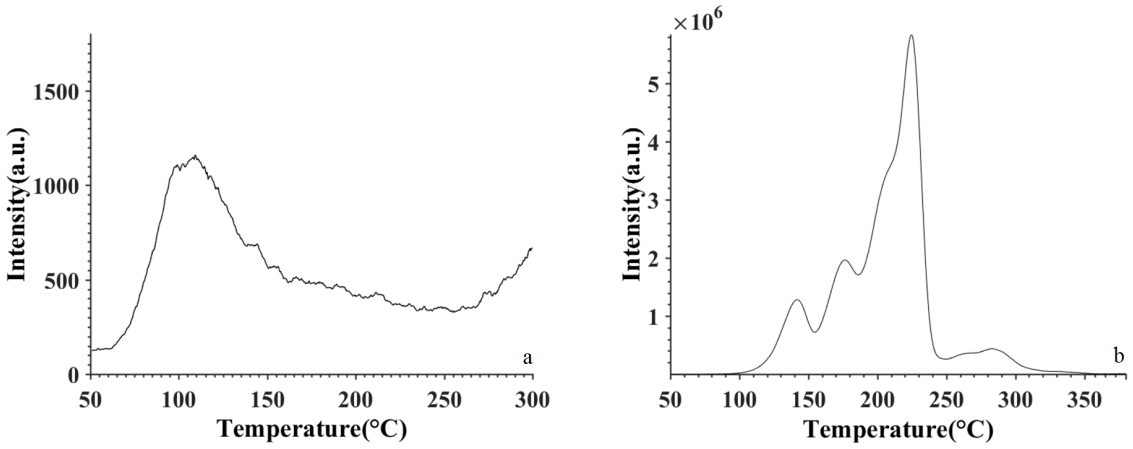


Figure 3.12: TA comparison between the intensities of the $Y_2O_3$:Tb thin film and TLD-100 from the company, Thermo Scientific. a) The glow curve for $Y_2O_3$:Tb after 25Gy of x-ray irradiation. b) The glow curve of TLD-100 after 25Gy of x-ray irradiation. The glow curve for the $Y_2O_3$:Tb is much weaker than that for TLD-100 but the mass of the $Y_2O_3$:Tb thin film is much less than the TLD-100 chip from Thermo Scientific. The luminescent intensity per unit mass was 37 times greater for the TLD-100.

# Chapter 4

# Reduced Thermal Emission Microheaters

## 4.1 Two Proposed Methods for Reducing Thermal Emission from Microheaters

Micromachined heaters have applications in a wide variety of high temperature processes such as carbon nanotube growth [57], gas sensing [58–60], microfluidics [61] and measuring thermoluminescence [62–66]. Unfortunately, traditional microheater designs are incompatible with measurements of low levels of light at high temperatures. Measuring faint signals of luminescence at elevated temperatures can be extraordinarily difficult because of the large amount of thermal background radiation emitted from heating elements. Typically, to mitigate background emission when monitoring material fluorescence, one must use a cutoff filter that blocks all but the shortest wavelengths, leaving only high energy UV fluorescence centers to be probed at very high temperatures, and even these are swamped when heating elements reach temperatures beyond several hundred $^{o}$C.

Two methods are described here to create microheaters that emit very little background radiation. The first method alters the heater design such that a large central region is composed solely of infrared transparent materials. Kirchoffs Law, which states that the thermal emission of a material is exactly equal to its absorption, requires

that the background emission be negligible. In theory, this central region could also be composed of highly reflective materials, but metals become more emissive at higher temperatures. The second method applies Kirchoffs Law to a multilayer stack on the top and bottom of the microheater. The multilayer stack has a high reflectivity in the wavelength range of interest, therefore it can change the emissivity of the microheater/multilayer body in that spectral range [67].

The first method of using infrared-transparent materials in the center of a heater with an aperture to block the emission from the heating coils has the advantage of being able to block all wavelengths from the thermal radiation of the metal heating element. While in the second method the multilayer structure can only block a range of wavelengths depending on the thickness of the layers in the stack and the number of layers. One disadvantage to the first method is that it requires an aperture to be properly aligned with the center of the microheater and since the center of the microheater does not have a heating element, there will be non-uniform heating from the center to edge of the heater. The multilayer microheater has uniform heating and does not require any careful alignment.

## 4.2 Design and Fabrication of Microheaters

The microheaters that were used in this study were composed of platinum heating elements on released alumina platforms. These materials have been used in previous work on microstructures operated at high temperature [68, 69]. In [68] a Pt paste was deposited on an $Al_2O_3$ substrate and patterned using laser sintering. The method used in [69] was to deposit $Al_2O_3$ by reactive sputtering and then deposit Pt by DC magnetron sputtering. Both of these methods result in a microheater that operates without being released from the substrate. In the microheaters mentioned here they consisted of 300µm x 300µm and 500µm x 500µm alumina platforms suspended by four legs with a platinum heating element on the platform. The material for the platform was chosen to be $Al_2O_3$ because of its low thermal conductivity and high melting point. Platinum was chosen for the heating element because it has a relatively high melting point along with a linear temperature coefficient of resistance over a wide range of temperatures. This microheater design allowed for good thermal isolation allowing the microheaters to

reach high temperatures at small amounts of current. The length and cross sectional area of the legs was chosen to decrease thermal conductance while maintaining mechanical stability. Power loss at very high temperatures in the microheater primarily comes from radiative losses which exceed thermal conduction losses to the substrate.

The microheater fabrication process starts with deposition of 100nm $Al_2O_3$ by atomic layer deposition(ALD) onto a standard 4 in. p-type (100) silicon wafer. This first layer $Al_2O_3$ will act as the primary structural support for the microheater. The platform that holds the heating element along with the support legs will be defined by the first layer. As the film becomes thicker the inherent stress in the film due to lattice mismatch or difference in coefficient of thermal expansion with the substrate will cause greater stress across the device. The 100nm thickness was chosen based on two factors. The first being that a thicker film will have a greater stress and thermal conductance. Too much stress across the device can lead to the device being destroyed. The greater amount of stress will lead to device failure which usually occurs in the support legs of the microheater. The second is that the film needs to have enough thickness so that it will withstand testing. Thicknesses below 100nm tended to be too fragile and would frequently fail during testing and operation. Choice of structural material is also of importance in regard to stress. The choice of thickness and material were the two most important variables in fabricating robust high temperature microheaters. The deposition technique can also have an effect on the amount of stress. ALD is the only thin film deposition technique used for the structural layer due to its good reproducibility at depositing high quality films. The heating element which consists of 5nm of titanium and 50nm of platinum is deposited using DC magnetron sputtering and patterned using a lift-off process. The 5nm of titanium is to promotes adhesion of the heating element to the $Al_2O_3$ film. The contact pads were the next layer and they consisted of 10nm of titanium and 200nm of gold which was also patterned using a lift-off process. The 200nm thickness of gold based off of the minimum thickness of gold required for wire bonding. A 20nm encapsulation layer of ALD $Al_2O_3$ was then deposited to protect the devices from further processing and from the environment during testing. The support legs and platform were patterned using a reactive ion etch(RIE) consisting of a $BCl_3$ plasma which etched through the 120nm of $Al_2O_3$. The vias which allowed for contact to the gold pads were defined using a similar RIE process to etch through the 20nm

encapsulation layer. The Bosch process was used to release the microheaters by doing a etch through the wafer from the backside. Figure 4.1 shows a summary of the fabrication process. A more detailed description of the process can be found in appendix A.

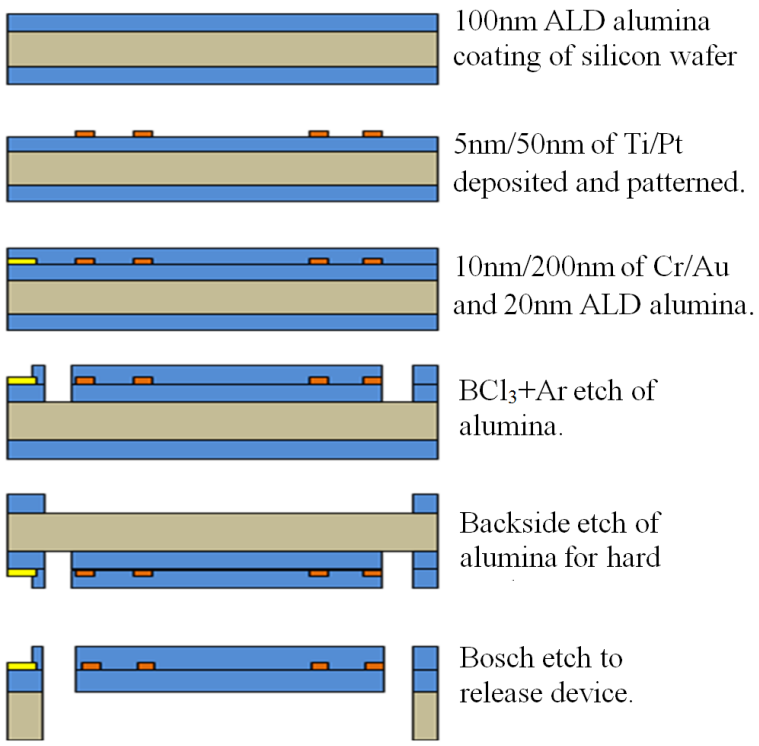


Figure 4.1: Summary of fabrication process for microheaters with a platinum heating element on a $Al_2O_3$ structure. More detailed description in appendix A.

The first choice of structural material and heating element were $HfO_2$ and tungsten respectively. The reason for these choices were that $HfO_2$ is capable of surviving a KOH release and has a low thermal conductivity while tungsten has an extremely high melting point. The hope was the release process would be a simple KOH dunk and the operating temperatures of the device could be very high. The problem that arose from the choice of these materials were that they were both very high stress materials. The devices were far too fragile to survive a KOH release and had extremely low yields much lower than 1%. The movement of liquid in the KOH bath was thought to be the cause of the devices breaking during the release. The Bosch process was later used to

release these devices. The yields were still very low at about 50% but it was enough to do testing of the devices. The next attempt at fabricating the microheaters was to use platinum on a hafnia thin film. These devices had slightly better yield upon release but still have very low operating temperatures similar to those of the tungsten on hafnia. Eventually the microheater fabrication process with the platinum on alumina was decided upon because it allowed for robust microheaters that had high yields upon release and also were able to reach temperatures in excess of 1000°C. The only drawback to using alumina and the reason why it was not the first choice was because it has a higher thermal conductivity than hafnia so the operating powers would by higher and it was thought that higher temperatures would be possible with the better thermal isolation of having a lower thermal conductivity.

During the electrical characterization of the 300x300µm devices maximum temperature the devices would begin to fail at 400°C and none would survive above 500°C. The larger 500x500µm heaters would begin to fail at even lower temperatures usually between 300°C and 400°C. Figure 4.2 depicts what can happen to the devices upon failure. Often times the failure would occur in the support legs of the microheater. The entire device would typically leave nothing to take a picture of then. Other times during testing cracks would appear across the platform as seen in Figure 4.2. Platinum was considered as a replacement for the tungsten as the heating element. It has less stress and a well known linear temperature coefficient of resistance (TCR) over a wide range of temperatures. The results for this were slightly better than the tungsten. The devices would still not survive a KOH release but proved to have a slightly higher release yield after the Bosch release method. During testing of the platinum on $HfO_2$ heaters the maximum operating temperatures would not go much higher than the previous tungsten microheaters they would reach a maximum of about 550°C before failing. After attempting various thicknesses for $HfO_2$ and still having no success it was abandoned and $Al_2O_3$ was chosen as a possible structural material. $Al_2O_3$ was not the first choice because of the thin films available, it had a higher thermal conductivity than $HfO_2$ and would not be able to survive a KOH release. Its greatest advantage over $HfO_2$ was that it had significantly less thin film stress when deposited onto the standard silicon wafers at about 350MPa compared to 1GPa for hafnia. The optimal thickness of 100nm for each film was determined by depositing films with thicknesses ranging from 50 to

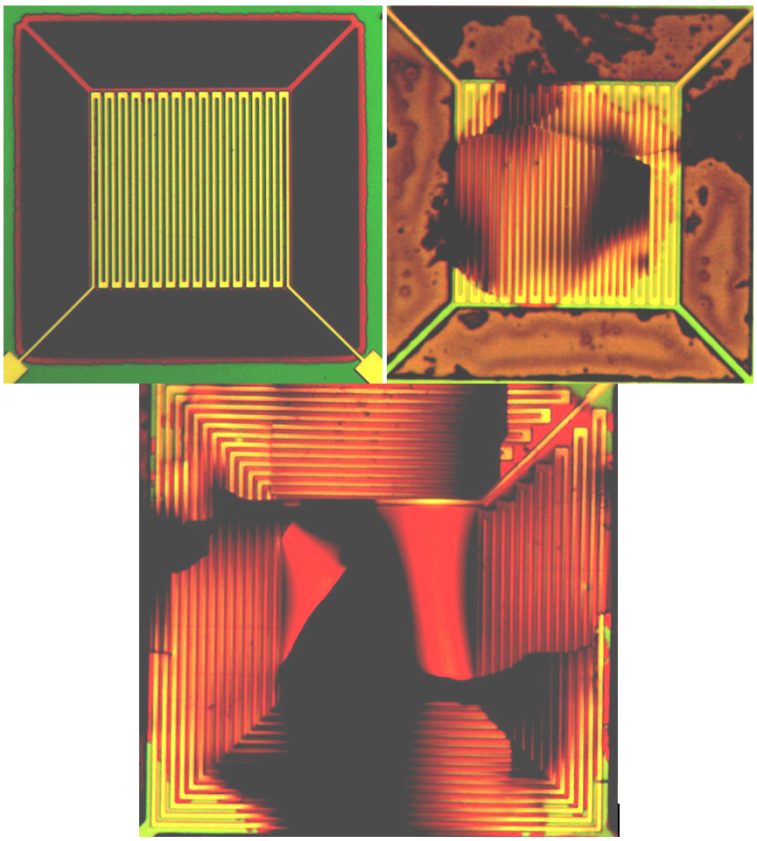

Figure 4.2: The upper left image is of a hafnia and tungsten microheater after surviving a release using the Bosch process. The upper right image shows an example of how the device would fail during high temperature testing. The bottom image shows how one of the larger 500x500µm devices failed during high temperature testing.

200nm. From this point on only $Al_2O_3$ will be discussed because $HfO_2$ had such poor yields after release and such low operating temperatures regardless of the thickness of the film.

$$G_L = 4k_{Al_2O_3}\frac{A_{Al_2O_3}}{L} + 2k_{Pt}\frac{A_{Pt}}{L} \tag{4.1}$$

At 50nm the yields after release of the $Al_2O_3$ microheaters was less than 25% for 100-200nm it was above 90%. During testing the 100nm thick structural layer was able to most consistently reach higher temperatures and survive successive heating and cooling cycles. So simply by trial and error and due to limitations in time the 100nm thick $Al_2O_3$

was found to be the optimal thickness for the microheaters. The next thing to consider was the thickness of the metal for the heating element. Tungsten was never tested on the $Al_2O_3$ due to its inherent high stress and poor performance on $HfO_2$ microheaters. Platinum was used as the heating element because of the before mentioned reasons of having less stress than tungsten and having a well known linear TCR over a wide range of temperatures. Determining a minimum thickness of platinum was favorable in order to reduce the thermal conductance to the substrate via the support legs. Equation (4.1) is the total thermal conductance for the four legs two of which have platinum on them where A is the cross-sectional area, L is the length of the legs, and k is the thermal conductivity of the material. The first term is the thermal conductance of the legs due to the alumina support, and the second part is the thermal conductance due to the platinum lead. The thermal conductivity of platinum 35W/m*K [70] is greater than that of alumina 2.59W/m*K [71] by over an order of magnitude. It may be expected then that the second term would greatly dominate the first term, but an appropriate thickness of the platinum could be chosen to balance this out so they have similar magnitudes. If the alumina support leg is 10µm and 100nm thick and the platinum leads are 5µm wide and 50nm thick this leads to a ratio of conductance for platinum to that of alumina of 1.7. This ratio could be lowered more by making the platinum thinner, but for ease of fabrication and to avoid possible grain boundary effects 50nm was chosen. The choice of a 20nm thick encapsulation layer of $Al_2O_3$ was determined by the minimum thickness necessary to protect the heating element from subsequent process steps and the environment during testing [72]. A picture of a released microheater is shown in Figure 4.3. What is evident from the SEM in Figure 4.3 is that the microheater is flat. This is due to the alumina having a tensile stress which is useful in this particular application.

## 4.3 Simulation and Design of Two Methods for Reducing Thermal Emission from Microheaters

Thermoluminescent materials were used to test the reduction in thermal emission. As mentioned in previous chapters thermoluminescence is seldom measured at temperatures in excess of 400°C. Typically thermoluminescent measurements are not taken above this

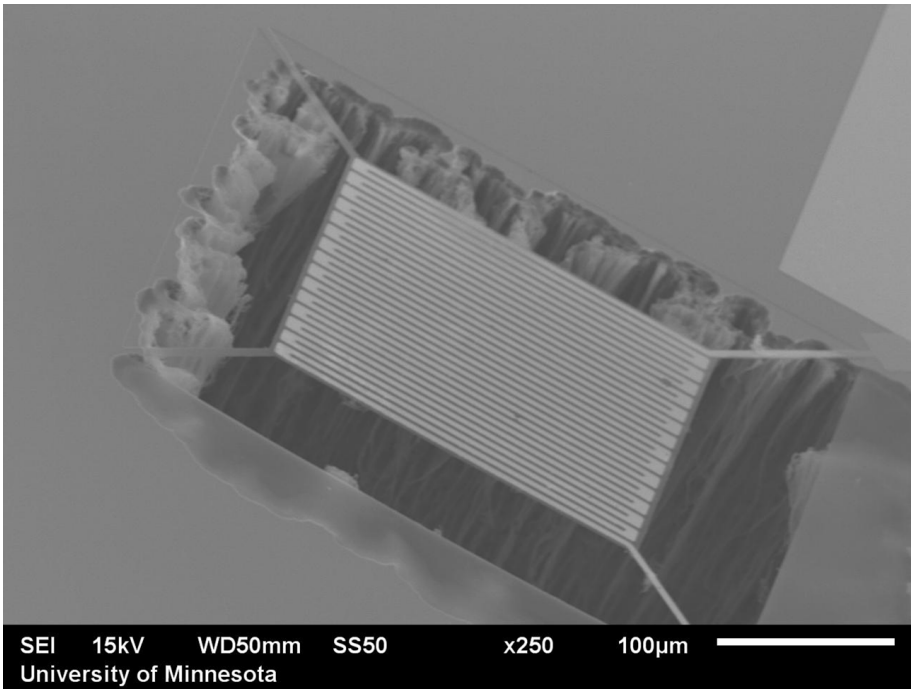


Figure 4.3: SEM of released microheater.

temperature because the thermal emission from the heating element will overwhelm the thermoluminescent signal. At 400°C the peak wavelength of the blackbody is around 4µm and will not interfere with most detection devices used to measure the visible spectrum of light. The part of the blackbody curve that is comprised of lower wavelengths is much lower in intensity but is still able to interfere with measurements of the already low intensity emissions that are typical with thermoluminescence. Figure 4.4 shows an example of how the thermal emission background signal can alter a thermoluminescent measurement. Optical filters can be used to block out the longer wavelength thermal emission but that could also block emission from the thermoluminescent sample.

The two alternatives presented here are able to reduce the thermal emission but still able to measure the emission wavelength from the thermoluminescent sample. Two thermoluminescent materials were chosen that have spectral emission characteristics appropriate for the corresponding reduced thermal emission techniques in order to test how these two methods reduce the thermal emission during a measurement. LiF:Ti,Mg is a material that was used in the characterization of transparent microheaters using an

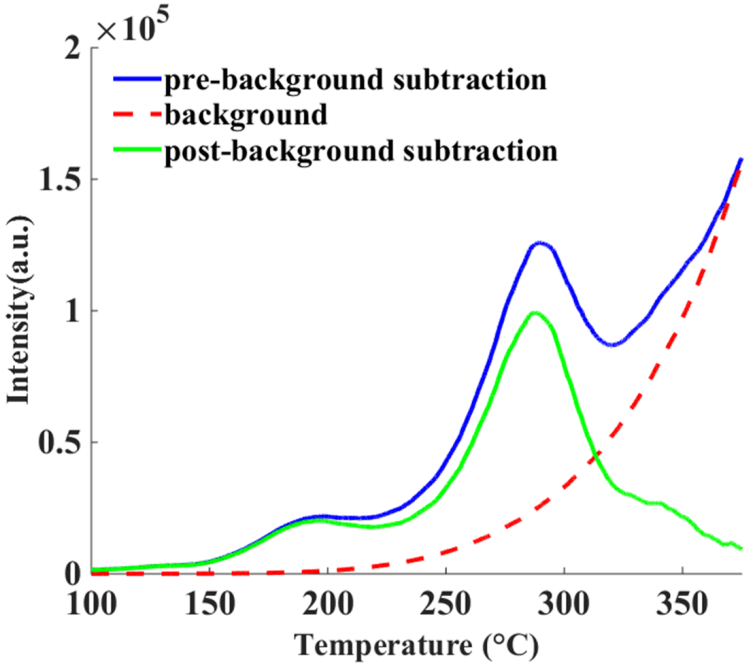


Figure 4.4: Example of how thermal emission background can alter the shape and intensity of a thermoluminescent signal. In this example the thermal emission curve is numerically subtracted from a measured glow curve for $CaSO_4$:Ce,Tb.

aperture. LiF:Ti,Mg has a wide emission spectrum which works well with the transparent microheaters because the aperture allows all wavelengths of emission to be measured while reducing thermal emission from the metal heating element. The TL material used for the microheaters with the multilayer interference structure was $CaSO_4$:Ce,Tb. The $CaSO_4$:Ce,Tb has sharp spectral emission peaks over a wavelength range where the multilayer structure can be designed to have lowered thermal emission. The spectral peak at 486nm was chosen to for the design of the multilayer since it is the strongest emission peak.

The multilayer design was based on a distributed Bragg reflector(DBR). The DBR coating was designed for the wavelength $\lambda$ and consisted of alternating layers with thickness $\lambda/4n$ for each layer and had a different index of refraction n for each layer. The wavelength $\lambda$ was chosen based on maximizing the reflectance in the center of the TL emission spectra for $CaSO_4$:Ce,Tb.

The DBR reflectivity is strongly dependent on the difference between the index of

refraction for each of the quarter-wave thick layers and the number of quarter-wave layer pairs. It would be ideal to increase the number of quarter-wave pairs to get a higher reflectivity. But due to stress and processing limitations two pairs was a good compromise between ease of fabrication and reflectivity. The two materials used in the DBR were $Al_2O_3$ and $TiO_2$ which have refractive indices of 1.78 and 2.62 at 490nm respectively. The indices of refraction for the individual thin films of $Al_2O_3$ and $TiO_2$ were measured using a spectroscopic ellipsometer. The spectroscopic ellipsometer measurement was done for wavelengths between 260nm to 900nm. The $TiO_2$ showed non-zero values for the imaginary part of its index of refraction ranging in values from $1x10^{-3}$ to $1x10^{-2}$. The peak of the DBR reflectivity was chosen to have its center at 490nm which corresponds to thicknesses for the $Al_2O_3$ and $TiO_2$ layers of 68.6nm and 46.7nm respectively. The $Al_2O_3$ and $TiO_2$ were deposited by ALD onto released microheaters. The microheaters were conformally coated on the top and bottom by the ALD. The fact that the coating was on the top and the bottom of the

| DBR material | Thickness (nm) |
|---|---|
| $TiO_2$ | 46.7 |
| $Al_2O_3$ | 68.6 |
| $TiO_2$ | 46.7 |
| $Al_2O_3$ | 68.6 |
| platinum | 50 |
| $Al_2O_3$ | 149 |
| $TiO_2$ | 46.7 |
| $Al_2O_3$ | 68.6 |
| $TiO_2$ | 46.7 |

Table 4.1: The final multilayer structure with DBR layers above and below the platinum. Asymmetry just above and below the platinum is due to the structural and encapsulation layers of the original microheater. Because of this the first layer deposited by the ALD is 20nm thinner to compensate for the 20nm of $Al_2O_3$ already deposited for encapsulation.

microheater lead to stress cancellation. If for instance the ALD coated just one side then the stress from the film could build up on that side leading to the device becoming

warped and eventual failure. There was already 20nm of $Al_2O_3$ due to the encapsulation layer so the first layer of $Al_2O_3$ deposited for the DBR was a reduced thickness of 48.6nm. The microheater platform was 100nm thick so the bottom layer was 80nm thicker than a simple DBR. Table 4.1 depicts the layer structure in the final device. The transfer-matrix method [73] was used to simulate the absorption of the multilayer microheater structure with values for the indices of refraction taken from the spectroscopic ellipsometer measurement. According to Kirchoffs law of thermal radiation, the emissivity of a body is equal to its absorptivity. Since the absorptivity of the film is known from the simulation, then the emissivity is also known. The plot of emissivity for the multilayer structure is shown in Figure 4.5. along with the emission spectra of $CaSO_4$:Ce,Tb. According to the simulation the emissivity of the multilayer is reduced from 0.47 to 0.08 roughly between 450-600nm, but the simulation does not take into account the periodic structure of the serpentine pattern and assumes a uniform platinum layer.

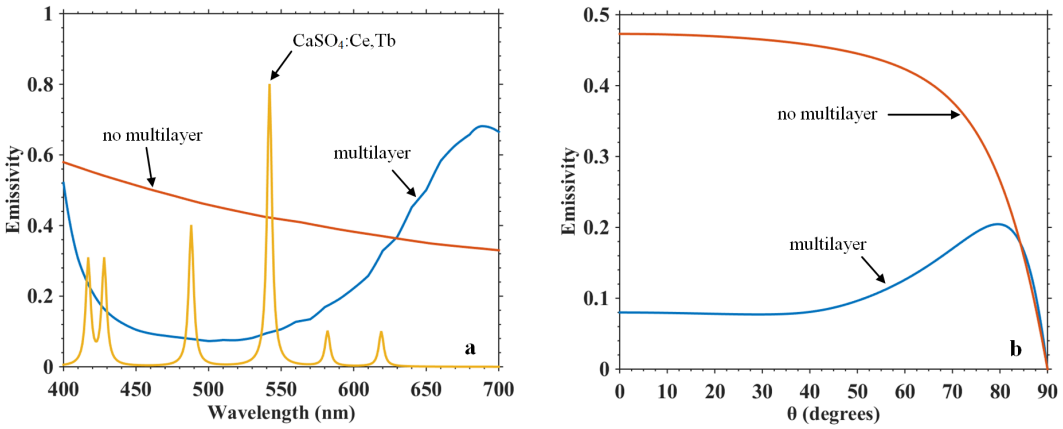


Figure 4.5: Simulation of emissivity for a microheater with and without a multilayer. a. The approximate emission spectra from a platinum surface (no multilayer), a dielectric coated platinum surface as described in Table 1 (multilayer), and a reference spectrum of $CaSO_4$:Ce,Tb. The main peaks of the calcium sulfate overlap well with the region of reduced emissivity at an angle of 0 degrees. b. The emissivity of the multilayer structure with the platinum surface at different angles from the microheater at a wavelength of 490nm.

In the metallized regions, the model shows that the coatings reduce the thermal emission intensity by a factor of about 6 compared to a uniform platinum layer, but the

overall emissivity is much lower because this model ignores the non-emitting open areas and any diffractive or potential plasmonic effects. The DBR center wavelength of 490nm was chosen because the simulation showed that it would decrease the emissivity of the microheater over a span of wavelengths which contains the strongest emission peaks of the $CaSO_4$:Ce,Tb. Figure 4.5 shows how the emissivity changes with different angles for the multilayer with platinum. The multilayer causes a slight increase in emissivity at higher angles.

## 4.4 Infrared Transparent Microheater with Aperture

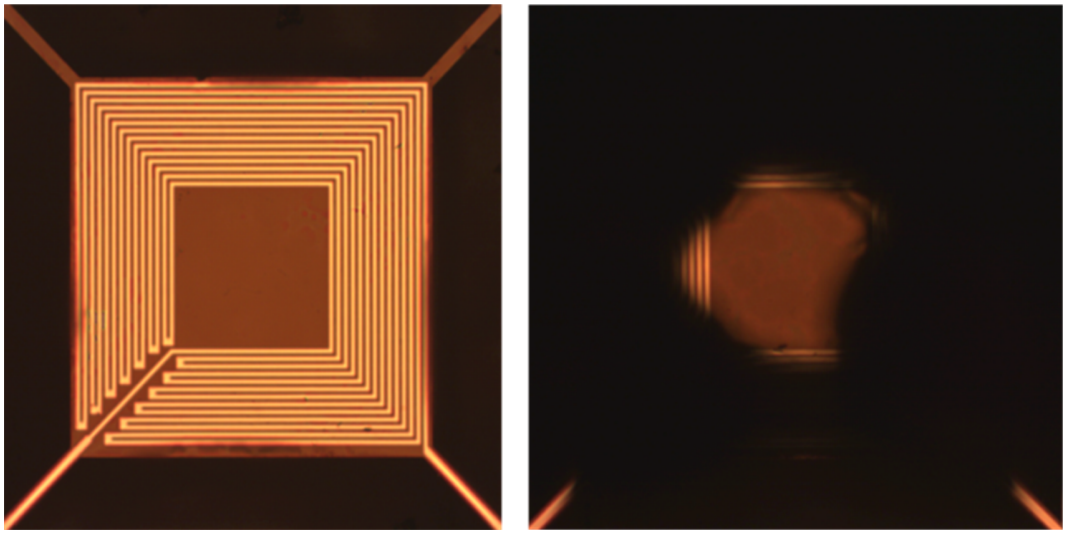

Figure 4.6: Typical transparent microheater without aperture (left) with aperture (right). The central region is infrared-transparent. The overall microheater is 500 x 500µm in area and the center square is 210 x 210µm. The area of the aperture is approximately $4.7x10^4 µm^2$ and the total area of the microheater is $2.5x10^5 µm^2$. The TCR of $2.3x10^{-3}$/°C was measured by placing the microheater on a thermoelectric cooler/heater to control the temperature and then measuring the resistance in the temperature range of 15-60°C. Current was applied to the microheater to raise its temperature from 50-400°C where the temperature was measured using a thermal camera.

A typical transparent microheater is shown in Figure 4.6. The overall device is 500 x 500µm in area and the central region which is transparent is 210 x 210µm. The total area of the microheater is $2.5x10^5 µm^2$ as seen on the image in left side of Figure

4.6 and the area of the aperture on the right side of Figure 4.6 that overlaps with the microheater is approximately $4.7x10^4 \mu m^2$. The aperture overlaps about 19% of the total microheater area. The thermal emission from the microheaters was tested by gradually raising the temperature by applying increasing current from a source measurement unit(SMU) to the microheater. A microbolometer thermal camera with an areal density of 676 image pixels per microheater was then used to measure the surface temperature of the microheater. The thermal camera measurement was calibrated by using the microheater metal as a thermistor to verify accuracy. The microheater was placed on a thermoelectric cooler/heater to control the temperature, and the resistance was measured in the temperature range of 15-60°C. The resistance versus temperature measurement was then repeated by running current directly through the heating element of the microheater and measuring temperature using a thermal camera to measure temperature in a range of 50-400°C.

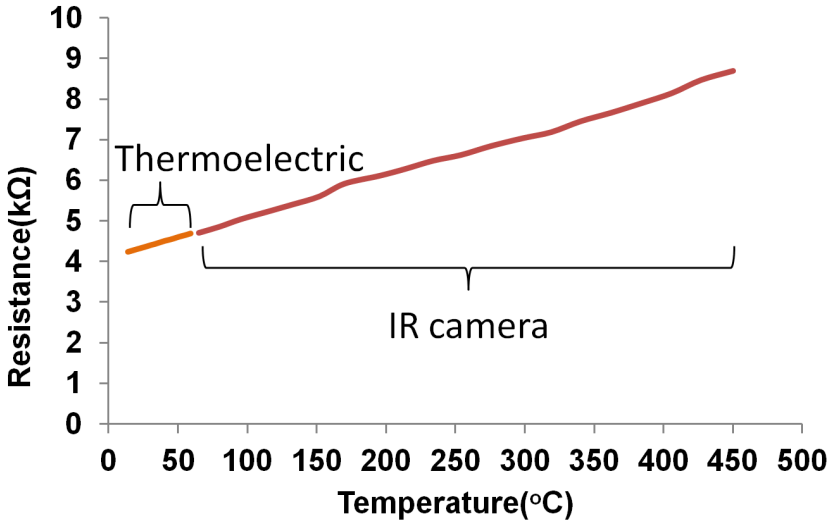


Figure 4.7: Thermoelectric measurement with a well known temperature used to configure the higher temperature measurement of the thermal camera.

The result of the two measurements is shown in Figure 4.7. The resistances measured during this process were calibrated so that measurements done with the thermoelectric and thermal camera corresponded in their overlap range. The thermal camera has a temperature uncertainty of 2%. The TCR measured with the thermoelectric

heating and the microheater heating was $2.3x10^{-3}/^{o}C$. There was a significant temperature gradient across the microheater from the lower temperature center to the higher temperature coil, but it was accounted for by using our thermal camera on identical dummy microheaters with an absorbing region of Ti/Pt in the center. The Ti/Pt in the center was deposited and patterned along with the main heating element but was not electrically connected to the heating coils; however, the emissivity of the Ti/Pt in the center was the same as the Ti/Pt that was being heated electrically. A comparison of the temperature between the heating element and center was performed with the thermal camera which was calibrated to measure the temperature of the heating element. Therefore in Figure 4.7, when a temperature is indicated on the x-axis, that temperature was absolute within the limits of the measurement error. A higher current drive was used when the aperture was placed over the center of the microheater to offset the temperature gradient across the microheater. Data was then taken when the aperture was positioned over the heater coil.

Figure 4.8 shows a comparison of thermal emission versus temperature in three cases; without aperture, with aperture placed in the center transparent area of the microheater, and with the aperture offset and placed over the platinum heater coil. Note that the thermal emission measured through the aperture is reduced by 90% when it is moved from the heater coil to the transparent center. The reason a comparison was done between the aperture over the heating coil and no aperture is because one could speculate that the reduction in thermal emission intensity is simply due to the aperture blocking all light from getting to the detector. Since there is still significant reduction in intensity between the aperture over the heating coil and no aperture methods, it proves that the reduction in thermal emission for the aperture centered case is because most of the light from the heating coils is getting blocked and only emission from the center will be allowed directly through the aperture to the detector. The aperture used in this measurement was custom made using a thin piece of stainless steel with a hole burned into it using a high power Nd:YAG laser. Most commercially available apertures are in the center of a metal disk. For this application that arrangement would not work because when the aperture was placed over the center of the microheater the metal disk portion would be blocking the electrical contacts. In order to compensate for this the high power laser burnt the aperture into the edge of a piece of metal. The aperture

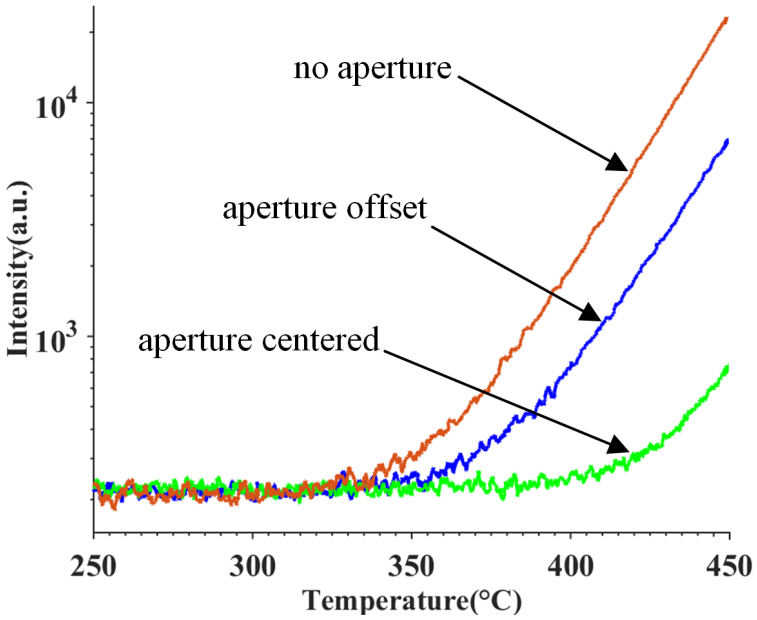


Figure 4.8: Comparison of a thermal emission signal from a microheater with no aperture, an aperture offset so it is centered on the heating element, and with aperture centered to the middle of the microheater. The thermal emission was reduced by 97% when with the aperture was placed at the center of the microheater. A reduction in thermal emission intensity of about 90% at 450°C occured when the aperture was placed over the heating element compared to when there was no aperture.

would have to be within 600 µm of the edge to not block the metal contacts.

LiF:Ti,Mg (TLD-100), as discussed previously, is a thermoluminescent (TL) material that was used as a characteristic low photon number emitter in the characterization of the transparent microheaters. LiF:Ti,Mg particles of 10-20µm in size were deposited on the microheater surface. The deposition of microparticles was carried out by first placing the microparticles into isopropyl alcohol (IPA). This microparticle and IPA mixture was placed in a liquid dropper and one drop was placed on the microheater. The IPA would quickly evaporate leaving only the microparticles remaining on the microheater. Measurements were done beforehand to determine that the IPA has no effect on the thermoluminescence of the LiF:Ti,Mg. The TL intensity versus temperature of the LiF:Ti,Mg particles is shown in Figure 4.9. The aperture was placed over the center of the microheater so that the thermoluminescence of the LiF:Ti,Mg was detected while

the thermal emission from the heating element was blocked. At high

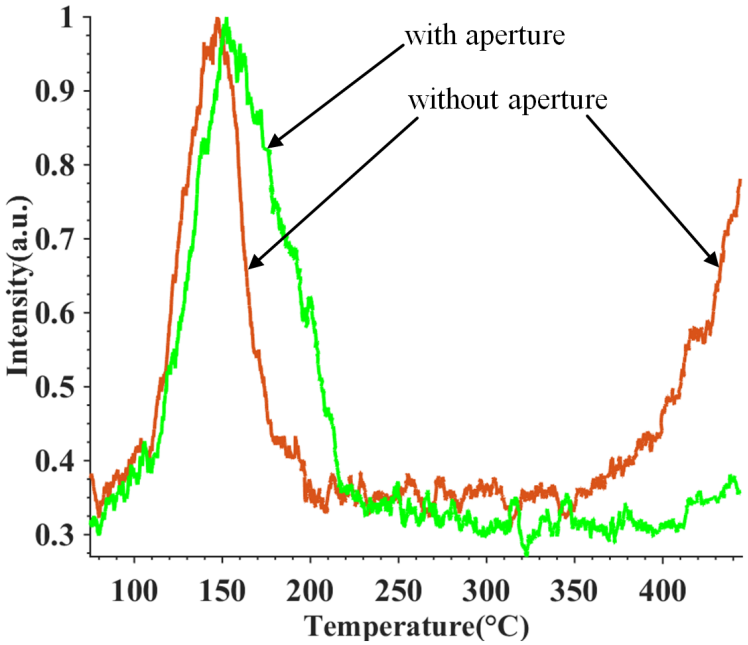


Figure 4.9: Normalized LiF:Ti,Mg(TLD-100) TL glow curves of 10-20µm diameter particles on the microheaters. The red curve shows emission from a microheater without an aperture while the green curve shows the emission of a transparent microheater using the aperture. A higher density of particles was placed on the microheater with the aperture to normalize the intensity of the TL emission.

temperatures the intensity of the thermal emission of the microheater without the aperture becomes comparable to the intensity of the LiF:Ti,Mg TL peak around 150°C. For higher temperature TL measurements this thermal emission can obscure or overwhelm the signal making it impossible to take accurate measurements. But when the aperture is placed over the center of the microheater most of the thermal emission is blocked allowing for the possibility of measuring higher temperature TL peaks. All optical measurements were taken in a dark chamber using a photomultiplier tube (PMT) because of the weak intensity of the luminescent or thermal emission signals. The emission spectra for the LiF:Ti,Mg is 320-620nm [74]. It consists of a single peak spanning the entirety of this range. It is a good fit for testing with the aperture because it lets light of all wavelengths from the center of the microheater reach the PMT.

## 4.5 Microheater with Emissivity Modified by Multilayer

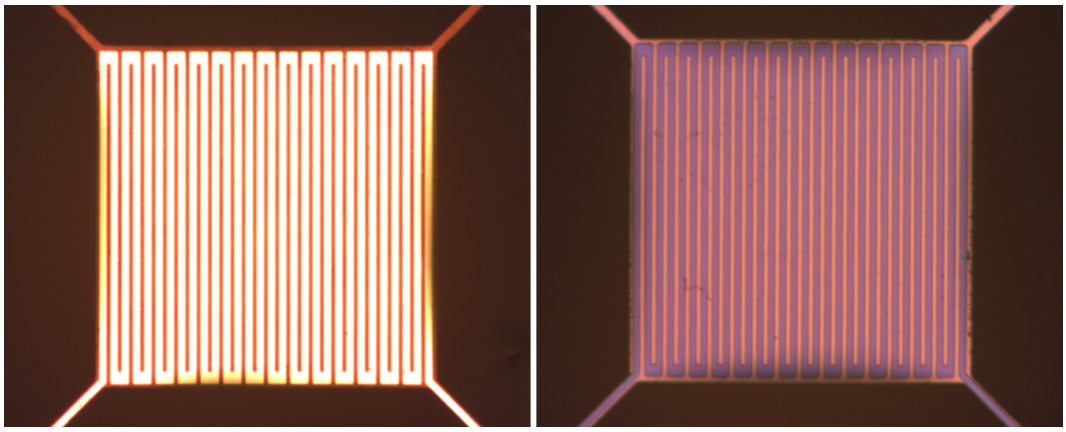

Figure 4.10: Microheater without thermal emission reduction multilayer(left) and microheater with the multilayer (right). Both are 300µmx300µm platforms. The change in color is attributed to the change in reflectivity introduced by the multilayer. The TCRs before and after the multilayer deposition were 2.3x10$^{-3}$/°C and -4.4x10$^{-4}$/°C respectively.

The microheaters used in the multilayer method are shown with and without the multilayer in Figure 4.10. These microheaters have 300µm x 300µm dimensions. The temperature dependence of the microheaters platinum resistors was measured before and after multilayer deposition to give TCRs of 2.3x10$^{-3}$/°C and -4.4x10$^{-4}$/°C respectively. The transition from positive to negative was due to the impact of $TiO_2$ on the resistance. It is inferred from our measurements that the $TiO_2$ is somewhat electrically conductive, and it behaves in the same manner as semiconductors, which tend to have negative TCRs. The TCR measurements were used to determine what the drive voltages were for the microheaters. This was done by finding the correlation between voltage and temperature by increasing the voltage applied to the microheater and then measuring the current to determine the resistance. The resistance along with the TCR was used to determine the temperature of the microheater. A linear increase in voltage corresponds to a linear increase in temperature. This is the same as the process used for the infrared transparent microheaters. The microheaters were placed in a dark chamber during optical measurements to reduce ambient light. The voltage source and resistance measurement were both done using a SMU to perform a linear ramp

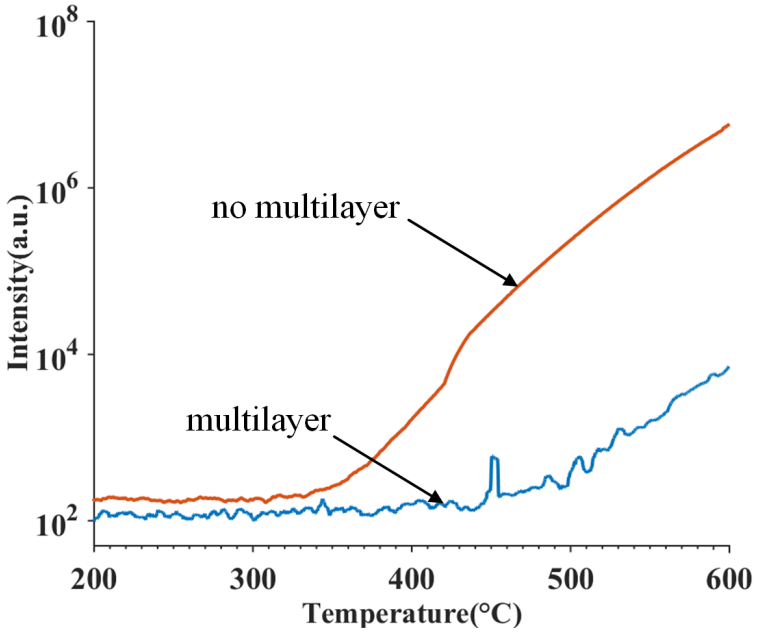


Figure 4.11: Thermal emission form microheaters with and without multilayer. The thermal emission intensity at 600°C was a factor of about 800 less for the microheater with the multilayer.

in temperature, which is standard in TL analysis. A photomultiplier tube (PMT) was used to measure the light emissions from the multilayer structure and $CaSO_4$:Ce,Tb. The counts were read by the frequency counter which sent the data to a computer. The computer also received the resistance measurements from the SMU. The thermal emission intensity of the microheater with and without the multilayer was measured up to 600°C as shown in Figure 4.11. The multilayer reduced the thermal emission intensity by almost three orders of magnitude. In order to demonstrate the ability of the microheaters to block background radiation, microparticles of $CaSO_4$:Ce,Tb were deposited on a microheater. A few microparticles of $CaSO_4$:Ce,Tb would normally be very difficult to see in a standard heating system because of the heater thermal emission. Figure 4.12 shows a SEM image of particles of $CaSO_4$:Ce,Tb on our microheater with particle size <80m. Figure 13 demonstrates the reduction in thermal emission intensity while measuring the

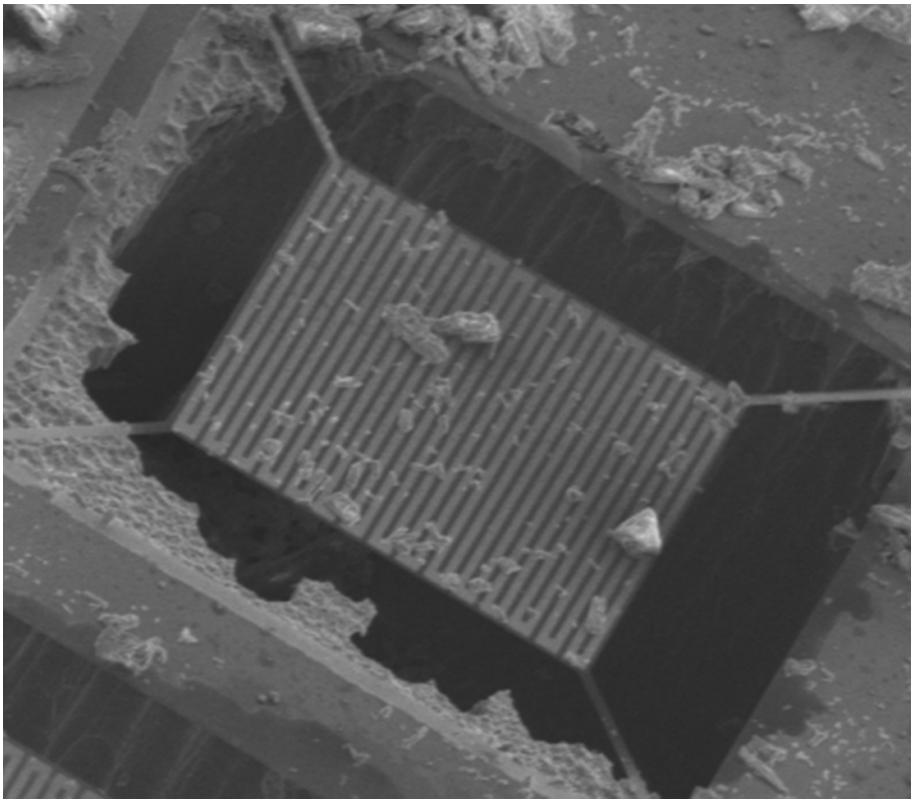

Figure 4.12: image of microheater with $CaSO_4$:Ce,Tb microparticles.

luminescence of the $CaSO_4$:Ce,Tb microparticles. The PMT used for the optical measurements was only sensitive to wavelengths between 350 to 650nm. The thermal emission signal measured depended on a combination of the quantum efficiency of the PMT and the emissivity of the microheater with the multilayer. From Figure 13 the PMT count at 420°C was 2474 photons from the particles and 153 photons from the thermal emission signal. The thermal emission signal for the microheater without the multilayer had a PMT count of 4386 which would have had a detrimental effect on the measurement. The efficiency of the interference structure increases even further at higher temperatures as the thermal emission power moves further towards shorter wavelengths.

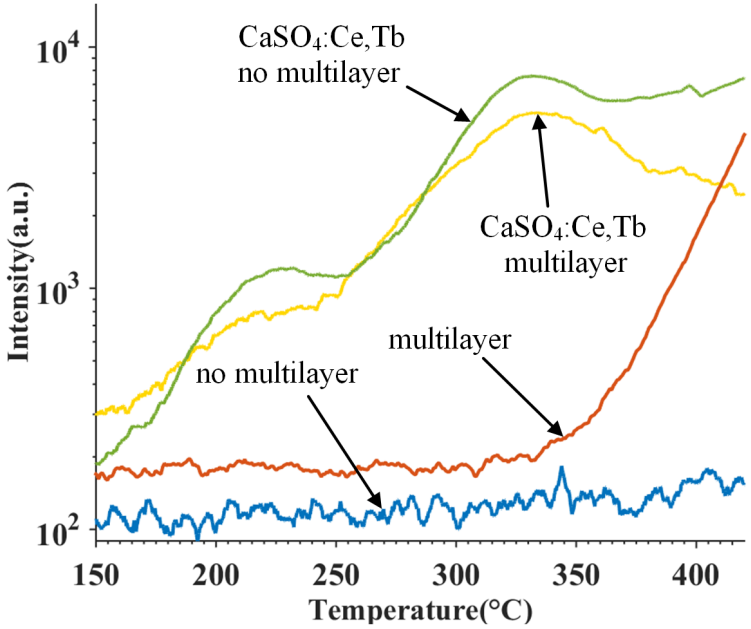


Figure 4.13: Thermoluminescence of $CaSO_4$:Ce,Tb microparticles on a microheater with interference structure. The thermal emission from the microheater with no multilayer measured by the PMT is 4386 counts and the TL intensity was 2474 counts at 420°C. The effect of the thermal emission can been seen when comparing the $CaSO_4$:Ce,Tb signal with and without the multilayer. The intensity values from about 350°C and above are compromised by the background, so all points from 350°C and up are made accessible to measurement by the multilayer.

## 4.6 Comparison of Reduced Thermal Emission Techniques

It would be useful to discuss the relative advantages and disadvantages of the two methods used to reduce thermal emission during high temperature fluorescence measurements. Transparent heaters have low emissivity across extremely wide swaths of the infrared and visible spectrum. Their ultimate performance is limited by the intrinsic absorption of their constituent dielectric, but even this will be small in almost all cases because the transparent region can be made extremely thin. As one example, if a 10nm layer were deposited by atomic layer deposition, the material would require an incredibly high effective absorption coefficient of about 4.6 million/cm to have an emissivity of even 1%. On the other hand, the central region is only a fraction of the overall area of the heater, so an aperture must be used to reject emission from the heater coils. This

leads to an additional complication of non-uniform heating in the heater. The temperature of the coils will typically be hotter than the temperature of the transparent region; therefore, a calibration of the temperature of the central region relative to the coils must be performed at all temperature regions of interest using an external device such as a thermal camera or by calibrating relative to known temperature events such as characteristic thermoluminescent peaks of known materials. An advantage of the transparent microheater method is relative ease of fabrication, since the transparent regions can be created in a standard microheater process with no additional process steps.

The most fundamental disadvantage of the interference method is that interference structures must be optimized for specific wavelength ranges. These need not be continuous, but they are generally fixed by the fabrication process. Arbitrary tunability is extremely difficult for interference structures except for certain special cases such as Fabry-Perot resonances. In addition, the fabrication process is more difficult because incorporating interference structures is fabrication intensive. This applies whether the interference structure is a multilayer as in this work or a more advanced structure such as a photonic crystal. Advantages of the multilayer include the ability to use the entire heater without having to block emission from certain regions. The resulting optical collection system is then far simpler, and the amount of light that can be collected is significantly increased. While off-axis spectral performance can play a role, most collection optics use angular ranges that will shift interference performance a significant amount. In addition, as mentioned before, a photonic crystal could be used to block off light from any angle. If the spectral range of the weak emitter is limited, the efficiency of the interference structure in rejecting thermal emission over that range can be near 100%.

Two methods for reducing thermal emission from microheaters were introduced. The aperture method was shown to reduce the thermal emission up to 450°C by 90%. It blocks all emission wavelengths detectable by the PMT and does not require any further microfabrication steps; however, it requires the careful alignment of an aperture and has non-uniform heating across the heated surface. The multilayer interference method was capable of reducing the thermal emission signal by a factor of 800 and has uniform heating. The methods were tested by measuring the weak emission of thermoluminescence of LiF:Ti,Mg and $CaSO_4$:Ce,Tb microparticles at high temperatures.

# Chapter 5

# Thermoluminescent Microparticles for Temperature Sensing of Rapidly Increasing Thermal Events

## 5.1 Thermoluminescent Microparticles for Temperature Sensing

Common active methods for measuring the temperature profiles of explosive events have involved using some form of pyrometer or thermocouple [75–79]. Two drawbacks to these methods are obscuration of the thermal emission due to debris in the explosion and having to be kept a safe distance from an explosion to avoid being damaged, respectively. Applications where the sensor can be placed in direct contact with the explosive charge can have an advantage over these sensors. The use of thermoluminescent materials as passive temperatures which are placed very near or in direct contact with the explosive charge have been suggested in previous literature [80, 81], and have been shown to work as passive temperature sensors in explosions [82–84]. These methods used TL materials such as lithium borate ($LiB_4O_7$:Cu,Ag), magnesium borate ($MgB_4O_7$:Dy,Li), calcium sulfate ($CaSO_4$:Ce,Tb) and lithium fluoride (LiF:Mg,Ti) which were irradiated with

some form of ionizing radiation to fill the various traps in their band gaps. Each of these traps are characterized by the three main parameters of $n$, $E$, and $s$. The value of n stands for the filled trap density per unit volume. The trap depth, $E$, is the energy difference from the valence or conduction depending on if the trap contains a hole or electron. And the final parameter, $s$, is the frequency factor which has units of inverse time.

When the TL material is exposed to the high temperatures of the explosion, the value of n will decrease due to the thermal energy. When a sample has several traps, each one will lose carriers at a different rate depending on the thermal energy profile a.k.a. temperature profile of the explosion. After the testing, the thermoluminescence of the material is measured and compared to a control sample that was left out of the explosion. The temperature of the explosion was determined by comparing the thermoluminescence of the control sample to the sample that went through explosive testing.

In this previous work small amounts of TL microparticles were placed at a fixed distance from an explosive charge. The amount of microparticles used was a few grams at a time which would consist of thousands of microparticles. The shock wave from the detonation would cause the microparticles to be spread across the test chamber. Debris left over after testing was then collected. This debris would contain small amounts of the original TL material placed in the test chamber before the explosion. The amounts collected and then measured were usually only a few or maybe tens of milligrams of debris and TL microparticles which would mean they were made up of hundreds to thousands of microparticles. Even though these microparticles were placed in the same container they may have experienced different temperatures. Each microparticle does not necessarily experience the same temperature profile. Some may be shielded from the heat of the initial explosion by other particles or have possibly be blown away more quickly depending the flow of air in the explosion. The goal of this work is to look at a method of using microheaters for measuring the difference in temperature of various microparticles and show that the temperature that each microparticle is exposed to can differ over a large range. And that while the previous method does offer an accurate method of measuring temperature in an explosion further information on the temperature profile can be measured by looking at the individual microparticles.

## 5.2 Recovering Temperature Profile from Thermoluminescent Glow Curve

The thermoluminescent glow curve intensity, shape and position are dependent on the physical parameters of the traps in the band gap of the thermoluminescent material as described in chapter 2. The parameters for trap depth $E_t$ and frequency factor $s$ determine the peak position and shape where as the filled trap density n determines the intensity of the thermoluminescence. The intensity of the thermoluminescence will be linearly proportional to the number of filled traps assuming that each filled trap will empty and the carrier that was held in the trap is allowed to recombine to emit a photon as described in chapter 2. The temperature at which the filled trap empties is dependent on the depth of the trap and its frequency factor. The glow curves shown so far have a linear increase in temperature which eventually empties the majority of filled trap states. The maximum temperature of the linear ramp is chosen to empty the majority of the traps. In practice most glow curves are measured up to around 400°C to 500°C. This temperature range is usually sufficiently high enough to get a full read of all the trap states in a thermoluminescent material and empty the majority of trapped carriers. If the linear ramp stops at a lower temperature then some of the traps which have glow curve peaks at higher temperature will still have a significant filled trap population.

Another factor in emptying traps is the heating rate. As described in chapter 2, with rapid heating rates the glow curve peaks can shift to higher temperatures. Figure 6 in chapter 2 shows an example of how the glow curve peak will shift with heating rate. Even when the linear ramp reaches higher temperatures, such as 500°C, if the heating rate is sufficiently high then some of the higher temperature glow curve peaks will be pushed out to temperatures above 500°C. This means that the filled trap corresponding to the higher temperature glow curve peaks does not empty. What can happen in both the cases of lower maximum temperature and rapid heating rates for linear heating is that certain traps corresponding to the intermediate glow curve peak temperatures is lower amounts depopulation. These intermediate peaks are not at low enough temperatures to completely depopulate nor are they high enough temperature to have negligible depopulation. These traps will only partially depopulate. The concentration

$$n(t) = n_0 \exp\left[ - s \int_{t_0}^{t} \exp(-E_t/kT) dt \right] \tag{5.1}$$

of traps that are emptied in the intermediate case are a result of the maximum temperature that was reached and the heating rate. Partially depopulated traps then hold some kind of information about what the heating rate and maximum temperature they were exposed to. The temperature profile does not need to be limited to a simple ramp function. The linear heating is useful in simplifying the math for the derivation of the first-order kinetics equation. In the general case any temperature profile can be inserted into Equation (2.3) which is shown again here as Equation (5.1). The value of T in Equation (5.1) is now a function of time function of time T($\tau$). There are multiple solutions for n given any number of functional forms of T($\tau$). Some knowledge of the functional form of T($\tau$) will be assumed from here on to achieve unique solutions for $n$. It will further simplify matters if the amount of parameters used to describe T($\tau$) is minimized.

$$n = n_0 \exp[-t \exp(-E_t/kT)] \tag{5.2}$$

Thermal fading is an example of a single parameter case. When a sample is left at room temperature for long a period of time the traps will begin to depopulate. Some traps may depopulate in a matter of hours others may take decades. A sample has been irradiated and left a room temperature for some amount a time. The single parameter of this temperature profile would be the length of time the sample has been left at room temperature. Assuming that this sample is a single first-order peak material the amount of depopulation of the filled traps will empty according to Equation (2.15) repeated as Equation (5.2) here for convenience. The glow curve of this sample can be measured to determine the maximum intensity which correlates to the amount of filled traps. The same sample can then be reirradiated with the same dose it was before and the glow curve measured again without the thermal fading. Knowing the values of $E_t$ and $s$ of the sample a curve fit to the none thermally faded sample can be done. A simulation of the glow curve is carried out using the known values of $E_t$ and $s$. The value for $n_0$ is then adjusted until the simulated curve

$$I(T) = sn_0 exp[-st_{fade}\exp(-E_t/kT_{room})]\exp(E_t/kT)\exp\left[\frac{-s}{\beta}\int_{T_0}^{T}\exp(-E_t/k\theta)d\theta\right] \tag{5.3}$$

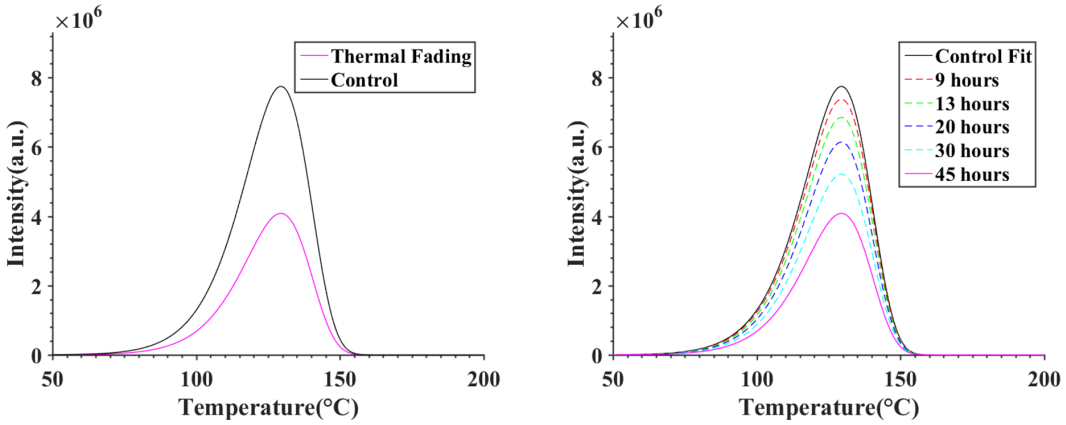


Figure 5.1: (Left) Example of a possible measurement of a single peak material with and without thermal fading. (Right) Example of how a simulation of the control can be used by increasing $t_{fade}$ of Equation (5.3) until it makes a good match to the measurement of the thermally faded sample.

matches the curve without thermal fading. This is the curve fit to the control sample. The control sample is the sample that has not experienced a temperature profile that will significantly change its glow curve after the initial irradiation. The initial filled trap density $n_0$ is known from the control sample curve fitting. This initial filled trap density can then be substituted into Equation (5.2) as $n_0$. Another glow curve fit will be done by substituting equation (5.2) for $n_0$ in the first-order kinetics equation the result is shown in Equation (5.3). The curve simulated using Equation (5.3) will be compared to the measurement of the sample that was thermally faded. The single parameter of $t_{fade}$ will be adjusted until a good fit to the thermally faded sample is found. This will be the amount of time between the glow curve measurement and the initial irradiation. Figure 5.1 illustrates this process of comparing simulated to measured glow curves in order to determine a parameter which in this case is $t_{fade}$. From the simulated results the time between irradiation and measurement for the thermally faded sample was 45 hours. In reality both of these curves are simulated but this was an

example of how the process of fitting the first-order kinetics to a measured glow curve can be used to find information about the temperature profile that a thermoluminescent sample experienced. The process of determining the temperature profile starts with knowing parameters $E_t$ and $s$ for all the traps and having some knowledge of what the temperature profile may look like. In this example it would have simply been a constant temperature with the parameter of time being the unknown. The guess for temperature profile T($\tau$) is substituted into Equation (5.1). The parameters for the temperature profile determine the amount of depopulation of the trap. The results of the depopulation from Equation (5.1) are substituted for $n_0$ in the first-order kinetics equation. The parameters of the temperature profile are then changed until a good fit to the sample that was exposed to the temperature profile is found.

## 5.3 Thermoluminescent Microparticles used to Measure Temperature in an Explosion

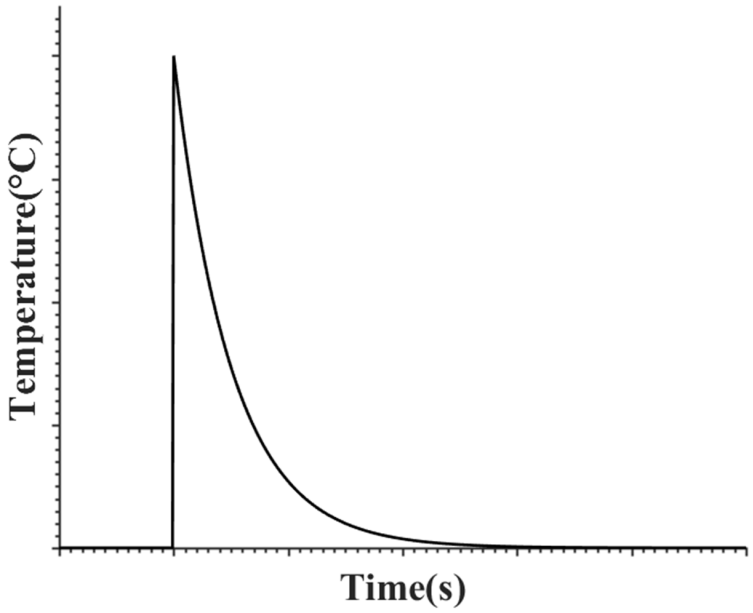


Figure 5.2: Model for the temperature profile of an explosive event.

$$T(t) = T_{max} \exp(-t/\tau) \tag{5.4}$$

$$n(t) = n_0 \exp\left[ - s \int_{t_0}^{t_1} \exp(-E/[kT_{max} \exp(-t/\tau)])dt \right] \tag{5.5}$$

In practice two samples of the same thermoluminescent material are irradiated with the same dose. This will lead to both samples having the same concentration of filled trap states and of course the same trap parameters $E_t$ and $s$. One of these samples is then exposed to some temperature profile T($\tau$). The temperature profile experienced by thermoluminescent microparticles in an explosive event can by modeled by an instantaneous jump to a maximum temperature and then an exponential cooling to room temperature[10]. Figure 5.2 depicts this temperature profile along with Equation (5.4)

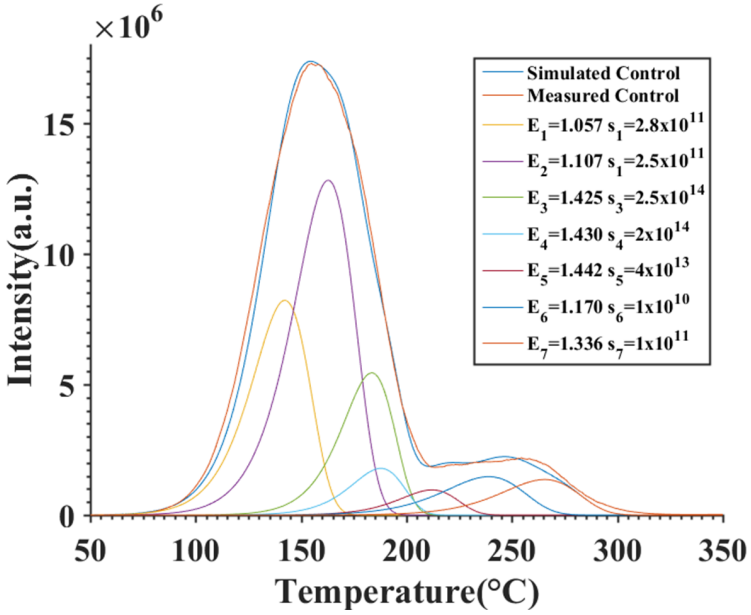


Figure 5.3: Glow curve fitting to control sample for $MgB_4O_7$:Dy,Li. The seperate first-order peaks are shown along with their corresponding parameters $E_t$ and $s$. The trap depths $E$ are in electron-volts and frequency factor $s$ in inverse seconds.

which can be used to describe it analytically. As with the single parameter example Equation (5.4) is substituted for the temperature T in Equation (5.1). The result of

| E (eV) | s(1/s) | $n_0(1/cm^3)$ |
|---|---|---|
| 1.057 | $2.8x10^{11}$ | $5x10^8$ |
| 1.107 | $2.5x10^{11}$ | $9.2x10^8$ |
| 1.425 | $2.5x10^{14}$ | $3x10^8$ |
| 1.430 | $2x10^{14}$ | $1x10^8$ |
| 1.442 | $4x10^{13}$ | $5.9x10^7$ |
| 1.170 | $1x10^{10}$ | $1.22x10^8$ |
| 1.336 | $1x10^{11}$ | $1.1x10^8$ |

Table 5.1: Trap parameters used to fit 7 first-order peaks to the control glow curve of $MgB_4O_7$:Dy,Li.

the substitution is shown in Equation (5.5). This will be the new carrier concentration that will be used to replace $n_0$ in the first-order kinetics equation. The $n_0$ in Equation (5.5) is the fill trap concentration prior to the explosive testing. The temperature profile described by Equation (5.4) has two parameters, the maximum temperature $T_{max}$ and time constant $\tau$. The two parameters for this temperature profile means that the single trap case given in the previous example is not sufficient to describe the temperature profile. There are multiple values of $T_{max}$ and $\tau$ that can lead to the same amount of depopulation of a trap. At least one more trap will be needed in order to find a unique description of the temperature profile. Additional traps will depopulate at different rates. Each trap will have multiple parameters of $T_{max}$ and $\tau$ that will describe the amount of depopulation. The intersections of solutions for $T_{max}$ and $\tau$ for these traps will be a more constrained solution reducing the range of solutions for $T_{max}$ and $\tau$. A robust method to find these parameters uses an initial fit to the control sample and varies the parameters until a good fit is made to the sample from the explosive testing. $MgB_4O_7$:Dy,Li is an oxide that was used in explosive testing with the fit for the control sample shown in Figure 5.3. The trap parameters of $E_t$, $s$ and $n_0$ were found by manually fitting 7 first-order glow curve peaks to the measured control sample. Table 5.1 shows all the values for the trap parameters used in the fit. The glow curve measurements taken of the magnesium borate were done in a similar fashion as the thermoluminescent measurements done in chapter 3. The measurements were carried out by linearly heating the sample at a rate of $0.6^oC/s$ and measuring the resulting glow curve with a PMT. The heating rate is slower due to the thermal mass

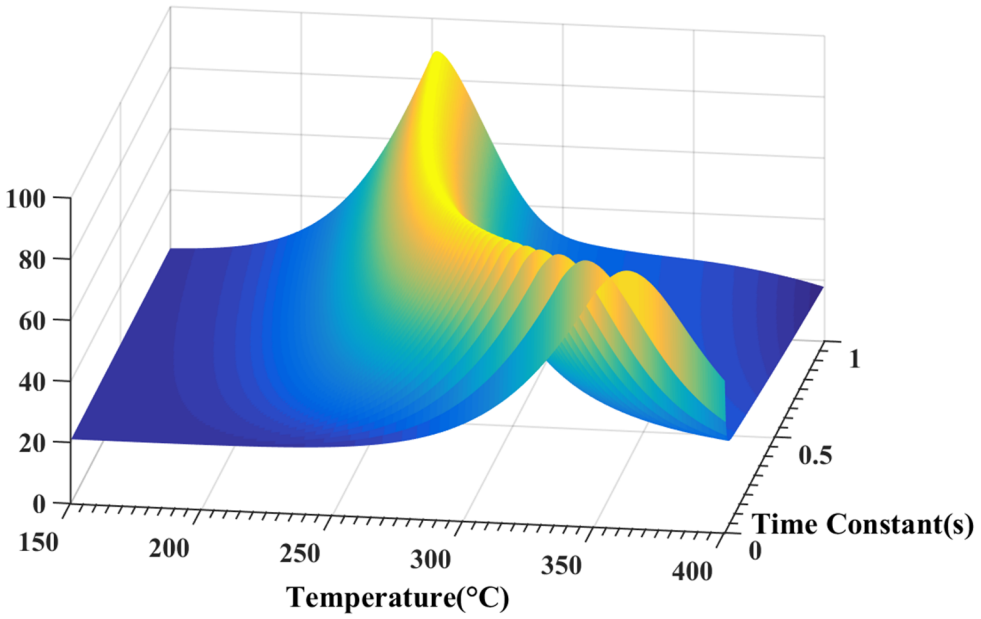


Figure 5.4: Grid of correspondence between simulated to measured data by taking the difference between each point at the corresponding temperature. The best match between the simulated and measured glow curves had the smallest average difference between points.

of a copper puck which is used to hold the powder sample. An optical bandbass filter centered at the 486nm emission wavelength of the magnesium borate was used to reduce the amount of measured thermal emission from the heating element. A range of temperature profile parameters for $T_{max}$ and $\tau$ is evenly sub divided. The subdivisions of these parameters forms a grid of values. Each grid location corresponds to a different set of $T_{max}$ and $\tau$ values. The set of values in each grid location is substituted into equation (5.4). This makes a new grid of values corresponding to different temperature profiles which can then be substituted into Equation (5.5) to calculate the new filled trap populations for each of the seven traps. Each grid location will correspond to a different set of partially depopulated traps which when summed result in another grid of simulated glow curves of the microparticles that were in the explosion. The solution at each grid location is compared to the measured sample from the explosive testing. The comparison is done by taking the difference between each point at the corresponding temperature. The best match between the simulated and measured glow curves had the

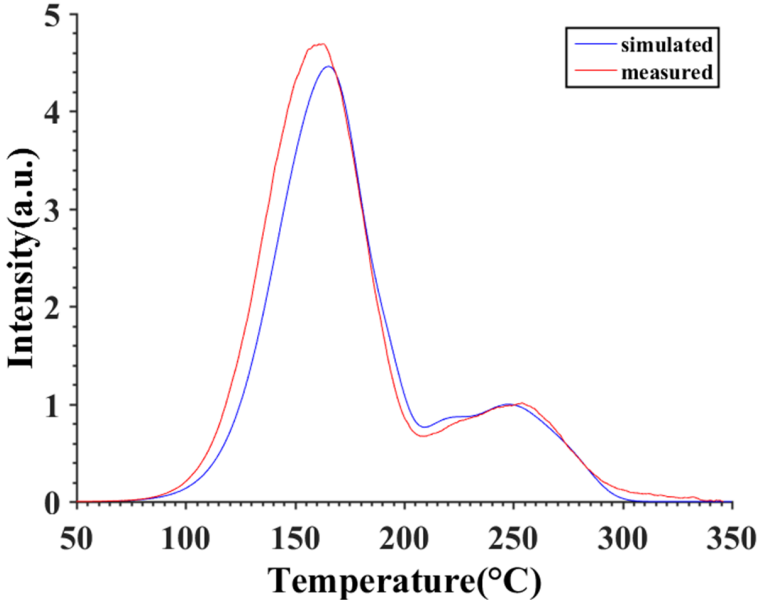


Figure 5.5: Simulated fit to the measured data for microparticles from an explosive test. This fit corresponds to a grid location where $\tau$ is 50ms and $T_{max}$ is 322°C.

smallest average difference between points. The resulting grid of best matching parameters is shown in Figure 5.4. The yellow ridge along the center of the figure represents the best matches between simulated and measured data for the different values of $T_{max}$ and $\tau$. If a time constant of 50ms is assumed for the microparticles in the explosive testing by using Figure 5.4 this corresponds to a $T_{max}$ of 322°C in equation (5.5). The simulated fit to the measured data at the grid point for a $\tau$ of 50ms and $T_{max}$ of 322°C is shown in Figure 5.5.

## 5.4 Measurement using Individual Microparticles

The TL material chosen for the thermal measurements was magnesium borate($MgB_4O_7$:Dy,Li) which will be referred to as MBO for the sake of brevity. The concentrations of dysprosium and lithium were both 0.1%. Impurities of dysprosium and lithium listed in the chemical formula act as traps and/or recombination centers in the host material of magnesium borate to give the material additional spectral and TL peak features. This material was synthesized by solution combustion synthesis and supplied by the

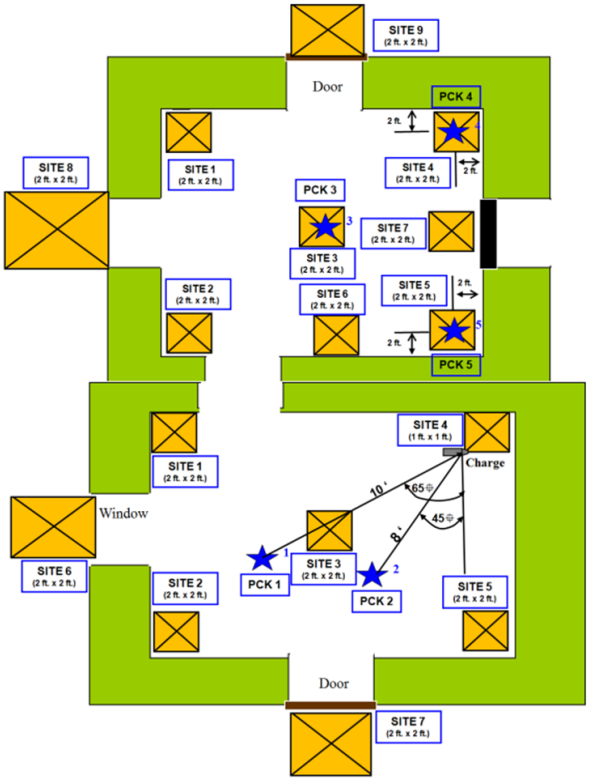


Figure 5.6: Explosive test chamber consisting of two rooms. A source with the explosive charge and an adjacent room. There are 5 MBO samples spread throughout the two chambers. The yellow boxes indicate sample collection sites while the blue stars indicate where the MBO samples were placed.

group from Oklahoma State University as mentioned in [7]. The maximum size of the particles were 180µm with a nominal size of 35-120µm. They were irradiated with 200Gy of gamma radiation to fill the traps in the band gap in preparation for measuring temperature. Explosive testing was done at a test chamber at the Kirtland Air Force Base in Albuquerque New Mexico. The test chamber consisted of two rooms, a source room in which the explosive charge was placed and an adjacent room. These two rooms are connected by a door way. The basic layout of the test chamber is shown in Figure 5.6. MBO is placed at five different locations throughout the test chamber, two of the locations were in the source room and three locations were in the adjacent room. Each location utilized 3 grams of MBO. A 5lb pentolite bare charge was used for

the explosive detonation. The debris from the explosion which contained the MBO for testing was collected from 15 different locations throughout the chamber. Depending on the location, the amount of debris collected ranged from a few grams up to about 100 grams. The example analysis presented here was done on the microparticles from site 3 in the source room. These were chosen because the temperature reversal of the milligram sized samples in this area showed that it was a moderate temperature area when compared to the coolest areas farthest from the explosion charge and hottest areas near the explosive charge. It was the location most likely to have reasonable amounts of trap depopulation. Because if there was not enough or too much trap depopulation a large range of temperatures in the microparticles probably wouldnt be observed.

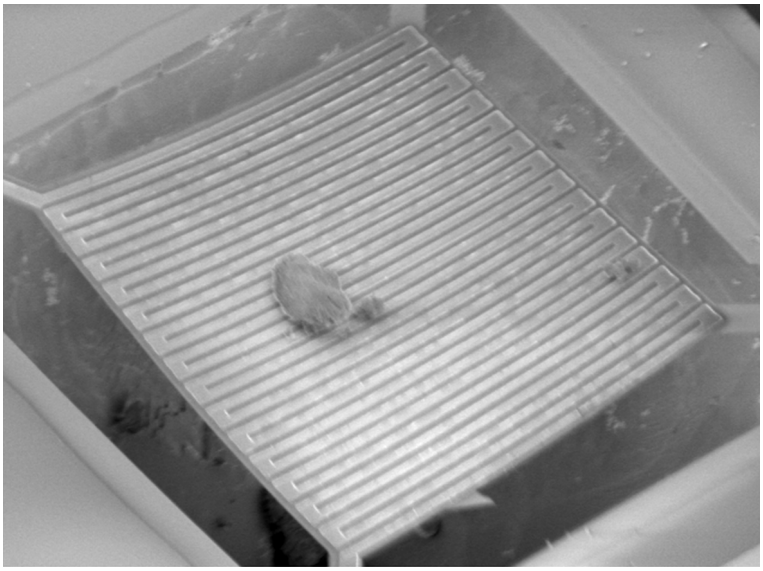

Figure 5.7: Microheater with MBO microparticle.

Microheaters were used to measure the thermoluminescence of the individual microparticles. The microheaters were constructed of a square 300 x 300µm platform which were the structural layer and were made of silicon nitride. The platform is suspended in air by four legs that allow for good thermal isolation from the substrate. There is a platinum heating element in a serpentine pattern across the microheater to evenly heat it the entire structure. There is also a thin layer of silicon nitride deposited across the surface of the microheater to protect the platinum heating element

from reacting with the atmosphere or any samples placed on it. Acquiring individual microparticles from the debris is a tedious process. There is no obvious or simple way to identify microparticles of MBO from the debris. But since the MBO appears white under a microscope it gave a starting point for selecting particles for testing. After several particles were selected for testing they were picked up and moved out of the debris one at time and placed on the microheaters as seen in Figure 5.7. The particles chosen for testing were 25-75µm in diameter for more consistent heating. Due to the time consuming nature of finding enough viable particles only 90 microparticles were tested for a TL signal. The MBO was then heated at a linear rate of 2°C/s from room temperature up to 400°C. During the heating process the thermoluminescence was measured using a photomultiplier tube due to the extremely weak signal from the small mass of MBO.

## 5.5 Analysis of Individual Microparticle Measurements

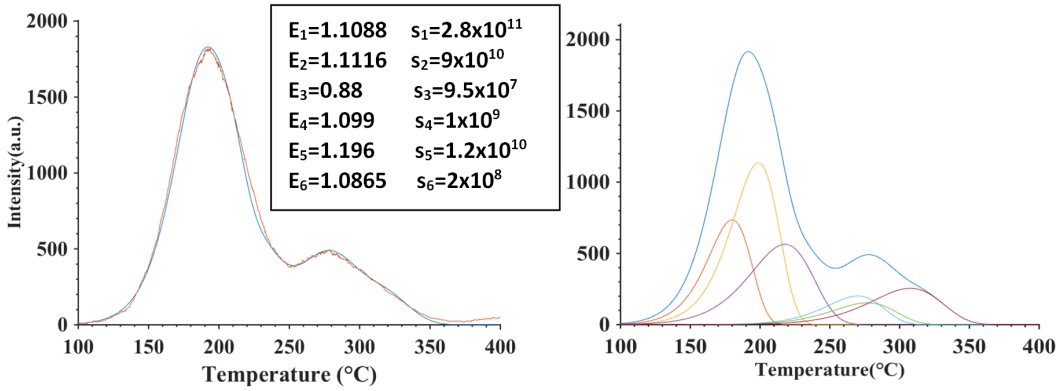


Figure 5.8: (left) The curve fit compared to measured MBO control sample using the linear superposition of 6 first-order curves. (Right) Graph showing the individual first-order curves used to do the fit. The legend shows the values for $E$ in eV and $s$ in inverse seconds.

The first step in reversing the temperature from the MBO microparticles is to find the values for $n$, $E$, and $s$ to get a proper fit to the control sample of MBO. The fit to the MBO control curve in previous work [7] consisted of 28 single order curves. In this work it was decided to use fewer curves for the sake of computational simplicity. A total of 6 curves was found to make a good fit to the control and the results are shown in

Figure 5.8. The final curve fit to the control is a linear superposition of the first-order kinetics equations. The trap depth $E$ determines the peak position and the frequency factor $s$ affects the peak width, position, and amplitude. The initial filled trap density

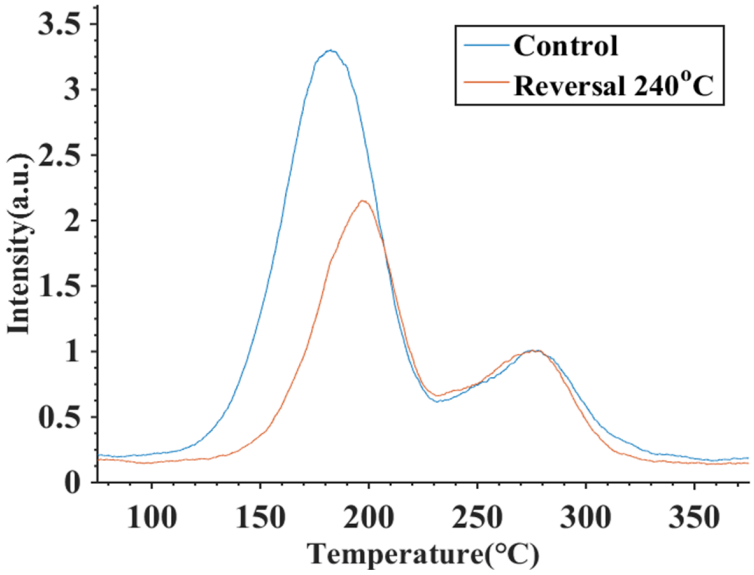


Figure 5.9: An example of an MBO microparticle which experienced a temperature of 240°C compared to a control sample. The lower temperature first-order peaks decreased in intensity indicating that those traps at least partially emptied.

$n_0$ is basically a scaling factor, so it is not as important as the other parameters $E$ and $s$. Figure 5.9 is a comparison between the measured thermoluminescence of the MBO control and a MBO microparticle that was in the explosive testing. The TL curves with peaks at lower temperatures tend to be shallower traps so they require less thermal energy in order to start emptying. The maximum temperature calculated for this example was 240°C.

As mentioned before, selecting MBO microparticles from the debris is a tedious and difficult process. The microscope was not the only method used to identify microparticles in the debris; energy dispersive spectroscopy(EDS) was also used. In this sampling of microparticles 15 potential MBO particles were selected from the debris. The initial selection was done by looking for microparticles that appeared white under a microscope. All the particles had diameters of 25-75µm. The EDS peaks of greatest interest used to identify the MBO were the magnesium and oxygen peaks. These peaks did not

appear as strongly in samples that had more of an atomic soup as seen in the EDS measurement shown in Figure 5.10.

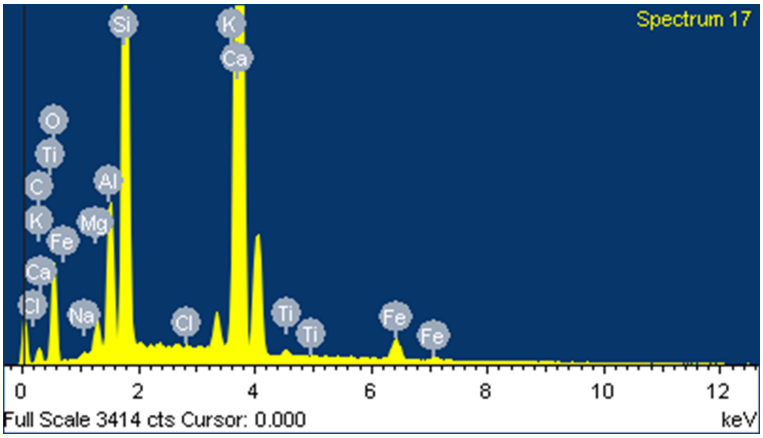


Figure 5.10: Energy dispersive spectroscopy measurement of debris which resembled MBO microparticles. The atomic soup had very weak signals for magnesium and consisted of titanium, calcium, potassium, iron, and aluminum.

Many different peaks indicating atoms not in the MBO indicated they were most likely debris. The EDS measurements of microparticles thought to be debris had peaks indicating titanium, calcium, potassium, iron, and aluminum. Although some of the samples had strong peaks for the magnesium and oxygen but also contained less intense peaks similar to that seen in the debris. This may be due to residue on the surface of MBO samples from the explosive event or from the environment.

A total of 90 microparticles were tested for thermoluminescence using the microheaters. Of these only 42 showed any measureable thermoluminescence. This means that the remaining 48 particles were either debris or completely depopulated MBO. Due to difficulty in handling of the microparticles EDS measurements could not be done to confirm their atomic composition. But temperature reversals were possible on the remaining 42 particles and the results are listed in Figure 9. There is a wide range of measured temperatures. Ranging from room temperature to 510°C with a clustering of microparticles around 290°C. Milligram size measurements made up of hundreds of microparticles at the same site 3 collection location show a temperatures of 331°C. This temperature is inside the clustering of temperatures measured for the microparticles. But when individual particles are measured a range of temperatures experienced by the

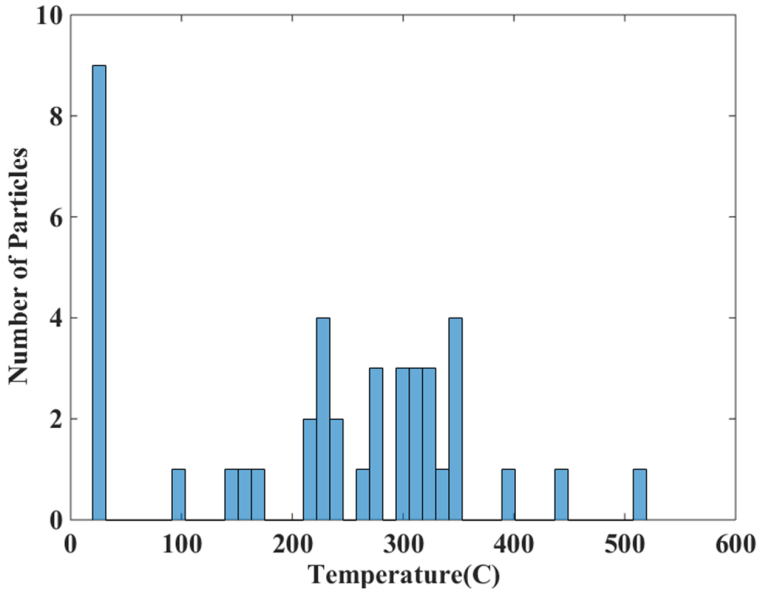


Figure 5.11: Histogram of the number of particles vs temperature measured. There is a wide range of measurements from room temperature up to 510°C. A measurement of MBO in milligrams from the same site 3 indicated a temperature of 331°C. But by looking at individual particles the temperature each particle experiences is not a single temperature but is over a range of temperatures.

microparticles because apparent. This means that some microparticles may have been shielded from the heat by microparticles closer to the explosion or it could be possible due to mixing from samples that were placed closer to or farther away from the explosive charge. Because there are also samples placed in the adjacent room that would not have experienced as much heat but could have been blown into the source room due to air flow around the two rooms from the shock wave. What can be observed from this is that if there is a minimum temperature that needs to be reached in entire test chamber a hotter explosive charge will be required in order to reach it. The maximum temperature experienced by the microparticles is in excess of 510°C. When milligram size samples are measured these finer points on the minimum and maximum bounds on temperatures in the chamber would be missed.

# Chapter 6

# Conclusion and Discussion

## 6.1 Importance of Thermoluminescent Trap Parameters

Possibly the most important information to have about a thermoluminescent material for any application are knowing with some amount of certainty the trap parameters $n$, $s$, end $E_t$. For applications in geological/archaeological dating or radiation dosimetry the trap parameters will not be as important because the correlation between radiation dosage and intensity of thermoluminescence can be empirically determined with sufficient accuracy. Mainly due to the fact they are only looking at one feature of the thermoluminescence the absolute intensity. But for the application of temperature sensing knowing the trap parameters is of paramount importance. It is very useful to have as much knowledge of the trap parameters as possible will because it will lead to more accurate measurements of the temperature profile due to the complexity that goes into comparing the shape of the glow curves between the control and temperature profile samples.

Thermoluminescence is highly dependent on the defects and impurities present in the material, so variations in the kinds of defects or impurities can significantly alter the glow curve. In the case of the $Y_2O_3$:Tb thin film of chapter 3 the thermoluminescent response would change a little bit from batch to batch. The temperature at which the glow curve peaks occur could shift as much as about $10^o$ Celsius along with the widths of the curves. This is due to the difficulty in controlling every parameter in the deposition process such as deposition rate and impurity concentrations. Given more time and examination on

how various steps in the process effect the outcome of the thermoluminescence these variations from batch to batch can most likely be significantly reduced. Even for the most widely used TLD material TLD-100 the amount of traps, trap parameters and first or higher order modeling has been debated for the last 40 years [85–91]. To the date of this thesis being published there is still debates going on about the trap nature of TLD-100. The lack of consensus on the trap parameters of TLD-100 do not hold it back from being a accurate method for measuring radiation dosage. For the application of temperature sensing the trap parameters are more important but a complete knowledge of them is not necessary to have a accurate measurement of temperature. But the more is known about the trap parameters the more accurate the measurement could be.

## 6.2 Possible Future Application of Thermoluminescence

Inspired by an idea of Manfred the author of [63] who suggested an integrated thermoluminescent device for measuring radiation dosage, is to combine a thermoluminescent thin film like the $Y_2O_3$:Tb described in chapter 3 with microheaters like those described in chapters 4 or 5. The thermoluminescent thin film would act as a TLD material and the microheater will allow for the heating which can be combined with a light sensor to make a complete measurement of a glow curve. This combination of thin film and microheater with light sensor fabricated into a integrated package would have dosimetric applications. The rings and badges used in the current TLD industry need to be measured using specialized equipment. The integrated package in the microheater is compatible with standard VLSI fabrications techniques so it could be made for cheap and requires no special equipment to measure the amount of dosage.

The primary drawback to this application is the need for finding a way to grow a thin film on the microheater that consistently has similar trap parameters from batch to batch. This is merely a processing concern that could eventually be ironed out.

# References


[1] Martin Jim Aitken. *Thermoluminescence dating.* Academic press, 1985.

[2] Richard G Roberts, Rhys Jones, and Michael A Smith. Thermoluminescence dating of a 50,000-year-old human occupation site in northern australia. 1990.

[3] AG Wintle and DJ Huntley. Thermoluminescence dating of sediments. *Quaternary Science Reviews*, 1(1):31–53, 1982.

[4] G Guerin and G Valladas. Thermoluminescence dating of volcanic plagioclases. *Nature*, 286(5774):697–699, 1980.

[5] Martin J Aitken. Thermoluminescence dating of ancient pottery. *Scientific methods in medieval archaeology*, pages 271–279, 1970.

[6] Stephen WS McKeever, Marko Moscovitch, and Peter David Townsend. Thermoluminescence dosimetry materials: properties and uses. 1995.

[7] Alastair F McKinlay. Thermoluminescence dosimetry. 1981.

[8] AJJ Bos. High sensitivity thermoluminescence dosimetry. *Nuclear Instruments and Methods in Physics Research Section B: Beam Interactions with Materials and Atoms*, 184(1):3–28, 2001.

[9] T Kron. Applications of thermoluminescence dosimetry in medicine. *Radiation protection dosimetry*, 85(1-4):333–340, 1999.

[10] Philip R Armstrong, Merlin L Mah, Sangho S Kim, and Joseph J Talghader. Thermoluminescence of y 2 o 3: Tb 3+ thin films deposited by electron beam evaporation. *Journal of Luminescence*, 148:225–229, 2014.

[11] CS Alexander, MF Morris, and SWS McKeever. The time and wavelength response of phototransferred thermoluminescence in natural and synthetic quartz. *Radiation measurements*, 27(2):153–159, 1997.

[12] JY Chang. Correlation study of energetic ion induced optical absorption and thermoluminescence in crystalline lif and caf2. *IEEE Transactions on Nuclear Science*, 30(6):4081–4086, 1983.

[13] Shang-Chou Chang and Ching-Shen Su. Relationship between ultraviolet radiation induced thermoluminescence and crystalline structure of zro2. *Radiation effects and defects in solids*, 127(2):207–213, 1993.

[14] SA Durrani, KAR Khazal, SWS McKeever, and RJ Riley. Studies of changes in the thermoluminescence sensitivity in quartz induced by proton and gamma irradiations. *Radiation Effects*, 33(4):237–244, 1977.

[15] Yasuo Suzuoki, Kazumitsu Yasuda, Teruyoshi Mizutani, and Masayuki Ieda. Thermoluminescence in high density polyethylene and its oxidation effects. *Japanese Journal of Applied Physics*, 16(8):1339, 1977.

[16] SC Sabharwal et al. Study of growth imperfections, optical absorption, thermoluminescence and radiation hardness of cdwo 4 crystals. *Journal of crystal growth*, 200(1):191–198, 1999.

[17] M Ohta and M Takami. Thermoluminescent properties of tridymite sio2: Al3+, eu3+. *Journal of Sol-Gel Science and Technology*, 19(1-3):737–740, 2000.

[18] N Kristianpoller, A Rehavi, A Shmilevich, D Weiss, and R Chen. Radiation effects in pure and doped al 2 o 3 crystals. *Nuclear Instruments and Methods in Physics Research Section B: Beam Interactions with Materials and Atoms*, 141(1):343–346, 1998.

[19] M Martini, G Spinolo, A Vedda, and C Arena. Phosphorescence and thermally stimulated luminescence of amorphous sio2. *Solid state communications*, 91(9):751–756, 1994.

[20] VI Arkhipov, EV Emelianova, R Schmechel, and H von Seggern. Thermally stimulated luminescence versus thermally stimulated current in organic semiconductors. *Journal of non-crystalline solids*, 338:626–629, 2004.

[21] Harry G Hecht and E Donald Taylor. Thermoluminescent study of the color centers in irradiated polycrystalline mgo. *Journal of Physics and Chemistry of Solids*, 28(8):1599–1605, 1967.

[22] ED Taylor and HG Hecht. Thermoluminescent study of x-irradiated polycrystalline cao, sro and bao. *Journal of Physics and Chemistry of Solids*, 29(5):865–868, 1968.

[23] GFJ Garlick, M Springford, and H Checinska. The infra-red emission of indium sesquisulphide. *Proceedings of the Physical Society*, 82(1):16, 1963.

[24] RK Choudhary, A Soni, P Mishra, DR Mishra, and MS Kulkarni. Synthesis of aluminum nitride thin films and their potential applications in solid state thermoluminescence dosimeters. *Journal of Luminescence*, 155:32–38, 2014.

[25] A Sathyamoorthy and JM Luthra. Mechanism of thermoluminescence in magnesium oxide. *Journal of Materials Science*, 13(12):2637–2644, 1978.

[26] Dušan A Pejaković. Studies of the phosphorescence of polycrystalline hafnia. *Journal of Luminescence*, 130(6):1048–1054, 2010.

[27] Yan Yang, Hua Wei, Lihua Zhang, Kim Kisslinger, Charles L. Melcher, and Yiquan Wu. Blue emission of eusup2+/sup-doped translucent alumina. *Journal of Luminescence*, 168(1):297 – 303, 2015.

[28] NNH Ramli, H Salleh, GA Mahdiraji, MI Zulkifli, S Hashim, DA Bradley, and NM Noor. Characterization of amorphous thermoluminescence dosimeters for patient dose measurement in x-ray diagnostic procedures. *Radiation Physics and Chemistry*, 116:130–134, 2015.

[29] JM Oduko and NM Spyrou. Thermoluminescence of irradiated foodstuffs. *International Journal of Radiation Applications and Instrumentation. Part C. Radiation Physics and Chemistry*, 36(5):603–607, 1990.

[30] C Christodoulides and JH Fremlin. Thermoluminescence of biological materials. *Nature*, 232:257–258, 1971.

[31] Patrick T McCutcheon. Thermoluminescent analysis of burned bone: Assessing the problems. ACS Publications, 1996.

[32] Jyoti Gaikwad, S Thomas, S Kamble, PB Vidyasagar, and A Sarma. Effect of 7 li (45 mev) ions on spinach leaves studied by thermoluminescence technique. *Nuclear Instruments and Methods in Physics Research Section B: Beam Interactions with Materials and Atoms*, 156(1):231–235, 1999.

[33] CM Sunta, WEF Ayta, JFD Chubaci, and S Watanabe. A critical look at the kinetic models of thermoluminescence: I. first-order kinetics. *Journal of Physics D: Applied Physics*, 34(17):2690, 2001.

[34] CM Sunta, WEF Ayta, JFD Chubaci, and S Watanabe. A critical look at the kinetic models of thermoluminescenceii. non-first order kinetics. *Journal of Physics D: Applied Physics*, 38(1):95, 2004.

[35] Stephen WS McKeever. *Thermoluminescence of solids*, volume 3. Cambridge University Press, 1988.

[36] Reuven Chen and Stephen WS McKeever. *Theory of thermoluminescence and related phenomena*. World Scientific, 1997.

[37] Reuven Chen. On the calculation of activation energies and frequency factors from glow curves. *Journal of Applied Physics*, 40(2):570–585, 1969.

[38] David J Huntley and Michel Lamothe. Ubiquity of anomalous fading in k-feldspars and the measurement and correction for it in optical dating. *Canadian Journal of Earth Sciences*, 38(7):1093–1106, 2001.

[39] Fouad A Hasan, Bradly D Keck, Christopher Hartmetz, and Derek WG Sears. Anomalous fading of thermoluminescence in meteorites. *Journal of luminescence*, 34(6):327–335, 1986.

[40] KL Choy, JP Feist, AL Heyes, and B Su. Eu-doped y 2 o 3 phosphor films produced by electrostatic-assisted chemical vapor deposition. *Journal of materials research*, 14(07):3111–3114, 1999.

[41] Vijay Singh, Vineet Kumar Rai, Isabelle Ledoux-Rak, Shigueo Watanabe, TK Gundu Rao, Jose Fernando Diniz Chubaci, Laurent Badie, Fabienne Pelle, and Svetlana Ivanova. Nir to visible up-conversion, infrared luminescence, thermoluminescence and defect centres in y2o3: Er phosphor. *Journal of Physics D: Applied Physics*, 42(6):065104, 2009.

[42] MA Flores-Gonzalez, G Ledoux, Stéphane Roux, K Lebbou, Pascal Perriat, and O Tillement. Preparing nanometer scaled tb-doped y 2 o 3 luminescent powders by the polyol method. *Journal of Solid State Chemistry*, 178(4):989–997, 2005.

[43] Peter A Tanner and Ka Leung Wong. Synthesis and spectroscopy of lanthanide ion-doped y2o3. *The Journal of Physical Chemistry B*, 108(1):136–142, 2004.

[44] Paulo Jorge Ribeiro Montes, Mario Ernesto Giroldo Valerio, Marcelo Andrade Macêdo, Frederico Cunha, and Jose Marcos Sasaki. Yttria thin films doped with rare earth for applications in radiation detectors and thermoluminescent dosimeters. *Microelectronics Journal*, 34(5):557–559, 2003.

[45] Daniele Gozzi, Alessandro Latini, Giancarlo Salviati, and Nicola Armani. Growth and characterization of red-green-blue cathodoluminescent ceramic films. *Journal of applied physics*, 99(12):123524, 2006.

[46] JC Alonso, E Haro-Poniatowski, R Diamant, M Fernández-Guasti, and M Garcia. Photoluminescent thin films of terbium chloride-doped yttrium oxide deposited by the pulsed laser ablation technique. *Thin Solid Films*, 303(1-2):76–83, 1997.

[47] Nameeta Brahme, Anuradha Gupta, DP Bisen, and U Kurrey. Thermoluminescence study of y2o3: Tb. *Recent Research in Science and Technology*, 4(8), 2012.

[48] Adrie JJ Bos, Pieter Dorenbos, Aurélie Bessière, and Bruno Viana. Lanthanide energy levels in ypo 4. *Radiation Measurements*, 43(2):222–226, 2008.

[49] AH Krumpel, E Van Der Kolk, D Zeelenberg, AJJ Bos, KW Krämer, and P Dorenbos. Lanthanide 4 f-level location in lanthanide doped and cerium-lanthanide codoped nalaf 4 by photo-and thermoluminescence. *Journal of applied physics*, 104(7):073505, 2008.

[50] Jumpei Ueda, Pieter Dorenbos, Adrie JJ Bos, Andries Meijerink, and Setsuhisa Tanabe. Insight into the thermal quenching mechanism for y3al5o12: Ce3+ through thermoluminescence excitation spectroscopy. *The Journal of Physical Chemistry C*, 119(44):25003–25008, 2015.

[51] Adrie JJ Bos, Ronald M Van Duijvenvoorde, Erik Van der Kolk, Winicjusz Drozdowski, and Pieter Dorenbos. Thermoluminescence excitation spectroscopy: A versatile technique to study persistent luminescence phosphors. *Journal of Luminescence*, 131(7):1465–1471, 2011.

[52] AV Sidorenko, P Dorenbos, AJJ Bos, CWE Van Eijk, and PA Rodnyi. Lanthanide level location and charge carrier trapping in lilnsio4: Ce3+, sm3+, ln= y or lu. *Journal of Physics: Condensed Matter*, 18(19):4503, 2006.

[53] Jianhua Hao, SA Studenikin, and Michael Cocivera. Blue, green and red cathodoluminescence of y 2 o 3 phosphor films prepared by spray pyrolysis. *Journal of Luminescence*, 93(4):313–319, 2001.

[54] A de J Morales Ramírez, A García Murillo, F de J Carrillo Romo, J Ramírez Salgado, C Le Luyer, G Chadeyron, D Boyer, and J Moreno Palmerin. Preparation and studies of eu 3+ and tb 3+ co-doped gd 2 o 3 and y 2 o 3 sol–gel scintillating films. *Thin Solid Films*, 517(24):6753–6758, 2009.

[55] Gabrielle G Long, DR Black, A Feldman, EN Farabaugh, RD Spal, DK Tanaka, and Z Zhang. Structure of vapor-deposited yttria and zirconia thin films. *Thin Solid Films*, 217(1-2):113–119, 1992.

[56] ED Wachsman, N Jiang, CW Frank, DM Mason, and DA Stevenson. Spectroscopic investigation of oxygen vacancies in solid oxide electrolytes. *Applied Physics A*, 50(6):545–549, 1990.

[57] Jingyu Lu, Ting Xu, and Jianmin Miao. Temperature control of microheaters for localized carbon nanotube synthesis. *Journal of nanoscience and nanotechnology*, 11(12):10498–10502, 2011.

[58] O Grudin, R Marinescu, LM Landsberger, M Kahrizi, G Frolov, JDN Cheeke, S Chehab, Michael Post, Jim Tunney, Xiaomei Du, et al. High-temperature gas sensor using perovskite thin films on a suspended microheater. *Journal of Vacuum Science & Technology A: Vacuum, Surfaces, and Films*, 20(3):1100–1104, 2002.

[59] Gwiy-Sang Chung and Jae-Min Jeong. Fabrication of micro heaters on polycrystalline 3c-sic suspended membranes for gas sensors and their characteristics. *Microelectronic Engineering*, 87(11):2348–2352, 2010.

[60] H-Y Lee, S Moon, SJ Park, J Lee, K-H Park, and J Kim. Micro-machined resistive micro-heaters for high temperature gas sensing applications. *Electronics Letters*, 44(25):1460–1461, 2008.

[61] Minhee Kim, Roman Brukh, Sumit Kishore, Somenath Mitra, and Durgamadhab Misra. Design and fabrication of heated microchannels. *Sensors and Materials*, 18(1):35–48, 2006.

[62] Merlin L Mah, Michael E Manfred, Sangho S Kim, Mirjana Prokic, Eduardo G Yukihara, and Joseph J Talghader. Measurement of rapid temperature profiles using thermoluminescent microparticles. *IEEE Sensors Journal*, 10(2):311–315, 2010.

[63] Michael E Manfred, Nicholas T Gabriel, Eduardo G Yukihara, and Joseph J Talghader. Thermoluminescence measurement technique using millisecond temperature pulses. *Radiation protection dosimetry*, 139(4):560–564, 2010.

[64] Philip R Armstrong, Merlin L Mah, Lucas Taylor, and Joseph J Talghader. Reduced blackbody microheaters for measuring high temperature thermoluminescent glow curve peaks. In *Optical MEMS and Nanophotonics (OMN), 2014 International Conference on*, pages 7–8. IEEE, 2014.

[65] PR Armstrong, ML Mah, KD Olson, and JJ Talghader. Microheater multilayer interference to reduce thermal emission for low photon number luminescence measurement. In *Solid-State Sensors, Actuators and Microsystems (TRANSDUCERS), 2015 Transducers-2015 18th International Conference on*, pages 924–927. IEEE, 2015.

[66] Merlin L Mah, Philip R Armstrong, Sangho S Kim, Joel R Carney, James M Lightstone, and Joseph J Talghader. Thermal history sensing inside high-explosive environments using thermoluminescent microparticles. In *Sensors, 2011 IEEE*, pages 1269–1272. IEEE, 2011.

[67] Xiaodong He, Yibin Li, Lidong Wang, Yue Sun, and Sam Zhang. High emissivity coatings for high temperature application: progress and prospect. *Thin Solid Films*, 517(17):5120–5129, 2009.

[68] ZX Cai, XY Zeng, and J Duan. Fabrication of platinum microheater on alumina substrate by micro-pen and laser sintering. *Thin Solid Films*, 519(11):3893–3896, 2011.

[69] G-S Chung and S-S Noh. Fabrication of the pt microheater using aluminum oxide as a medium layer and its characteristics. *Sensors and materials*, 10(5):251–261, 1998.

[70] X Zhang, HQ Xie, M Fujii, H Ago, K Takahashi, T Ikuta, H Abe, and T Shimizu. Thermal and electrical properties of a suspended nanoscale thin film. *International journal of thermophysics*, 28(1):33–43, 2007.

[71] Nicholas T Gabriel and Joseph J Talghader. Thermal conductivity and refractive index of hafnia-alumina nanolaminates. *Journal of Applied Physics*, 110(4):043526, 2011.

[72] AI Abdulagatov, Y Yan, JR Cooper, Y Zhang, ZM Gibbs, AS Cavanagh, RG Yang, YC Lee, and SM George. Al2o3 and tio2 atomic layer deposition on copper for water corrosion resistance. *ACS applied materials & interfaces*, 3(12):4593–4601, 2011.

[73] Yeh Pochi. Optical waves in layered media. *J. Wiley & Sons*, 1988.

[74] RG Fairchild, PL Mattern, K Lengweiler, and PW Levy. Thermoluminescence of lif tld-100: Emission-spectra measurements. *Journal of Applied Physics*, 49(8):4512–4522, 1978.

[75] DB Rickman. Improved thermocouple armoring technique for blast/shock environments. In *PROCEEDINGS OF THE INTERNATIONAL INSTRUMENTATION SYMPOSIUM*, volume 44, pages 695–702. AMERICAN TECHNICAL PUBLISHERS LTD, 1998.

[76] Eric Udd. A personal review of 25 years of fiber grating sensor development. In *Proc. of SPIE Vol*, volume 8722, pages 872202–1, 2013.

[77] WK Lewis and CG Rumchik. Measurement of apparent temperature in post-detonation fireballs using atomic emission spectroscopy, 2009.

[78] Nick Glumac. Absorption spectroscopy measurements in optically dense explosive fireballs using a modeless broadband dye laser. *Applied spectroscopy*, 63(9):1075–1080, 2009.

[79] John M Densmore, Matthew M Biss, Kevin L McNesby, and Barrie E Homan. High-speed digital color imaging pyrometry. *Applied Optics*, 50(17):2659–2665, 2011.

[80] BA Doull, LC Oliveira, DY Wang, ED Milliken, and EG Yukihara. Thermoluminescent properties of lithium borate, magnesium borate and calcium sulfate developed for temperature sensing. *Journal of Luminescence*, 146:408–417, 2014.

[81] EG Yukihara, AC Coleman, and BA Doull. Passive temperature sensing using thermoluminescence: laboratory tests using li 2 b 4 o 7: Cu, ag, mgb 4 o 7: Dy, li and caso 4: Ce, tb. *Journal of Luminescence*, 146:515–526, 2014.

[82] EG Yukihara, AC Coleman, S Bastani, T Gustafson, JJ Talghader, A Daniels, D Stamatis, JM Lightstone, C Milby, and FR Svingala. Particle temperature measurements in closed chamber detonations using thermoluminescence from li 2 b 4 o 7: Ag, cu, mgb 4 o 7: Dy, li and caso 4: Ce, tb. *Journal of Luminescence*, 165:145–152, 2015.

[83] Merlin L Mah, Philip R Armstrong, Sangho S Kim, Joel R Carney, James M Lightstone, and Joseph J Talghader. Sensing the thermal history of high-explosive detonations using thermoluminescent microparticles. *IEEE Sensors Journal*, 13(5):1742–1747, 2013.

[84] Joseph J Talghader, Merlin L Mah, Eduardo G Yukihara, and Adam C Coleman. Thermoluminescent microparticle thermal history sensors. *Microsystems & Nanoengineering*, 2, 2016.

[85] SP Kathuria and CM Sunta. Kinetics and trapping parameters of thermoluminescence in lif tld-100-dependence on dose. *Journal of Physics D: Applied Physics*, 12(9):1573, 1979.

[86] GC Taylor and E Lilley. The analysis of thermoluminescent glow peaks in lif (tld-100). *Journal of Physics D: Applied Physics*, 11(4):567, 1978.

[87] RG Fairchild, PL Mattern, K Lengweiler, and PW Levy. Thermoluminescence of lif tld-100: Glow-curve kinetics. *Journal of Applied Physics*, 49(8):4523–4533, 1978.

[88] SWS McKeever. Thermoluminescence in lif: Analysis of the glow-curves. *Nuclear Instruments and Methods*, 175(1):19–20, 1980.

[89] E Lilley and GC Taylor. Order of kinetics for thermoluminescence in lif tld-100. *Journal of Physics D: Applied Physics*, 14(2):L13, 1981.

[90] SP Kathuria and CM Sunta. Order of kinetics for thermoluminescence in lif tld-100. *Journal of Physics D: Applied Physics*, 15(3):497, 1982.

[91] E Lilley and SWS McKeever. On the order of kinetics for thermoluminescence in lif (tld-100). *Journal of Physics D: Applied Physics*, 16(2):L39, 1983.

# Appendix A

# Microheater Fabrication Process

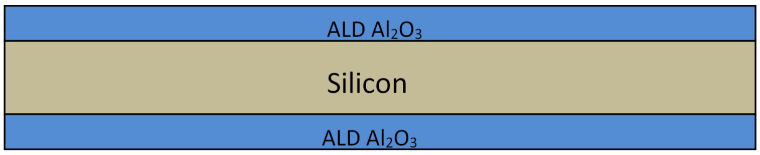


Figure A.1: Step 1: 100nm of $Al_2O_3$ is deposited onto a 4in silicon(100) wafer using atomic layer deposition(ALD). The wafer was propped up on glass slides so both sides are coated by the ALD. The top side $Al_2O_3$ will be our structural layer that the resistive heating element will be on.

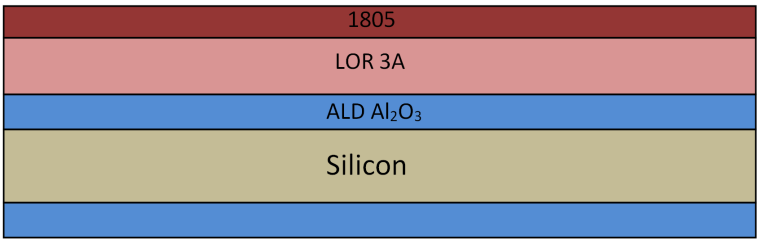


Figure A.2: Step 2: Spin on lift-of-resist (LOR 3A). And since it is not UV sensitive spin on 1805 photoresist for the UV sensitive mask. This is the first step in the lift-off process we use to deposit the platinum.

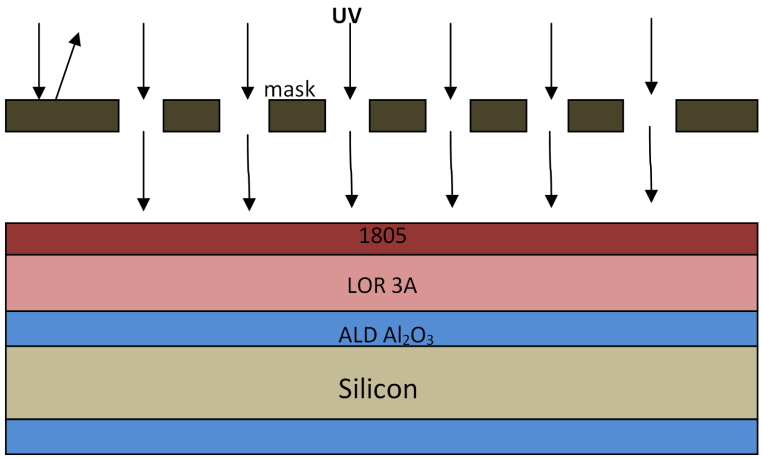


Figure A.3: Step 3a: Use the aligner and mask to expose the 1805 to UV light then develop in 351 developer to remove exposed parts of the 1805.

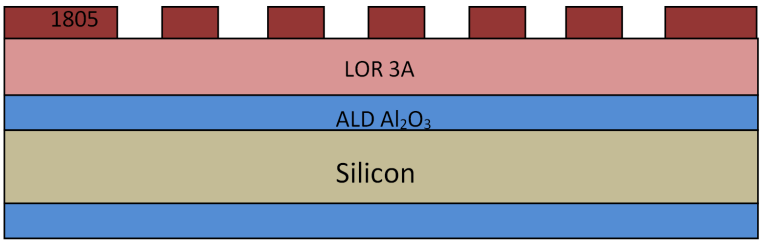


Figure A.4: Step 3b: After photoresist has been developed

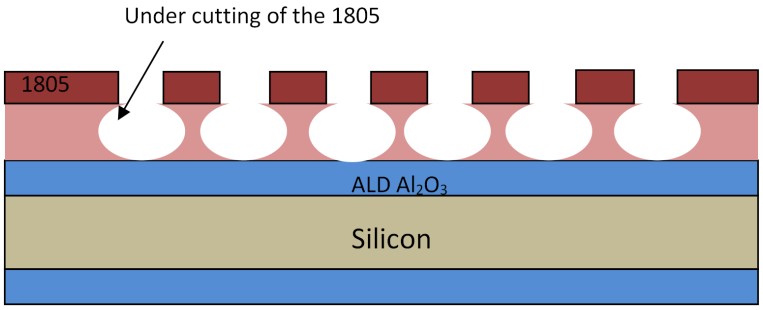


Figure A.5: Step 4: The LOR 3A is developed using CD-26 so that there is a hole through to the underlying $Al_2O_3$. This picture is not to scale but shows the under cutting of the 1805 so that there is no side wall coverage of the LOR 3A. Side wall coverage of the LOR 3A will prevent a proper lift off of the metal.

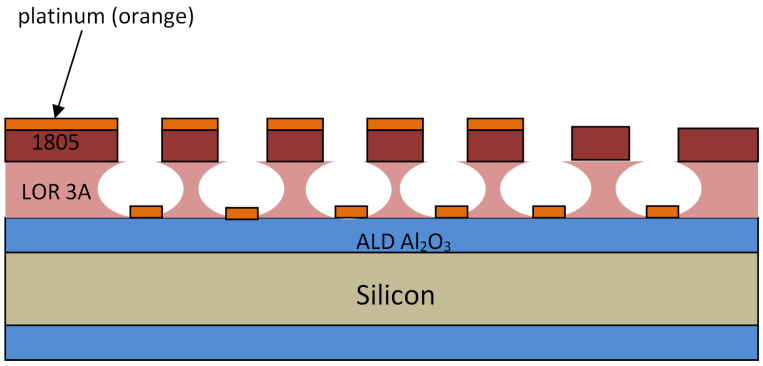


Figure A.6: Step 5: 50nm of platinum is deposited onto the surface using DC magnetron sputtering. The platinum deposited onto the $Al_2O_3$ is what we want the rest should be removed during the next step. Not shown is possible side wall coverage of the 1805 but this wont cause any problems with the lift-off.

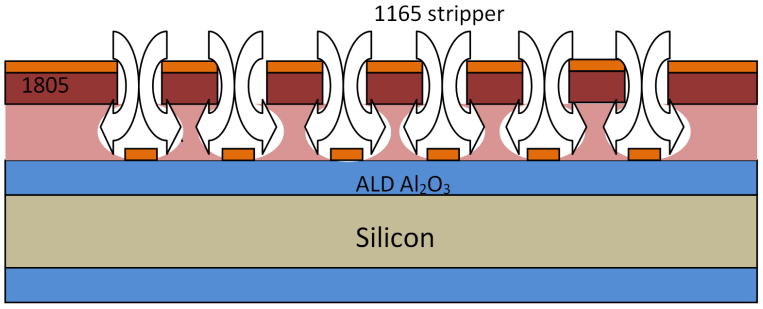


Figure A.7: Step 6a: The wafer is dunked in 1165 stripper to remove the LOR 3A. Because the platinum and 1805 are resting on top of the LOR 3A they are removed or lifted off which is why this is called a lift-off process. All that is left is the platinum that is on the $Al_2O_3$. 1165 can also attack the 1805.

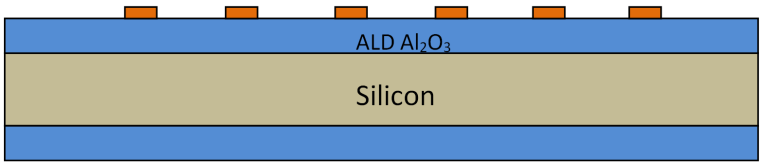


Figure A.8: Step6b: After LOR3A and photoresist was removed and only the platinum if left.

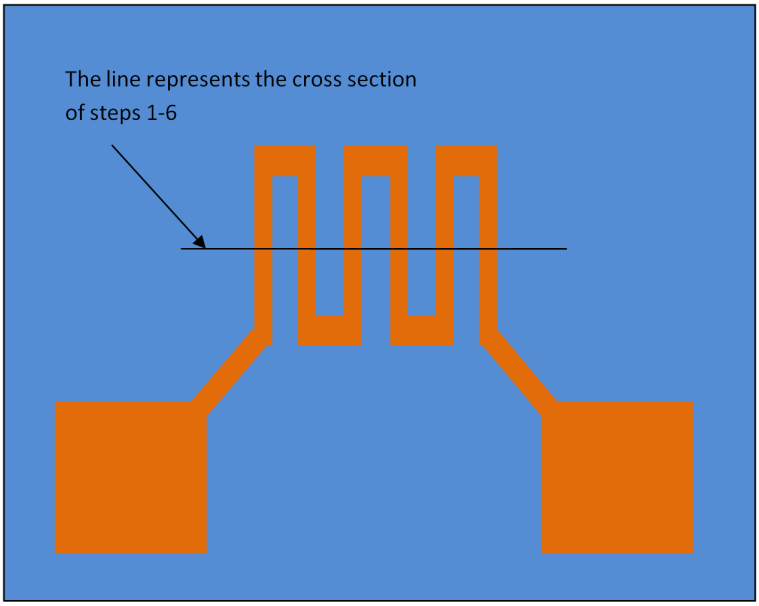


Figure A.9: This is a top view after the completion of step 6

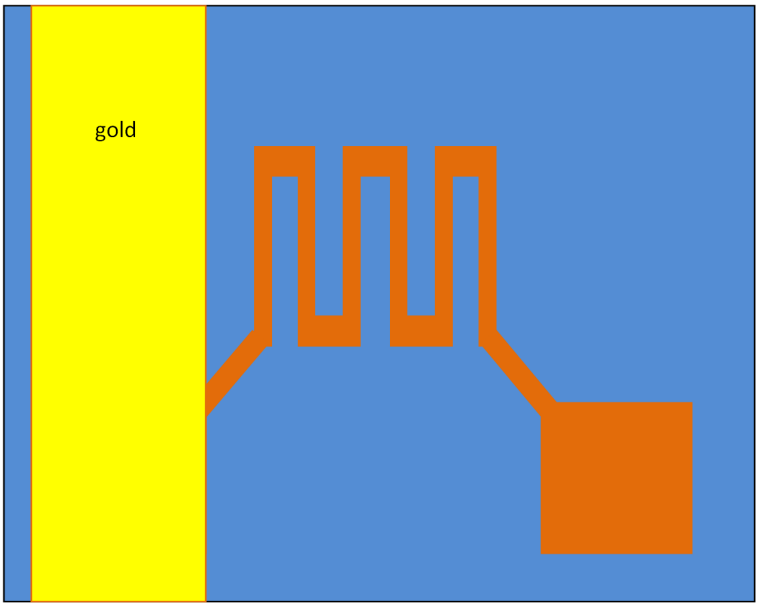


Figure A.10: Step 7: Steps 2-6 are done for the gold contact pads. The only differences are the mask and the use of gold for sputtering. The gold is 200nm thick. The gold contact pad will act like a ground for several devices. Makes characterization later on more simple.

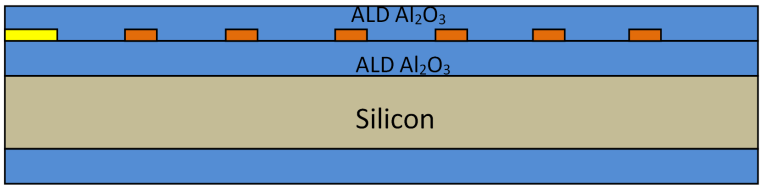


Figure A.11: Step 8: The last thin film deposition step is the encapsulation of our devices. More ALD $Al_2O_3$ (20nm) is deposited on our devices to protect from further process steps and eventual testing for characterization.

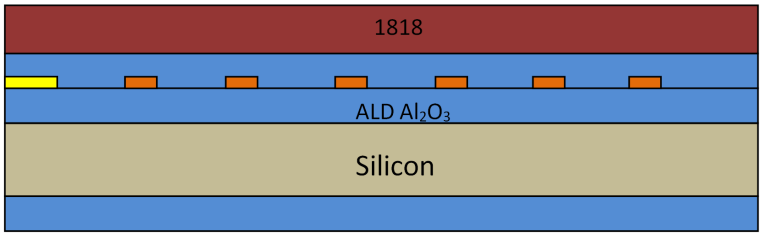


Figure A.12: Step 9: 1818 is spun on to act like a mask for the dry etch of the $Al_2O_3$. The 1818 photoresist is chosen because it is thicker than 1805.

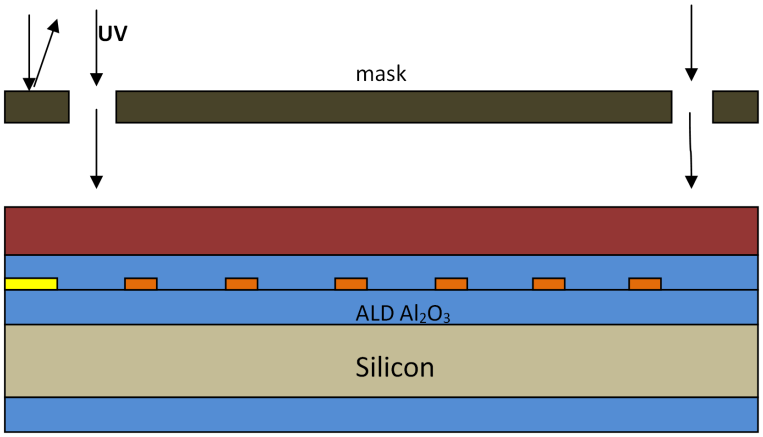


Figure A.13: Step 10a. Similar to step 3 the 1818 is exposed to UV radiation with the features for the platform defined by the mask. It is then developed in 351. The UV exposure time and 351 developer time are usually longer for 1818 because it is a thicker resist. The 1818 photoresist acts like a mask for the reactive ion etch(RIE). Ideally the $Al_2O_3$ is etched using a gas mixture of $BCl_3$ + Ar. This step may also be replaced by a BOE wet etch if desired.

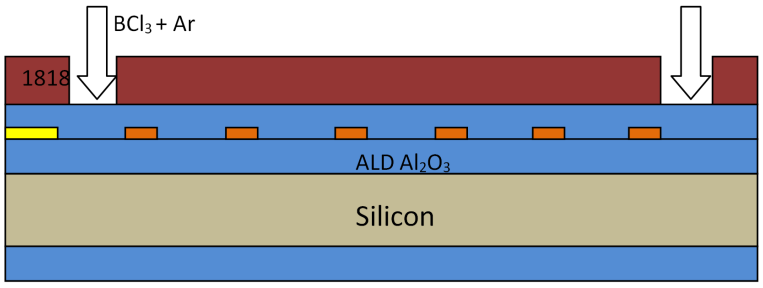


Figure A.14: Step 10b: After photoresist has been developed so the $BCl_3$ + Ar can etch the $Al_2O_3$

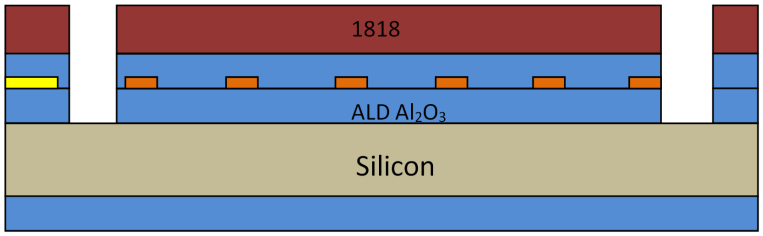


Figure A.15: Step 11a: The etch looks like an anisotropic etch in the picture but is actually an isotropic etch. The resulting etch defines the structure of the platform. It also leaves the silicon exposed making it possible to do a wet etch to remove the silicon from the bottom making it a free standing structure. This is called releasing the device. After the RIE the 1818 is removed with a solvent clean and a oxygen plasma clean if needed. The same steps to etch down to silicon were carried out to etch down to the gold so there can be an electrical contact.

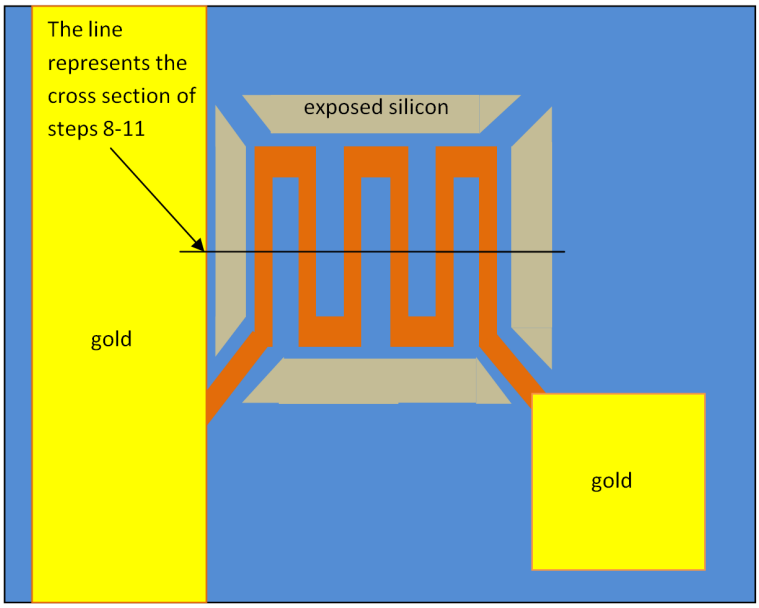


Figure A.16: Step 11b:This is a top view of the device after step 11. This is a crude drawing but gives an idea of the basic shape of our devices. The legs are actually all the same width. The encapsulating layer is clear.

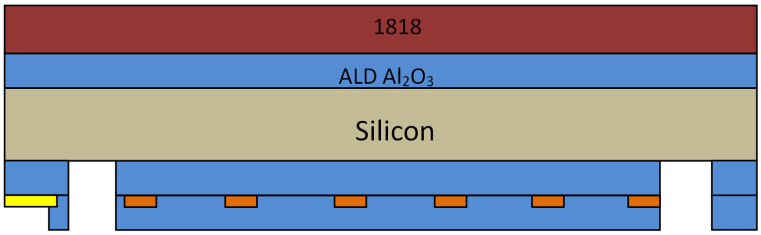


Figure A.17: Step 12: The last step is a backside etch release. A back side etch of the wafers is used to release the device. This will etch through the entire wafer from the back leaving only the $Al_2O_3$ platform and support legs. This step has several sub-steps described below. This release method has a few steps. This involves etching material out of the bottom of the wafer. So the cross section will be flipped upside down because the process only affects the bottom.

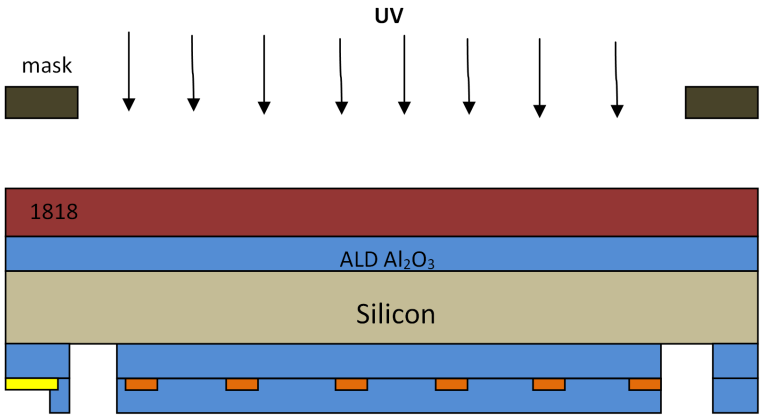


Figure A.18: Backside etch release Step 1: The RIE of the deep trench etcher using $SF_6$ will remove photoresist too quickly so a hard mask must be used. Luckily we already have a back side coating of $Al_2O_3$ to use as a backside etch mask. But the $Al_2O_3$ must be patterned using a similar method as steps 9-11. The main difference between this and the photolithography in step 10 is that there are two sets of cameras for alignment. Two on the top side of the aligner but there is also two more on the bottom side of the aligner. The backside cameras take pictures of the top of the wafer because that is where the alignment marks work. After the picture of the alignment marks is taken they are used to align to the backside of the wafer

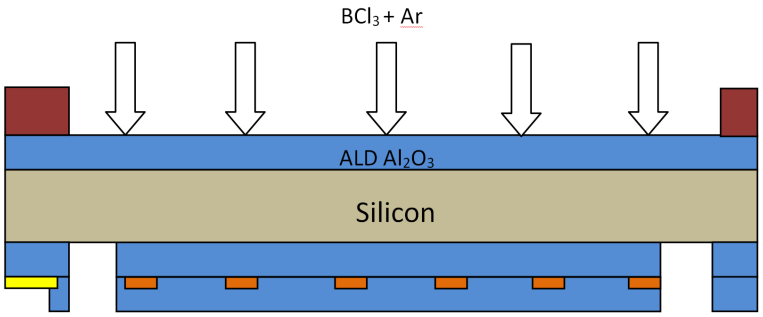


Figure A.19: Backside etch release Step 2: The hard etch mask is finally defined by using the exact same RIE gas as in step 10. The etch time would be the same because this is 120nm of $Al_2O_3$. The backside thickness is not depicted in the picture. BOE may also be a possible etch here.

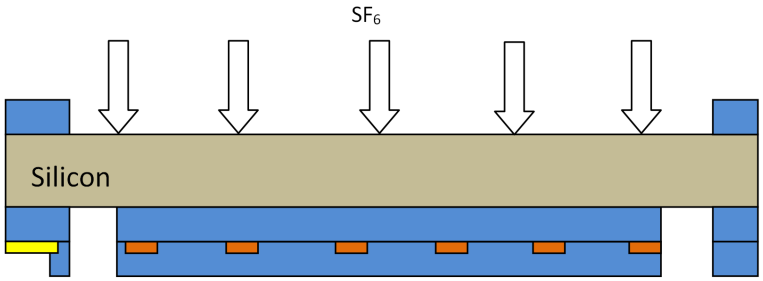


Figure A.20: Backside etch release Step 3: The deep trench etch of the backside is a anisotropic etch. It will leave vertical side walls. It does this by a series of cycles that involve coating the side walls with a polymer so they wont etch while the bottom of the etch pit is left exposed to the etch plasma.

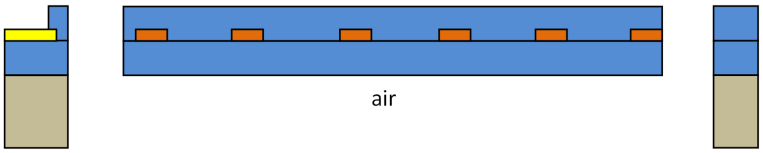


Figure A.21: This is the final result of the process with the platinum on $Al_2O_3$ micro-heater platform is freestanding.